

INFORMATION TO USERS

This manuscript has been reproduced from the microfilm master. UMI films the text directly from the original or copy submitted. Thus, some thesis and dissertation copies are in typewriter face, while others may be from any type of computer printer.

The quality of this reproduction is dependent upon the quality of the copy submitted. Broken or indistinct print, colored or poor quality illustrations and photographs, print bleedthrough, substandard margins, and improper alignment can adversely affect reproduction.

In the unlikely event that the author did not send UMI a complete manuscript and there are missing pages, these will be noted. Also, if unauthorized copyright material had to be removed, a note will indicate the deletion.

Oversize materials (e.g., maps, drawings, charts) are reproduced by sectioning the original, beginning at the upper left-hand corner and continuing from left to right in equal sections with small overlaps. Each original is also photographed in one exposure and is included in reduced form at the back of the book.

Photographs included in the original manuscript have been reproduced xerographically in this copy. Higher quality 6" x 9" black and white photographic prints are available for any photographs or illustrations appearing in this copy for an additional charge. Contact UMI directly to order.



Bell & Howell Information and Learning
300 North Zeeb Road, Ann Arbor, MI 48106-1346 USA
800-521-0600

University of Alberta

**Gas Pressure Measurements with Cantilever-in-Cantilever
Microstructures**

by

Keith Bradley Brown



A thesis submitted to the Faculty of Graduate Studies and Research in partial fulfillment
of the requirements for the degree of Master of Science

Department of Electrical and Computer Engineering

Edmonton, Alberta

Spring 1999



National Library
of Canada

Acquisitions and
Bibliographic Services

395 Wellington Street
Ottawa ON K1A 0N4
Canada

Bibliothèque nationale
du Canada

Acquisitions et
services bibliographiques

395, rue Wellington
Ottawa ON K1A 0N4
Canada

Your file Votre référence

Our file Notre référence

The author has granted a non-exclusive licence allowing the National Library of Canada to reproduce, loan, distribute or sell copies of this thesis in microform, paper or electronic formats.

The author retains ownership of the copyright in this thesis. Neither the thesis nor substantial extracts from it may be printed or otherwise reproduced without the author's permission.

L'auteur a accordé une licence non exclusive permettant à la Bibliothèque nationale du Canada de reproduire, prêter, distribuer ou vendre des copies de cette thèse sous la forme de microfiche/film, de reproduction sur papier ou sur format électronique.

L'auteur conserve la propriété du droit d'auteur qui protège cette thèse. Ni la thèse ni des extraits substantiels de celle-ci ne doivent être imprimés ou autrement reproduits sans son autorisation.

0-612-40030-1

University of Alberta

Library Release Form

Name of Author: Keith Bradley Brown


Title of Thesis: Gas Pressure Measurements with Cantilever-in-Cantilever
Microstructures

Degree: Master of Science

Year this Degree Granted: 1999

Permission is hereby granted to the University of Alberta Library to reproduce single copies of this thesis and to lend or sell such copies for private, scholarly, or scientific research purposes only.

The author reserves all other publication and other rights in association with the copyright in the thesis, and except as hereinbefore provided, neither the thesis nor any substantial portion thereof may be printed or otherwise reproduced in any material form whatever without the author's prior written permission.



(Keith B. Brown)

5 Groveland Avenue
Sherwood Park, Alberta
Canada, T8A 3G1

Date: 21 April 1999

University of Alberta

Faculty of Graduate Studies and Research

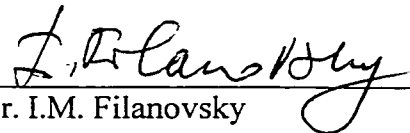
The undersigned certify that they have read, and recommend to the Faculty of Graduate Studies and Research for acceptance, a thesis entitled **Gas Pressure Measurements with Cantilever-in-Cantilever Microstructures** submitted by **Keith Bradley Brown** in partial fulfillment of the requirements for the degree of Master of Science.



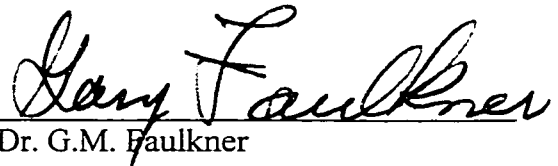
Dr. A.M. Robinson, co-supervisor



Dr. F.E. Vermeulen, co-supervisor



Dr. I.M. Filanovsky



Dr. G.M. Faulkner

Date: 20 April 1999

This thesis is dedicated to my friend,

Walter (Wally) Manchur

for always asking the right questions.

ABSTRACT

A CMOS micromachined magnetically actuated cantilever-in-cantilever (CIC) structure has been designed, constructed, and tested. The resonant behaviour of this oscillating microcantilever is modified by the changing damping effects as the ambient air pressure varies, and hence this device may be employed as a pressure sensor.

Five variations of the CIC device were constructed and tested for changes in resonant frequency, quality factor, amplitude of oscillation, and actuating current required to maintain the amplitude of oscillation constant as the ambient pressure was varied from 15 to 1450 Torr.

The results have been analyzed and a model is presented that describes the effect of gas pressure on the resonant characteristics of these devices.

ACKNOWLEDGEMENTS

I would like to express my sincere gratitude to my supervisors, Dr. A.M. Robinson and Dr. F.E. Vermeulen, for their patience, guidance, assistance, and constant support. In particular, to Dr. Robinson for providing an environment conducive to research and learning, and to Dr. Vermeulen for his ever-positive feedback. Special appreciation and thanks are extended to Dr. W. Allegretto, Dr. I. Filanovsky, and Dr. R.P.W. Lawson for their discussions, assistance, and encouraging words.

It is also my wish to acknowledge the support of the Canadian Microelectronics Corporation (CMC) without which this research could not have been accomplished. The author appreciates the support and services provided by the Alberta Microelectronic Corporation (AMC). Special thanks are due to the Natural Sciences and Engineering Research Council (NSERC) for its role in the financial support of this research.

Visiting scholar and friend Tiansheng Zhou has my thanks and appreciation for his assistance, feedback, and ideas. I am also grateful to my fellow graduate students: Yuan Ma, Derek Strembicki, and Bing Yu for their invaluable advice and help during my research. Special thanks to Rilayna Rakoz and Martin Spacek for their contributions to my work over the summer. In addition, the author would like to extend his thanks to Richard Haley, Roy Schmaus, Jim Fearn, Ben Bathgate, Kees den Hartigh, and Ralph Nevins for their technical assistance.

Last but not least, my heartfelt appreciation goes to my family for their understanding and faith in my abilities.

TABLE OF CONTENTS

Chapter	Page
1. INTRODUCTION	1
1.1 Microsystems	1
1.2 Thesis Overview	2
2. AN OVERVIEW OF CMOS MICROMACHINING	5
2.1 Introduction	5
2.2 CMOS Technology	6
2.2.1 CMOS Transistor Theory	6
2.2.2 CMOS Fabrication Process	9
2.2.3 Circuit Examples	13
2.3 Bulk Micromachining	15
2.3.1 Anisotropic Etching	16
2.3.2 Isotropic Etching with XeF ₂	21
2.3.3 Micromachine Examples	25
3. GAS PRESSURE MEASUREMENTS WITH CANTILEVER MICROSTRUCTURES	27
3.1 Introduction	27
3.2 Sensor Design and Fabrication	28
3.3 Experiment Layout and Procedure	34
3.4 Results and Analysis	39
3.4.1 Resonant Frequency	42

3.4.2	Quality Factor	45
3.4.3	Actuating Current	49
3.4.4	Piezoresistor Response	50
4.	SENSOR MODELING AND ANALYSIS	52
4.1	Introduction	52
4.2	Resonant Response Analysis	53
4.3	Piezoresistance	61
4.4	Damping Relation	64
4.5	Non-Linearity and Hysteresis	68
5.	DISCUSSION	76
5.1	Introduction	76
5.2	Pressure Sensitivity	77
5.2.1	Resonant Frequency	78
5.2.2	Quality Factor	79
5.2.3	Actuating Current	80
5.2.4	Piezoresistive Response	81
5.2.5	Damping Relation	82
5.3	CIC Device Applications	83
5.3.1	Industrial Atmospheres	84
5.3.2	Meteorological Environments	85
6.	CONCLUSION AND FUTURE WORK	86
6.1	Gas Pressure Microsensors	86
6.2	Future Work	87

REFERENCES	89
APPENDICES	96

LIST OF TABLES

Table		Page
4.1	Damping ratio, constant, and damping term for resonant response curve fit at 700 Torr.	56
4.2	Statistical analysis of largest response resonant frequency for CIC devices.	59
4.3	Cantilever-in-cantilever thin film material mass and device mass.	60
4.4	Hysteresis effect on maximum deflection frequency for triple CIC type 1 at 0.1 Torr.	72
5.1	Comparison of CIC device sensitivities for pressure measurement based on changes in resonant frequencies.	79
5.2	Comparison of CIC device sensitivities for pressure measurement based on changes in quality factor.	80
5.3	Comparison of CIC device sensitivities for pressure measurement as actuating current is changed to keep device deflection constant.	81
5.4	Comparison of CIC device sensitivities by measuring piezoresistive response at resonance as a function of pressure at constant actuating current.	82
5.5	Comparison of CIC device sensitivities by measuring the “damping relation” at resonance as a function of pressure at constant actuating current.	83

LIST OF FIGURES

Figure		Page
2.1	Physical structure of an n-channel MOS transistor.	7
2.2	Physical structure of a p-channel MOS transistor.	7
2.3	Typical n-well CMOS wafer process.	10
2.4	CMOS inverter schematic and layout.	14
2.5	Simple CMOS current mirror schematic and layout.	15
2.6	Three crystal planes inscribed in a crystalline silicon unit cell with their Miller indices.	17
2.7	Typical anisotropic etch.	18
2.8	Cantilever cutaway during anisotropic etching illustrating undercutting.	20
2.9	Gas trapping during XeF_2 etching.	23
2.10	Gas-phase XeF_2 etching system.	24
2.11	Microphotograph of thermistor.	25
2.12	Microphotograph of single CIC.	26
3.1	Single, double, and triple cantilever-in-cantilever type 1.	29
3.2	Single and double cantilever-in-cantilever type 2.	30
3.3	Actuation of triple cantilever-in-cantilever type 1.	33
3.4	Experiment layout and magnet arrangement.	36
3.5	Bell jar experimental setup.	36
3.6	Signal conditioning circuitry.	37
3.7	Data acquisition setup.	38

3.8	Frequency response for single CIC's at atmospheric pressure and constant actuating current.	40
3.9	Frequency response for double CIC's at atmospheric pressure and constant actuating current.	41
3.10	Frequency response for triple CIC's at atmospheric pressure and constant actuating current.	42
3.11	Frequency at which largest piezoresistive response is observed versus pressure for single CIC's at constant actuating current.	43
3.12	Frequency at which largest piezoresistive response is observed versus pressure for double CIC's at constant actuating current.	44
3.13	Frequency at which largest piezoresistive response is observed versus pressure for triple CIC's at constant actuating current.	44
3.14	Relative piezoresistive response versus frequency for single CIC type 1 at constant actuating current.	46
3.15	Relative piezoresistive response versus frequency for single CIC type 2 at constant actuating current.	46
3.16	Relative piezoresistive response versus frequency for double CIC type 1 at constant actuating current.	47
3.17	Relative piezoresistive response versus frequency for double CIC type 2 at constant actuating current.	47
3.18	Relative piezoresistive response versus frequency for triple CIC type 1 at constant actuating current.	48
3.19	Q versus pressure at constant actuating current.	48
3.20	Actuation current versus pressure for constant piezoresistive response at resonance.	50
3.21	Piezoresistor response at resonance versus pressure at constant actuating current.	51
4.1	Least squares fitting of response of triple CIC type 1 at constant actuating current versus frequency.	57

4.2	Least squares fitting of response of double CIC type 1 and type 2 at constant actuating current versus frequency.	58
4.3	Least squares fitting of response of single CIC type 1 and type 2 at constant actuating current versus frequency.	58
4.4	Polysilicon piezoresistor embedded inside CIC arm.	63
4.5	Damping relation versus pressure for CIC devices at constant actuating current.	68
4.6	Example of hysteresis loop.	69
4.7	Frequency response for a triple CIC for various pressures at constant actuating current.	70
4.8	Frequency response for a triple CIC at 3.0 mA _{pp} constant actuating current	73
4.9	Frequency response for a triple CIC at 1.8 mA _{pp} constant actuating current	74
4.10	Frequency response for a triple CIC at 1.0 mA _{pp} constant actuating current	74
4.11	Frequency response for a triple CIC at 0.5 mA _{pp} constant actuating current	75

LIST OF ABBREVIATIONS AND SYMBOLS

<i>A</i>	Conductor area
Al	Aluminum
AMC	Alberta Microelectronic Corporation
<i>B</i>	Magnetic field vector
BOE	Buffered Oxide Etch
C	Capacitor
CIC	Cantilever-in-cantilever
CMC	Canadian Microelectronics Corporation
CMOS	Complementary Metal Oxide Semiconductor
DI	De-ionized water
DIP	Dual In-line Package
EDP	Ethylene diamine pyrocatechol
ξ	Damping ratio
f_o, ω_o	Resonant frequency
G(x,y,t)	Force per unit area (load)
KOH	Potassium hydroxide
L	Transistor gate length
<i>L</i>	Length vector along current path
LDD	Lightly Doped Drain
LOCOS	Local Oxidation of Silicon
MAP	Manifold Absolute Pressure

MEMS	Microelectromechanical systems
MOS	Metal Oxide Semiconductor
NMOS	n-channel MOS
PMOS	p-channel MOS
R	Resistor
ρ	Area density (mass per unit area)
ρ_l	Viscous damping term
SOG	Spin-on glass
TCR	Temperature Coefficient of Resistance
TMAHW	Tetra-methyl-ammonium hydroxide water
V_{gs}	Gate to Source Voltage
V_{tn}	Threshold voltage (N-channel device)
V_{tp}	Threshold voltage (P-channel device)
W	Transistor gate width
XeF ₂	Xenon Difluoride
ZIF	Zero Insertion Force

Chapter 1

INTRODUCTION

1.1 MICROSYSTEMS

The systems studied in this thesis are known to North Americans as microelectromechanical systems (MEMS) and to Europeans as microsystems, while in Japan they are referred to by the terms micromachining and micromachines [1]. Micromachines are structures that can be fabricated either in large arrays or as discrete devices existing on the scale of microns to millimetres. In general, these systems include both the sensory mechanism, as well as the integrated circuits necessary for signal processing, communication, and control of the microsystem.

Much of the technology used to manufacture MEMS devices comes from integrated circuit (IC) processes, providing miniaturization, multiplicity, and microelectronics (the 3 “M’s”) [2]. Miniaturization is highly desirable. Multiplicity is important as many systems working together can achieve results impossible for a single device. The coordination and control of these elements is accomplished by merging them with on-chip microelectronics [3].

Some of the key structures in MEMS devices today are micro-pumps, valves, gas flow sensors, and pressure sensors [4]. Other structures can take the form of accelerometers, comb-drives, and projection video systems [5].

Commercial interest in microsystems products is driven by their many advantages, which include product miniaturization, high-precision sensing, batch fabrication, integration of sensor components and integrated circuits, low-cost products,

reliability, and a high degree of functionality. Important examples of commercial MEMS product lines that have made a significant impact include accelerometer systems (for example, automobile air bag deployment systems) and pressure sensor systems [4]. In the same way that microelectronics has revolutionized the field of electronics, micromachines could spark the next technology revolution [5].

By early 1995, MEMS industry revenues exceeded \$2.7 billion (U.S.) per year. Approximately 41% of that market belonged to the automotive sector where devices such as the manifold absolute pressure (MAP) sensor are highly developed and widely used. The projected market for pressure sensors in general is \$2.5 billion (U.S.) per year into the next century, making them one of the most important of MEMS devices [6-8].

Most of the silicon pressure transducers in use today employ strain or capacitance sensitive membranes over sealed cavities [7,9-17]. Piezoresistors are the principal tool for detecting the amount of strain (pressure) present, but capacitance devices are more sensitive to changes in pressure and exhibit lower temperature sensitivity [7]. Both of these types of devices are subject to trapped gas expansion as temperature rises. Most devices compensate for this problem by using a second vacuum-sealed reference cavity, which increases the size and complexity of the system. In addition, the creation of sealed cavities is not a simple process for micromachining. Cantilever devices, on the other hand, are some of the least complex micromachines and are relatively simple to fabricate.

1.2 THESIS OVERVIEW

The fundamental operation of a Cantilever-in-Cantilever (CIC) is based on the interaction of alternating current flow within the structure with a static external magnetic

field, resulting in the production of a Lorentz force which provides the torque for deflection of the device. Magnetically actuated CMOS-compatible CIC devices were first developed in our Micromachining Applications and Development Lab at the University of Alberta and reported in 1996 [18]. Characterization of static deflection and exploration of resonant vibration features were undertaken in 1997 [19]. In this thesis, the novel application of these devices as pressure sensors is studied. Of particular interest is the characterization of dynamic deflections at various pressures both above and below atmospheric pressure.

In Chapter 2 a brief overview of CMOS micromachining is given. This overview includes the general theory of MOS transistor operation followed by a summary of standard industry wafer processing for the fabrication of microelectronics. In addition, CMOS micromachining-related processing details are provided and some examples of simple micromachines are given.

The core material of this thesis is contained in Chapter 3. Here the dynamic properties of oscillating CIC's and the changes in these properties with pressure are investigated. Experimental procedure is described and information on sensor design and layout is given.

Chapter 4 deals with modeling the characteristics of the CIC structure as a function of pressure. This model is aptly named the "damping relation". Piezoresistance as a means of measuring cantilever deflection is discussed. A brief comparison of the resonant response of the CIC structure with that of a classical damped harmonic oscillator is made. Information is provided on hysteresis and non-linear effects that were observed for extreme deflections of the CIC devices at high currents and low pressures.

Chapter 5 discusses the results obtained in the previous two chapters and examines possible device applications in industrial and meteorological environments.

Chapter 6 presents a conclusion of the work done and ideas for future chip integration are developed. These ideas include on-board magnetic field generation by inductive planar coils placed around the CIC, and integrated signal conditioning circuitry to improve signal quality and alleviate the need for bulky external equipment.

Chapter 2

AN OVERVIEW OF CMOS MICROMACHINING

2.1 INTRODUCTION

At the time of writing this thesis there exist three methods for creating microstructures: surface, bulk, and complementary metal-oxide semiconductor (CMOS) micromachining. Whereas surface micromachining is the fabrication of micromechanical structures from deposited thin films, bulk micromachining is characterized by the removal of significant amounts of silicon from the substrate. When bulk micromachining is combined with CMOS circuitry a new process called CMOS micromachining is created [20,21]. This new process aims to optimize the use of existing manufacturing techniques in microelectronics to produce inexpensive, reliable, and robust micromechanical structures. Advantages of using CMOS micromachining are its suitability for mass production and the creation of complex circuitry on the same wafer as the micromachined device, thus creating an integrated system on a chip [1,4]. CMOS micromachined devices have exhibited both good performance when used to undertake measurements and superior yields. Disadvantages when using CMOS technology in the production of microstructures is that restrictions are imposed due to the finite number, order of appearance, and thickness of the process layers.

The development of functional micromechanical devices through CMOS micromachining requires knowledge of its constituent components: CMOS technology and bulk micromachining. This chapter is devoted to introducing the reader to the CMOS process and to bulk micromachining.

2.2 CMOS TECHNOLOGY

The transistor was invented in 1947, the bipolar transistor in 1949, but not until the early 1970s did the MOS transistor gain general usage. It then took another ten years before CMOS integrated circuits became the primary technology for VLSI systems design [22]. Today, CMOS technology has achieved extremely large device densities and minute feature sizes. For example, a Pentium II™ microprocessor has 7.5 million transistors, 7 metal layers, and feature sizes of 0.25 microns, on a wafer 10 mm by 10 mm in size.

2.2.1 CMOS Transistor Theory

A metal-oxide-semiconductor (MOS) transistor is a majority-carrier active device through which current flows between the source and the drain, modulated by a voltage applied to the gate [23]. Microcircuits containing the two complementary types of transistors known as n-channel (NMOS) and p-channel (PMOS) belong to the complementary metal-oxide-semiconductor technology referred to as CMOS. The typical structures for NMOS and PMOS transistors can be seen in Figure 2.1 and Figure 2.2.

The n-channel transistor uses electrons as the majority charge carriers and the source terminal for this device is whichever of the two terminals has the *lower* voltage applied to it. When a positive gate-source voltage, denoted V_{gs} , is applied to an n-channel transistor the result is an increase in the number of electrons in the region immediately below the gate. The gate-source voltage, for which the concentration of

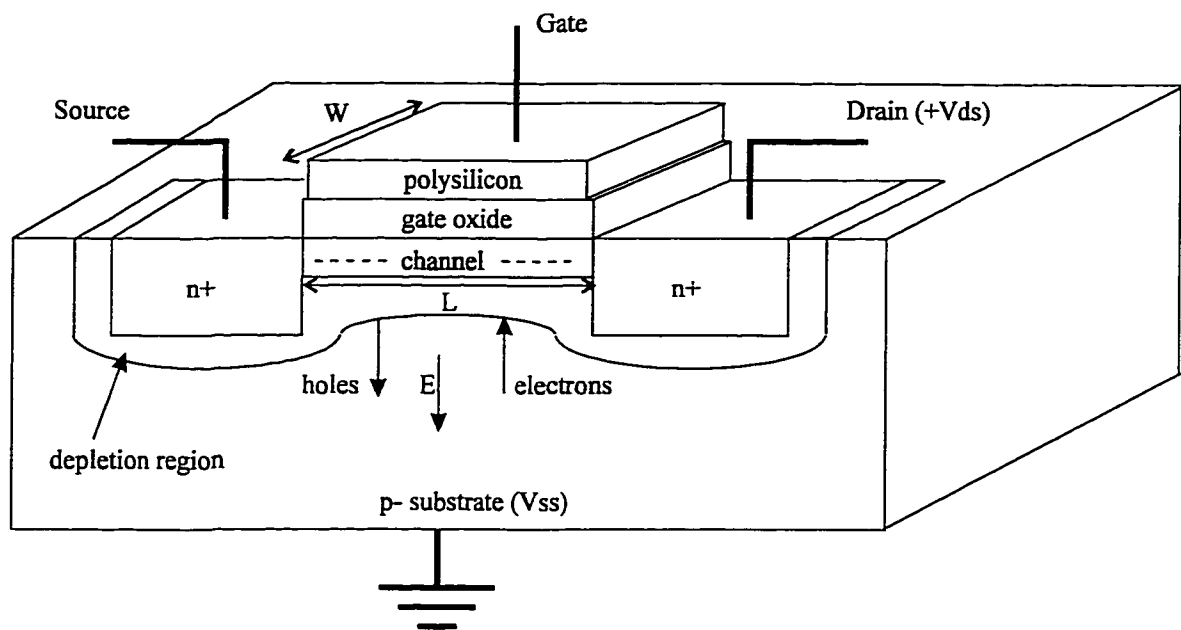


Figure 2.1 Physical structure of an n-channel MOS transistor.

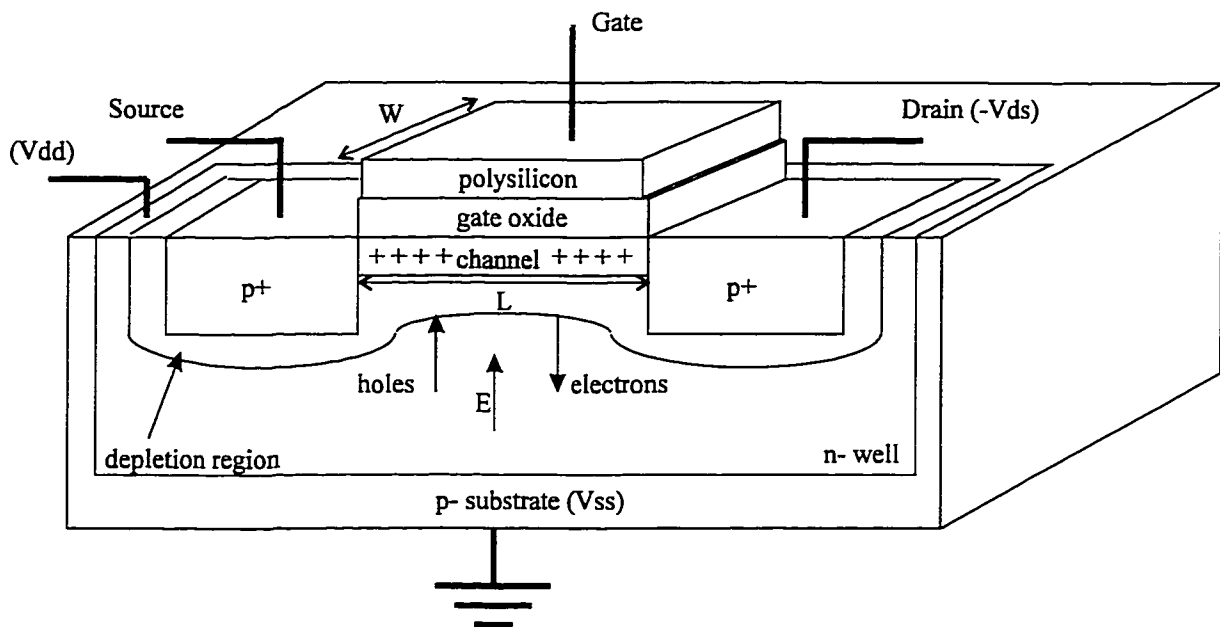


Figure 2.2 Physical structure of a p-channel MOS transistor.

electrons under the gate is equal to the concentration of holes in the substrate far from the gate, is known as the threshold voltage (V_{tn} for n-channel devices). When $V_{gs} \geq V_{tn}$, the channel is strongly inverted and current, I_{DS} , flows from the drain to the source. Weak inversion occurs for values of V_{gs} more than 100 mV below V_{tn} , no current flows from the drain to the source, and the transistor is assumed to be inactive or off. Moderate inversion, also called the linear region, is the region between strong and weak inversion where some current flows from drain to source.

The operation of p-channel transistors is analogous to that of the n-channel transistors with a few exceptions: whichever of the two terminals has the *higher* voltage applied to it is now called the source, the threshold voltage is denoted V_{tp} and is negative, and all voltages with respect to the substrate must be negative for active operation. Lastly, the current flows from source to drain. That is, the p-channel transistor is active (strong inversion) for $V_{sg} \geq V_{tp}$ and inactive or off (weak inversion) for $V_{sg} < V_{tp}$ by 100 mV or more. The linear region (moderate inversion) plays an important role in the operation of analog circuits comprised of MOS transistors.

The gate is made of a thin layer of polycrystalline silicon (polysilicon) under which is a thin insulating layer of silicon dioxide (gate oxide). The source and drain regions in Figure 2.1 are heavily n^+ doped while those of Figure 2.2 are heavily p^+ doped. The substrate is moderately p-type doped. A moderately n-type doped well formation is required under the p-channel device (Figure 2.2). There is no physical distinction between the drain and source regions because of their inherent structural symmetry.

A positive voltage is applied between the source and the drain in the normal operation of MOS transistors. No current flows (n-channel devices) with zero gate bias

as the source and drain are insulated from each other by two reversed-biased pn junctions and the channel is weakly inverted. The transistor enters the linear region (moderate inversion) for $V_{gs} > \text{zero}$ as the gate voltage produces an electric field E that attracts electrons and repels holes with small current flow possible. A sufficiently large gate voltage ($V_{gs} \geq V_{tn}$) will change the channel under the gate oxide from p-type to n-type, hence providing a conduction path between source and drain. The transistor is now in the active region (strong inversion). Similarly, for p-channel devices, a conduction path is created when the gate voltage is made sufficiently negative ($V_{sg} > V_{tp}$). Conduction now results from the movement of holes in the channel.

2.2.2 CMOS Fabrication Process

The sequence of processes involved in the fabrication of CMOS circuitry is called wafer processing. Wafer processing involves doping the semiconductor, growing insulating and conducting films in a sequence of layers, patterning the layers using lithographic techniques, and etching exposed materials. These fundamental steps are repeated over and over in various orders during the process sequence. Figure 2.3 illustrates the major steps involved in a typical n-well CMOS process involving one polysilicon layer and two metal layers.

The n-well process begins with a lightly doped p-type substrate and follows with the creation of the n-well, in which a p-channel transistor will reside. The n-well is created by ion implantation or deposition and diffusion through the first mask (Figure 2.3a).

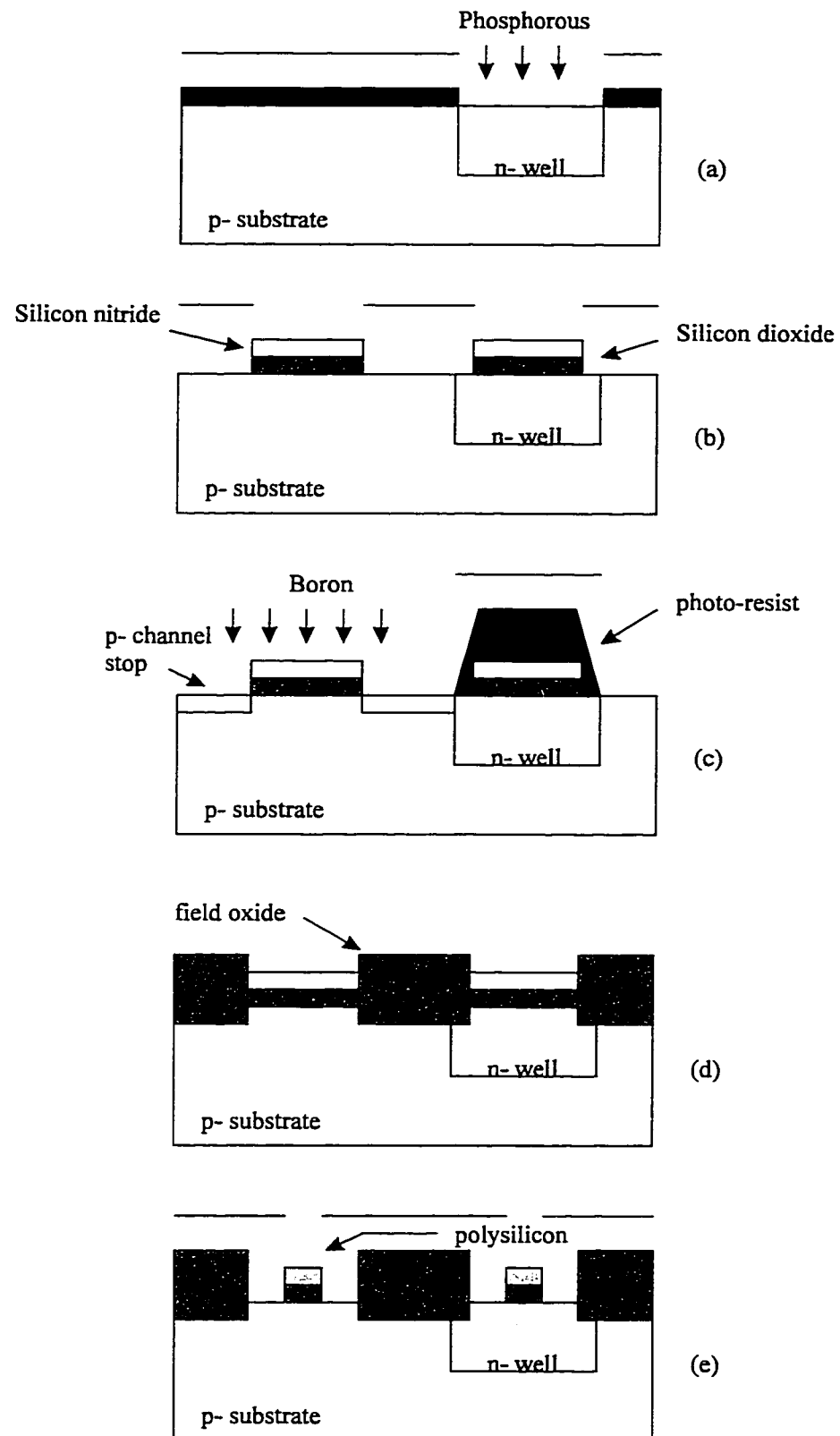


Figure 2.3 Typical n-well CMOS wafer process

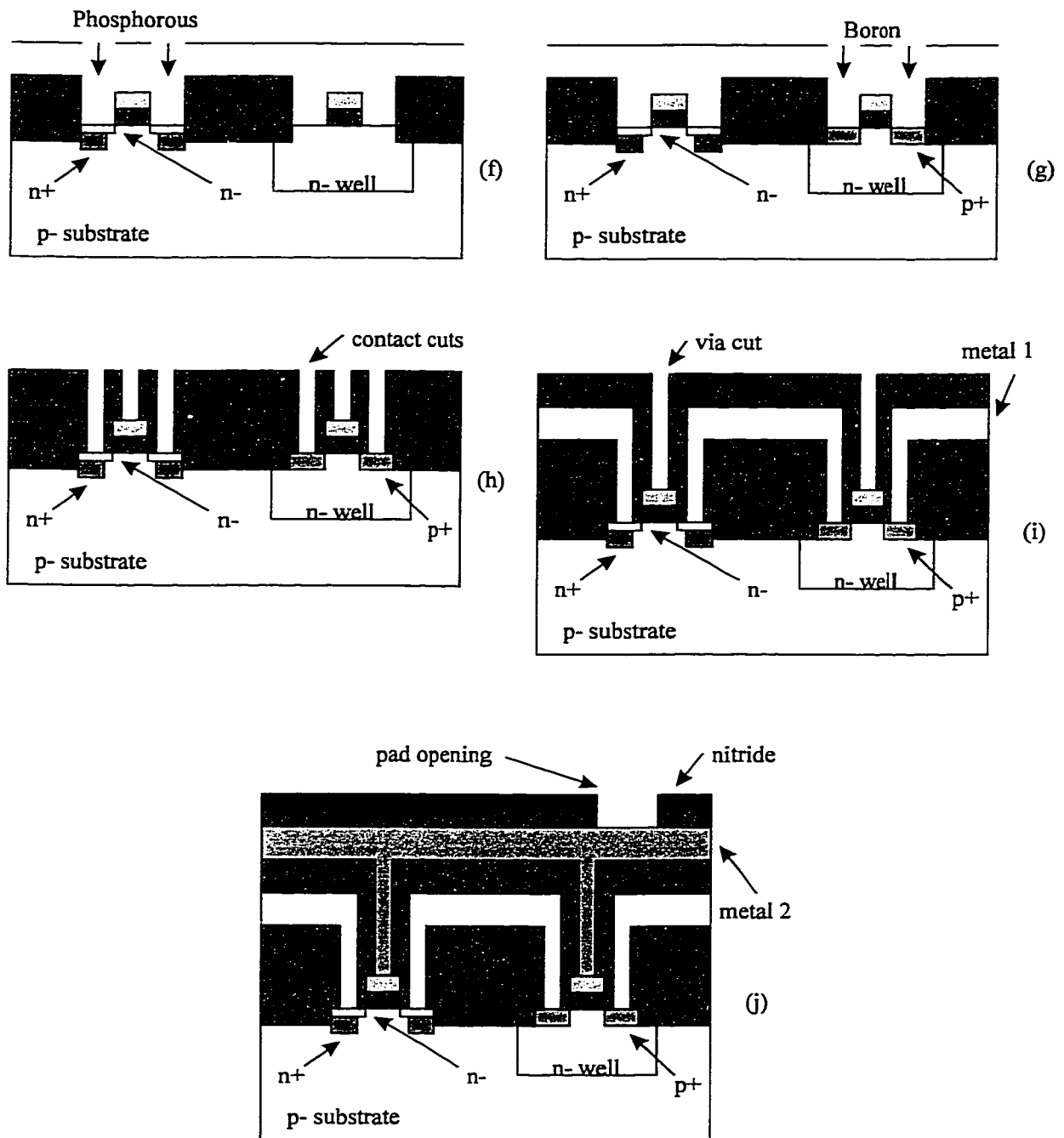


Figure 2.3 (continued) Typical n-well CMOS wafer process

The next mask defines regions needed for transistor gates and diffusion areas for source/drains, known as the "active area" (Figure 2.3b). In this area a thin silicon dioxide (SiO_2) layer is grown and covered with a thin layer of silicon nitride (Si_3N_4). The nitride layer is used in the next two process steps as a masking layer.

A photoresist mask is then used to direct the channel-stop implantation. Regions are thus created where no n-channel transistors (Figure 2.3c) will exist. These regions are implanted with boron to help electrically isolate unrelated transistor terminals.

The photoresist used in the channel-stop implant is then stripped. The $\text{SiO}_2/\text{Si}_3\text{N}_4$ layers still define the active regions. Figure 2.3d shows a thick field oxide that is grown vertically and horizontally over the wafer surface not masked by the oxide/nitride. This oxide adds to the electrical isolation between transistors created by the boron implant. The technique for growing field oxide on the wafer is called local oxidation of silicon or LOCOS.

The polysilicon gate definition is completed by stripping the silicon nitride layer, depositing polysilicon over the gate oxide, and patterning it (Figure 2.3e). Typically, chemical vapour deposition is used to place the polysilicon on the wafer.

The n^+ doped regions are created by first creating a light n^- doping of the substrate over the source/drain areas devoid of polysilicon. This is followed by a heavy n^+ doping of the p^- substrate. This lightly doped drain structure (LDD) is used to reduce hot carrier effects (Figure 2.3f). Using a spacer oxide over the polysilicon gate before the heavy doping leaves a slight space between the n^+ regions and the edge of the polysilicon gate. Keeping the spacer oxide yields a transistor resistant to hot-electron effects.

The next step (Figure 2.3g) is the doping of the p^+ diffusion regions for the p-channel devices. This is followed by a growth of oxide over the surface of the wafer. The definition of contact cuts is achieved (Figure 2.3h) by etching any oxide down to either the polysilicon gate or the substrate surface. This allows the metal interconnect layers to contact the diffusion (drain/source) regions as well as the gate.

The wafer is covered with a first layer of metal (Al) and selectively etched to produce the desired circuit interconnections. Another oxide layer is grown for insulation and via cuts are made where the second metal layer is designated to contact the underlying first metal layer or polysilicon gate (Figure 2.3i).

Finally, a second metal layer is deposited on the wafer, selectively etched, and a protective passivation layer deposited (Figure 2.3j). The passivation layer actually consists of two layers. The first layer is a spin-on-glass (SOG) oxide layer. This is followed by a nitride layer which is ideal for preventing the ingress of contaminants such as water vapour. Regions requiring contact between the top metal layer and the external world (for example, bonding pads) are etched through the passivation layer. Additional information on the CMOS process can be found in [24].

2.2.3 Circuit Examples

Integrated circuits are designed for either digital or analog applications. One example of a digital circuit is the CMOS inverter that outputs logical ones and zeros for an input of logical zeros and ones. The schematic and layout for a CMOS inverter is shown in Figure 2.4. An inverter consists of two transistors: one n-channel and one p-

channel connected in series. The input signal is delivered to both gates and the output comes from both drains.

Figure 2.5 illustrates the schematic and layout for a simple CMOS current mirror, also consisting of two transistors (both n-channel). A current mirror is designed to provide a fixed current independent of load resistance. This is achieved by the current source and transistor Q1 in what is called a diode configuration. Whatever current flows through Q1 will also flow from drain to source in Q2. Further details are given in [25].

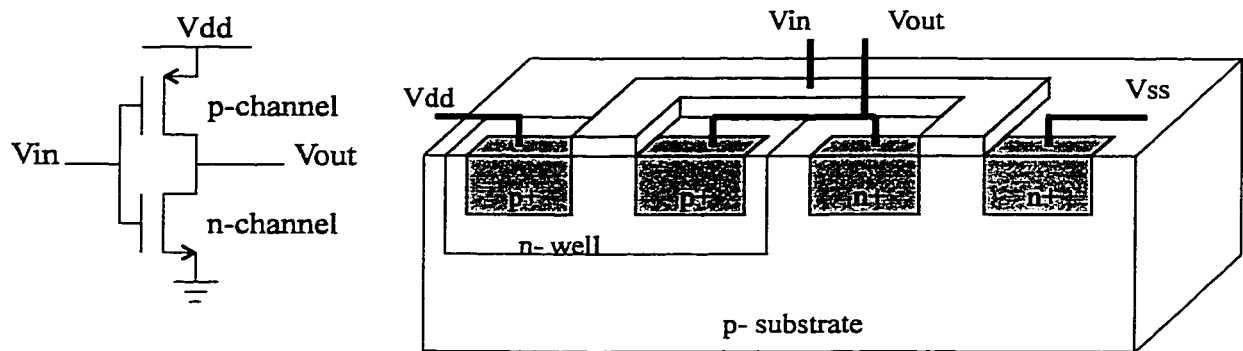


Figure 2.4 CMOS inverter schematic and layout.

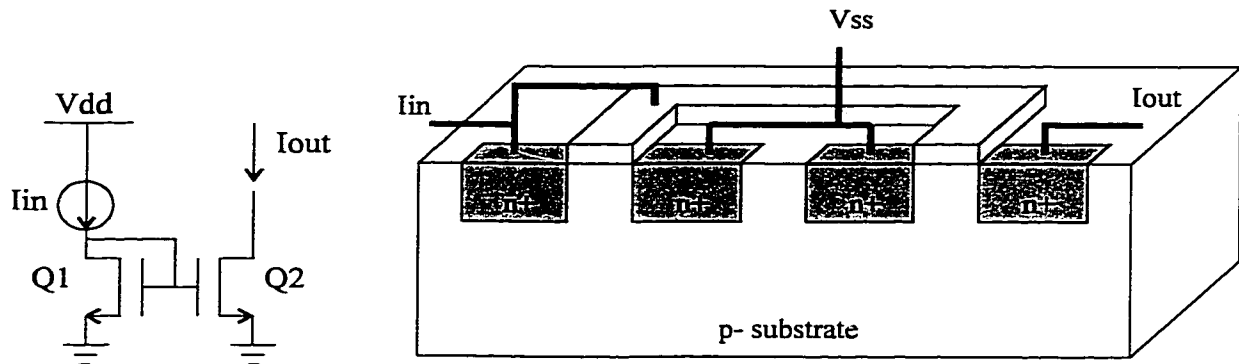


Figure 2.5 Simple CMOS current mirror schematic and layout.

2.3 BULK MICROMACHINING

Bulk micromachining is the fabrication of three-dimensional micromechanical structures out of silicon, polysilicon, silicon dioxide, silicon nitride, and other materials [26]. This fabrication is achieved by the selective removal of large amounts of silicon from a substrate. The objective of doing this can be to form membranes, trenches, holes, or to undercut structures, thus enabling them to physically move. The process of removing material in the creation of these devices is called etching, while the chemical substance interacting with the material to be removed is called the etchant. Etchants are present in the form of aqueous solutions (wet) or gas vapours (dry or plasma) and are either anisotropic or isotropic in nature. When the overall fabrication process sequence is designed carefully this etching can be compatible with on-wafer circuitry. An example of this is CMOS micromachining where both micromachines and microelectronics reside on the same wafer.

Any silicon surface exposed to air experiences the growth of a thin oxide layer. Just prior to etching it is good practice to have wafers dipped in a buffered oxide etch (BOE) for 10-15 seconds to remove this oxide layer. A solution of BOE consists of diluted hydrofluoric acid (HF) combined with NH_3F to provide a neutral pH. In the case of pre-fabricated CMOS chips, a 2% HF solution can be substituted for BOE. This is done since BOE has been reported to etch aluminum which is an important component of bonding pads [19]. Etching without the removal of this native oxide will reduce the efficiency of the etchant and produce rough etch surfaces.

2.3.1 Anisotropic Etching

Anisotropic etching is the directional-dependent etching of material based on etch rates that vary with crystal plane orientation. This form of etching is widely used for micromachining and is well described in the literature [27]. The process of anisotropic etching is fundamentally a charge-transfer procedure where dopant types and atomic density of the etched material determine the etch rates. To understand how anisotropic etching occurs requires some knowledge of the crystallographic planes present in a silicon crystal. Figure 2.6 illustrates three important crystal planes found in crystalline silicon as unit cubes in cartesian coordinates [29]. These planes are described by Miller indices: the smallest integer values equal to the reciprocals of the distances from the origin to the points of plane intersection with the axes. It is found that the (111) surfaces experience the lowest etch rate. The reason is thought to be that they exhibit the highest density of atoms. Further information can be found in [27,28].

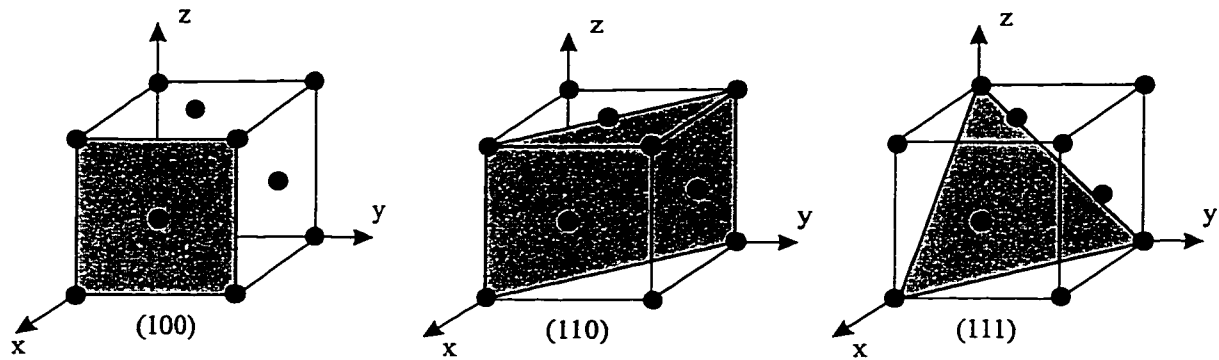


Figure 2.6 Three crystal planes inscribed in a crystalline silicon unit cell with their Miller indices.

Silicon wafers are manufactured in three common orientations, $\langle 100 \rangle$, $\langle 110 \rangle$, and $\langle 111 \rangle$, with $\langle 100 \rangle$ being exclusively used in CMOS technologies. The angle brackets denote that these indices reflect wafer orientations. However, this bracketing convention is not yet standardized throughout the literature. The most frequently used convention is (abc) for a particular crystal plane and $\langle abc \rangle$ for the group of parallel unit vectors associated with the (abc) crystal plane.

Before etching takes place, the substrate is covered by a layer of mask and patterned to expose only certain areas of the substrate to the etchant. Different size pit geometries will be produced depending on the orientation of the crystal. The profile of a typical (wet) anisotropic etch can be seen in Figure 2.7. The final pit is bounded by (111) plane surfaces due to their high density of atoms.

Undercutting results from substrate etching under the mask and plays an important role in the fabrication of suspended microstructures. Vertical etch stop layers, such as a heavily doped boron buried layer, are used to stop or slow the amount of etching downward into the substrate. Undercutting occurs when the vertical etch stop

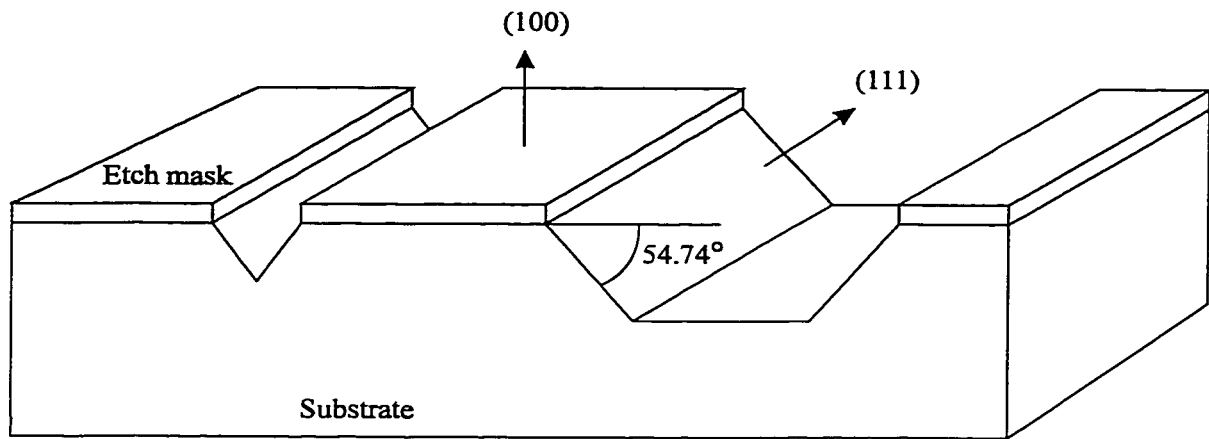


Figure 2.7 Typical anisotropic etch.

layer or (111) surface are encountered by the etchant resulting in the horizontal removal of substrate. Mitered corners present in the mask openings will also produce undercutting. Shown in Figure 2.8 is how undercutting can be achieved via anisotropic etching. At first, the silicon substrate is etched vertically downwards until (111) planes are reached. Concurrently, undercutting begins on the edges and corners at a rate determined by etch ratios for various crystal planes and the maximum etch rate. If sufficient time is allowed to pass, convex corners will continue to undercut until the etchant reaches the (111) surfaces producing a pyramidal shaped pit. Further etching causes the cantilever to be released, meaning the underside of the microstructure is no longer attached to the substrate.

The size of the mask openings is an important issue in undercutting. Release of the structure can be delayed or not be possible if the mask opening is too narrow to allow a sufficient flux of etchant. The way around this problem is longer etch times and/or larger openings.

Some examples of anisotropic etchants are EDP (ethylene diamine-pyrocatechol-water), TMAHW (tetramethylammonium hydroxide-water), and KOH (potassium

hydroxide-water). These etchants are composed of a primary component, a complexing agent, and a diluent (water). These wet anisotropic etchants can be highly selective in the materials that they etch.

The most common mix for EDP is 750 mL of ethylene diamine ($\text{NH}_2\text{-CH}_2\text{-CH}_2\text{-NH}_2$), 240 g pyrocatechol ($\text{C}_6\text{H}_4(\text{OH})_2$), 240 mL de-ionized water (DI), and 6 g pyrazine ($\text{C}_4\text{H}_4\text{N}_2$) [27]. EDP will not etch gold, chromium, silver, or tantalum. Etch rates for silicon are reported at 1.4-1.6 $\mu\text{m}/\text{min}$ at 119°C in the (100) direction [19]. Anisotropy ratios of 40:1 for silicon (100) to (111) directions can also be expected [30]. Aluminum and silicon dioxide etch rates are typically 10 nm/min and 10 nm/hr, respectively. The etch rate is dopant dependent; regions highly doped with boron ($> 7 \times 10^{19} \text{ cm}^{-3}$) experience almost no etching. EDP is a highly dangerous nerve toxin and carcinogenic etchant that has now been banned in most commercial fabrication facilities. It should be kept in a pure nitrogen environment as exposure to oxygen forms benzoquinone that will cause uncontrollable etch rate increases and a darkening of the solution. Also, after etching with EDP the wafers should be rinsed in DI water for at least 24 hours to prevent the forming of a benzoquinone residue on the substrate and hence further etching.

The combination of TMAH ($\text{N}(\text{CH}_3)_4\text{OH}$) and water to make TMAHW results in another anisotropic etchant commonly used for micromachining. A characteristic of TMAHW is that it not only etches silicon but also aluminum, and shows high selectivity for silicon dioxide and silicon nitride. That is, the etch rates for silicon dioxide and silicon nitride are much less than those for silicon and aluminum. TMAHW is a strong base that is both stable and colourless. It can cause severe irritation to skin, eyes, and mucous membranes. It is also poisonous when absorbed through the skin. Since most

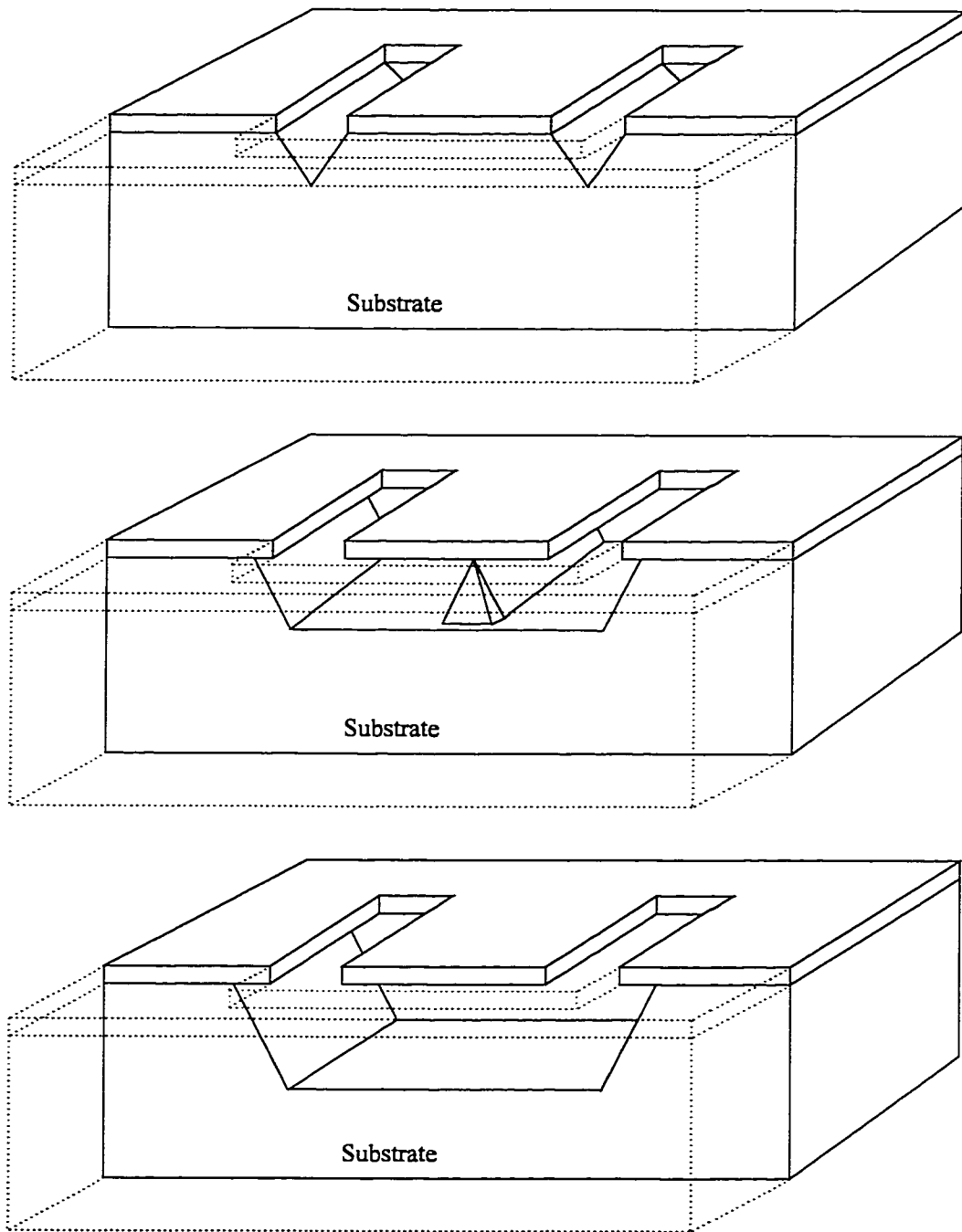


Figure 2.8 Cantilever cutaway during anisotropic etching illustrating undercutting.

CMOS processes use Al metal layers it is important to protect them from the etchant. This is particularly true for the bonding pads. Some researchers utilize TMAHW in the creation of microstructures by not only etching the silicon substrate but also some of the metal layers (commonly known as sacrificial metal etching). Literature suggests that adding silicon to TMAHW will greatly decrease its etch rate of aluminum and, hence, reduce the requirement for pad protection [19,30]. Etching parameters for TMAHW are a silicon etch rate of $1.0 \mu\text{m}/\text{min}$ at 90°C for 25 wt.% solutions, anisotropy ratios from 10:1 to 35:1 for the (100):(111) planes, and etch-stop for boron-doped regions in excess of 10^{20} cm^{-3} .

Finally, the third popular anisotropic (wet) etchant is KOH. Silicon etch rates of $8.5 \mu\text{m}/\text{min}$ at 100°C , anisotropy ratios (100):(111) of 400:1, and boron etch-stops for concentrations greater than 10^{20} cm^{-3} have been documented [30]. This etchant is a poison by ingestion, is a skin irritant, and can be very corrosive to the eyes and mucous membranes. KOH is not recommended as an etchant with only silicon dioxide as the masking material since it etches the oxide at a much faster rate than the silicon itself. The mask for this etchant is usually silicon nitride. This etchant is commonly used for surface micromachining where oxide layers are sacrificed in the fabrication of microstructures. KOH is not a desirable etchant where integrated electronics exist since potassium ions can be trapped in active devices and cause aging effects [30].

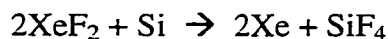
2.3.2 Isotropic Etching with Xenon Difluoride

Isotropic etching is the removal of material independent of crystallographic-orientation. That is, etching occurs in all directions at the same rate. As a silicon etchant,

xenon difluoride (XeF_2) etches isotropically, has high selectivity, and produces gentle dry reactions. XeF_2 is a versatile etchant in the fabrication of micro-structures and its use is rapidly increasing, as evidenced by the growing amount of literature available on this material [31-35].

At standard temperature and pressure, XeF_2 exists as a white solid material. Exposing solid XeF_2 to pressures less than 4 Torr at room temperature (its sublimation pressure) will cause it to rapidly sublime and isotropically etch silicon without external excitation. This ability to etch without excitation is the most likely cause of the high selectivity of XeF_2 to many metals, dielectrics, and polymers used in traditional integrated circuit fabrication [31]. Thus, XeF_2 is easy to use with CMOS micromachining. XeF_2 has very low etch rates for aluminum, chromium, titanium nitride, tungsten, silicon, dioxide, photoresist, or silicon carbide. Discrepancies exist between the reported etch rate for silicon nitride [20,31]. Selectivities have been observed for etching titanium:silicon, 85:1, and molybdenum:silicon, 6:1, respectively. Native oxides will not prevent etching but can slow the onset of etching.

The overall silicon/xenon difluoride reaction equation is:



Other etch products such as SiF , SiF_2 , SiF_3 , and Si_2F_6 have been reported but only in trace amounts [31]. The reaction is exothermic so substrates should not be thermally isolated during etching. Moisture on the chip, which causes HF formation with exposure to XeF_2 gas, is a safety hazard and can result in silicon dioxide etching. Also, water presence can occasionally lead to film formation believed to consist of a silicon-fluorine polymer that inhibits etching.

The etch rate for XeF_2 is dependent on the etch window dimensions and etch depth is not a linear function of time. Bulk etch rates are much higher during the initial 15 seconds and drop off dramatically after 4 minutes. Typical etch rates are 1-2 $\mu\text{m}/\text{min}$ vertically and 2-3 $\mu\text{m}/\text{min}$ laterally [33]. Undercutting outperforms etching depth after a certain time, possibly due to "gas trapping", as depicted in Figure 2.9. That is, given a small etch opening and a large etching surface area, the XeF_2 molecules become trapped beneath the undercut mask, resulting in a tendency to etch horizontally rather than vertically. Etching efficiency can be improved by protecting the wafer backside and edges from exposure to XeF_2 gas and also by ensuring the absence of water vapour.

All microstructures used in this thesis were etched with gas-phase XeF_2 . Figure 2.10 illustrates the experimental apparatus used to achieve the post-processing etching. All devices were packaged and bonded first, before etching, as the bonding pads are situated near the wafer's edge and hence were partially undercut during the etching process. Bonding after etching will cause the undercut pads to fracture thus reducing yield. During a normal etching cycle the expansion chamber is filled with gas-phase sublimated crystals from the charge chamber, while the etch chamber is pumped down.

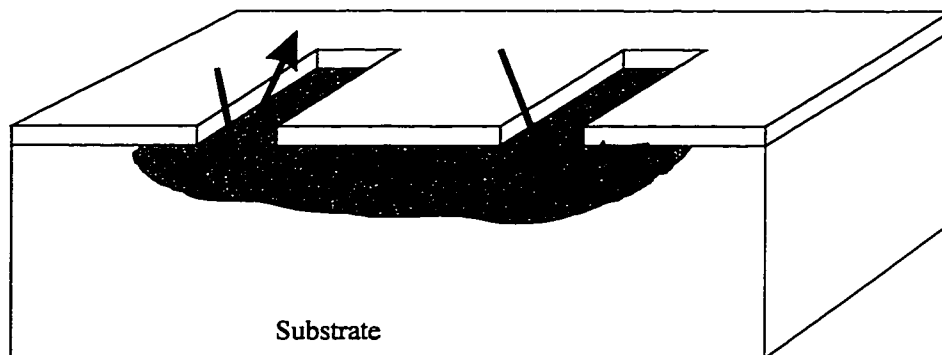


Figure 2.9 Gas trapping during XeF_2 etching.

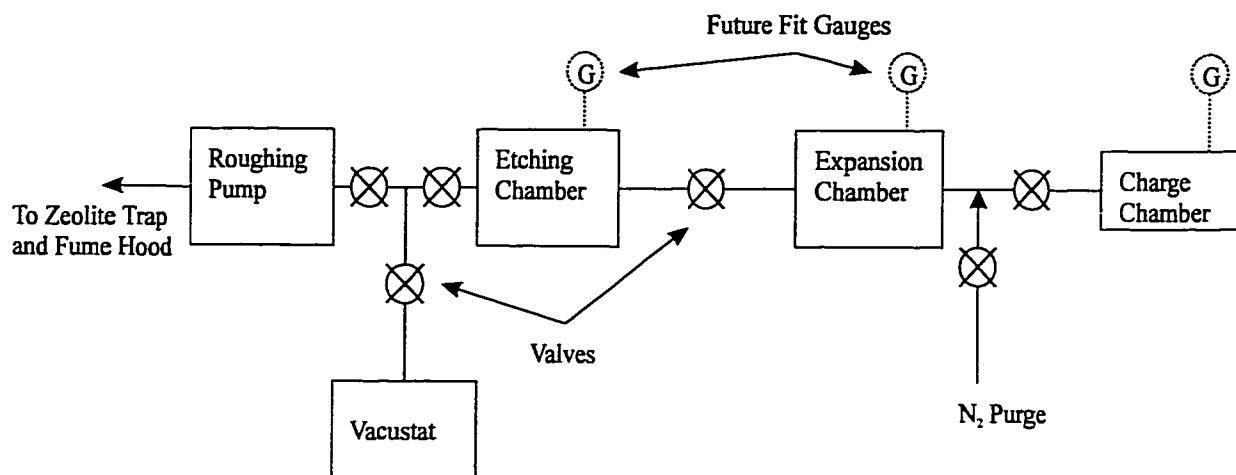


Figure 2.10 Gas-phase XeF_2 etching system.

The expected optimal or target pressures for this are 3 Torr in the expansion chamber, and 0.02 Torr in the etch chamber. Upon reaching the target pressures, the expansion chamber is isolated from the charge, the etch chamber from the pump, and the valve connecting expansion and etch chambers is opened. Pressure equalization occurs rapidly, and the etching commences. A slight rise in pressures during etching is due to the 50% increase in the number of moles of etched product over the number of moles of reactant gases. After etching, the etch and expansion chambers are pumped out, and the process is repeated. Each etch and expansion pulse lasts 1-2 minutes and a nitrogen purge of the system (except for the charge chamber) is carried out after every fourth pump down. This purge is necessary to remove any byproducts of etching or contaminants that have accumulated.

The system used for the etching of the microstructures used in this thesis utilized manual valves that resulted in a repetitive and time-consuming process for the user. A future improvement under development is computer-controlled etching with solenoid-actuated valves.

2.3.3 Micromachine Examples

Two simple examples of CMOS micromachines are shown in Figure 2.11 and Figure 2.12. The first example is a microphotograph of a thermistor whose resistance changes with temperature according to the polysilicon element's temperature coefficient of resistance (TCR). The entire device measures $100\text{ }\mu\text{m}$ by $100\text{ }\mu\text{m}$ and was isotropically etched with XeF_2 to thermally isolate the structure from the substrate. The second example (Fig. 2.12) is a microphotograph of a single cantilever-in-cantilever (CIC) prior to etching. This device is actuated by an alternating current that is passed through the arms in the presence of a constant magnetic field. The resulting Lorentz force at the end of the cantilever deflects the CIC up and down out of the plane of the wafer. Piezoresistors in the base of the arms detect this motion. Uses for the CIC include pressure sensing, as described in this thesis, magnetic field sensing [36], and thin film monitoring [37].

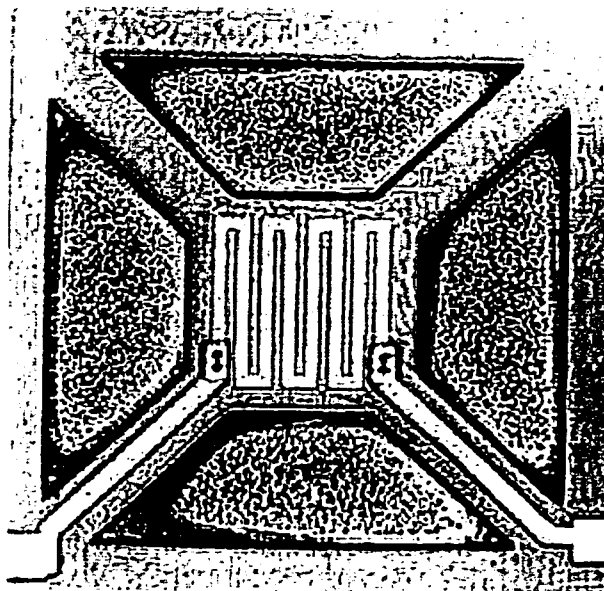


Figure 2.11 Microphotograph of unetched thermistor.

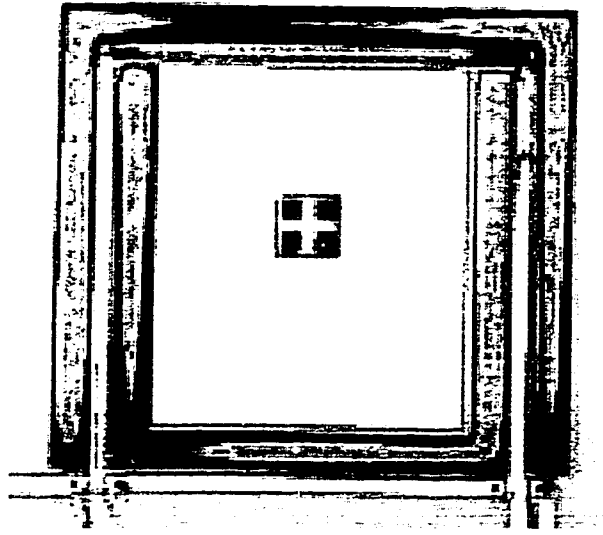


Figure 2.12 Microphotograph of unetched single CIC.

Chapter 3

GAS PRESSURE MEASUREMENTS WITH CANTILEVER MICROSTRUCTURES

3.1 INTRODUCTION

Microelectromechanical systems (MEMS) have played a major role in automotive engine control since 1979 in the form of manifold absolute pressure (MAP) sensors. Virtually all automobiles on the road today have one of these devices in their electronic engine control system operating at pressures ranging from hundreds to thousands of Torr. As automotive engines improve, the requirements for MAP sensors have become more stringent [8]. Hence, there exist important applications for accurate, cheap, robust, and reliable absolute pressure sensor microstructures.

Such a microstructure exists in the form of a magnetically actuated cantilever-in-cantilever (CIC) device which is the object of investigation of this thesis. Absolute pressure variations from 15 to 1450 Torr (0.02 to 1.91 atmospheres) were created and the dynamic properties of the CIC were investigated throughout this pressure range. A CIC is a nested cantilever microstructure that is actuated by a Lorentz force. This force is the result of the interaction of an alternating current flowing through the device and a constant external magnetic field.

The purpose of this chapter is to describe the design and fabrication of the CIC. Following this are the details of the experiments conducted and a presentation of the results obtained. These results include observed changes in the oscillatory behaviour of the structure, such as:

- resonant frequency
- quality factor
- actuating current for constant piezoresistive response
- piezoresistive response for constant actuating current

as functions of pressure within the stated pressure range. These measurements were carried out on five variations of the CIC device to obtain a broad range of data and allow the development of a realistic model for these devices.

3.2 SENSOR DESIGN AND FABRICATION

A cantilever is best described as a diving board over an empty swimming pool. The nesting of cantilevers within one another produces a structure known as a cantilever-in-cantilever. Such a device is used in this thesis for pressure sensing. The advantage of a CIC structure over a simple cantilever is that overall device stiffness is reduced, which leads to an increase in the amount of deflection that may be achieved for a given Lorentz force/unit length.

Three types of CIC devices were fabricated and are shown in Figure 3.1. The first device is known as a single CIC type 1 (Figure 3.1a) since it consists of a single nested cantilever. Similarly, the second and third structures are called double (Figure 3.1b) and triple (Figure 3.1c) CIC's type 1 after their respective number of nested cantilevers. The main reason for using double and triple CIC's rather than single ones is the relative ease with which large deflections can be generated, which in turn permits these devices to react to very small pressure changes.

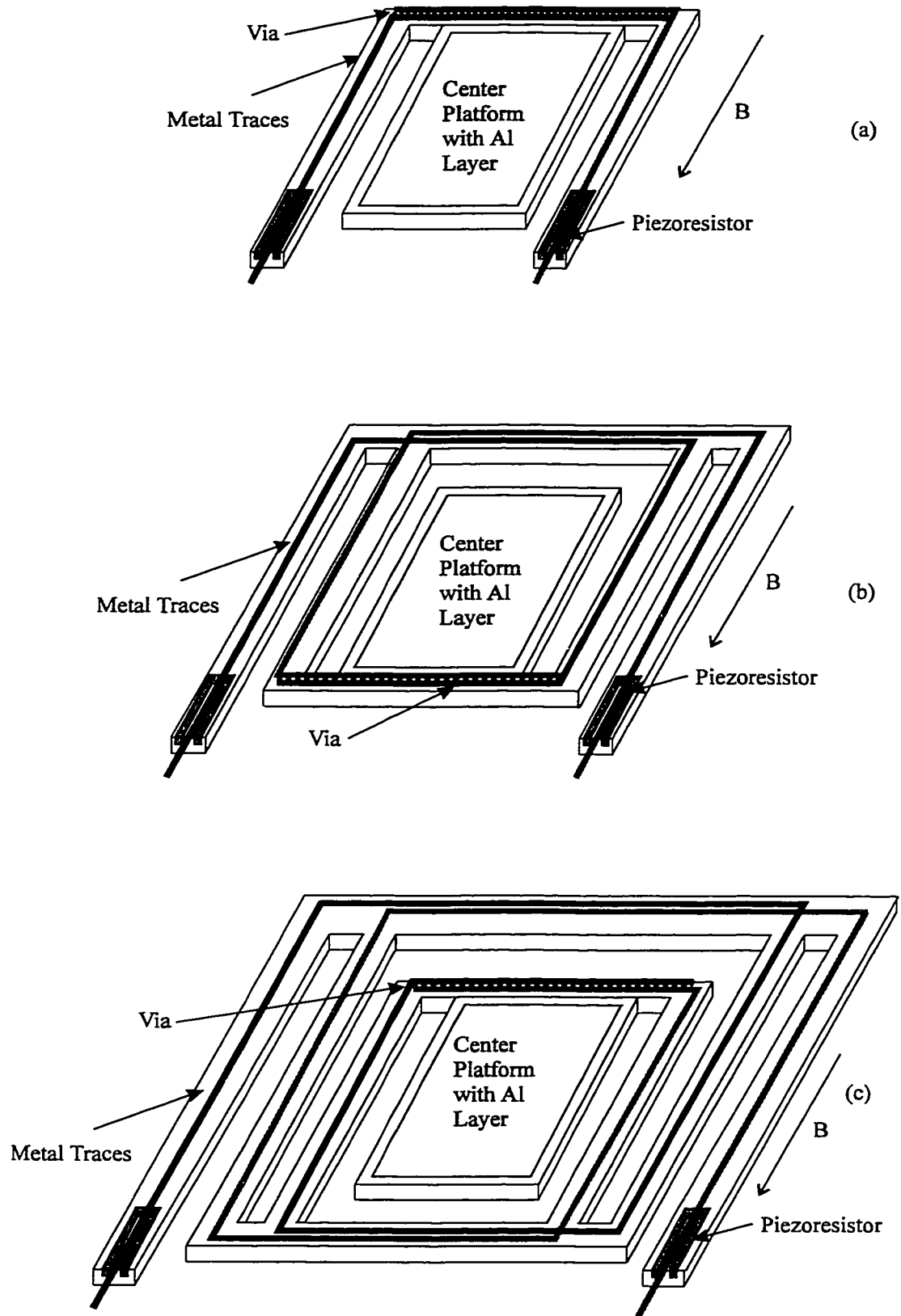


Figure 3.1 Single, double, and triple cantilever-in-cantilever type 1.

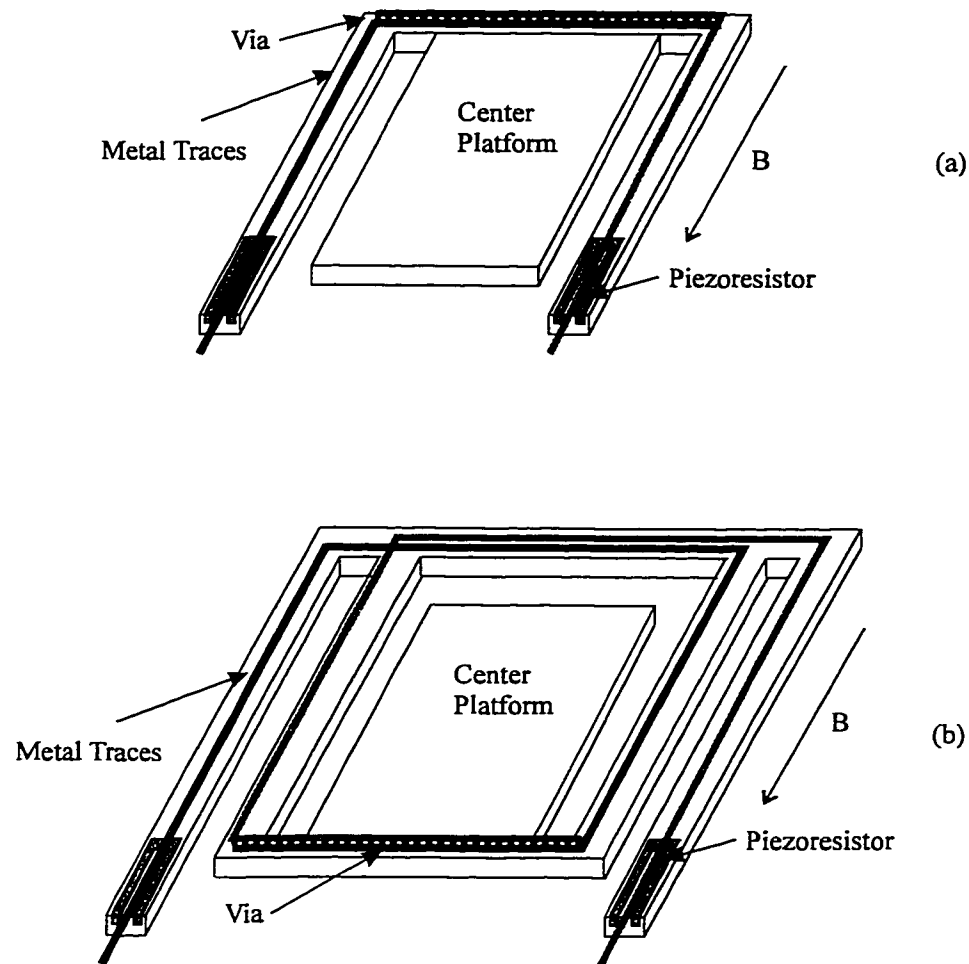


Figure 3.2 Single and double cantilever-in-cantilever type 2.

In addition, a variation on the single and double cantilever-in-cantilever devices was developed and termed type 2. These structures are shown in Figure 3.2, with the only difference between these devices and type 1 being the absence of a layer of metal on the center platform. The absence of this layer of metal does not change the stiffness or surface area of the sensor, but instead results in a reduction of the overall sensor mass. This was done for two reasons: first, to compare the performance between two CIC structures under the same conditions differing from each other only in mass; and second,

to observe the effect of differences in post-process etching and release, as discussed in the previous chapter, upon cantilever performance, since the center platform of the type 2 device is transparent.

Each of the devices has the same size center platform with the dimensions of 190 μm wide by 224 μm long. They also have the same arm width of 16 μm . There are, however, more sets of arms on the double and triple CIC's than on a single CIC. These microstructures are constructed from a sandwich of silicon dioxide, silicon nitride, and aluminum layers as shown in Figure 2.3 of Chapter 2. The overall thickness of both the arms and center platform is about 5 μm after etching. Polysilicon was placed at the base of the outermost arms of each cantilever-in-cantilever and connected in series to provide a piezoresistor (see Figure 3.1). This enables the measurement of the amount of deflection of the structure. Each piezoresistor is 88 μm long in the shape as shown, resulting in a current path approximately 175 μm in length. Opening regions to the substrate between the arms required the use of four design layers standard to CMOS processes. The first layer is an *active region* where no field oxide is grown, and is followed by *contact cuts* (absence of polysilicon and gate oxide). *Vias* were then applied to regions where no intermetal oxide is to be grown. Finally, the *passivation layer* was placed in areas free of spin-on-glass and nitride, as described in the previous chapter.

The actuation of a cantilever-in-cantilever is the result of a Lorentz force produced by the interaction of a magnetic field with a time-varying current. Figure 3.3 illustrates this principle for the case of a triple CIC device. The Lorentz force is defined as:

$$\vec{F} = i\vec{L} \times \vec{B} \quad (3.1.1)$$

where \vec{F} is the resulting force, i the time-varying current in the end of the cantilever of length \vec{L} , and \vec{B} is the magnetic field oriented as depicted in the Figure 3.3. When the force at the end of the cantilever is downward, the force at the other end is upward, thus contributing to cantilever deflection. There is no actuating force on the side arms. The addition of a second metal layer, overlapping but electrically isolated from the first metal layer, provides two current loops through the arms and thus doubles the Lorentz force. An alternating current (AC) sent through the device will cause it to oscillate at the applied frequency. At the resonant frequency of the device, deflections can reach 75° [38].

All of the devices used in this study were fabricated on a 9 mm^2 die by MITEL Corporation with their $1.5 \mu\text{m}$ CMOS process. This process provides two metal layers (aluminum) and two polysilicon layers in the manufacturing of very large scale integrated circuits and micromachines. Fabrication space was made available by the Canadian Microelectronics Corporation (CMC). The layout was achieved with the use of both Cadence and Mentor Graphics, each a high quality CAD tool based on the UNIX environment. The layout data is submitted to the industrial foundry via CMC in GDS II (stream) file format.

The nature of the manufacturing process used to fabricate these devices means that only one post-processing step was required, which involves the undercutting and release of the CIC's by isotropic gas-phase pulse etching with xenon difluoride (XeF_2). The procedure for isotropic etching with xenon difluoride was carried out in accordance with that detailed in Chapter 2. Due to the high selectivity of XeF_2 all etching took place

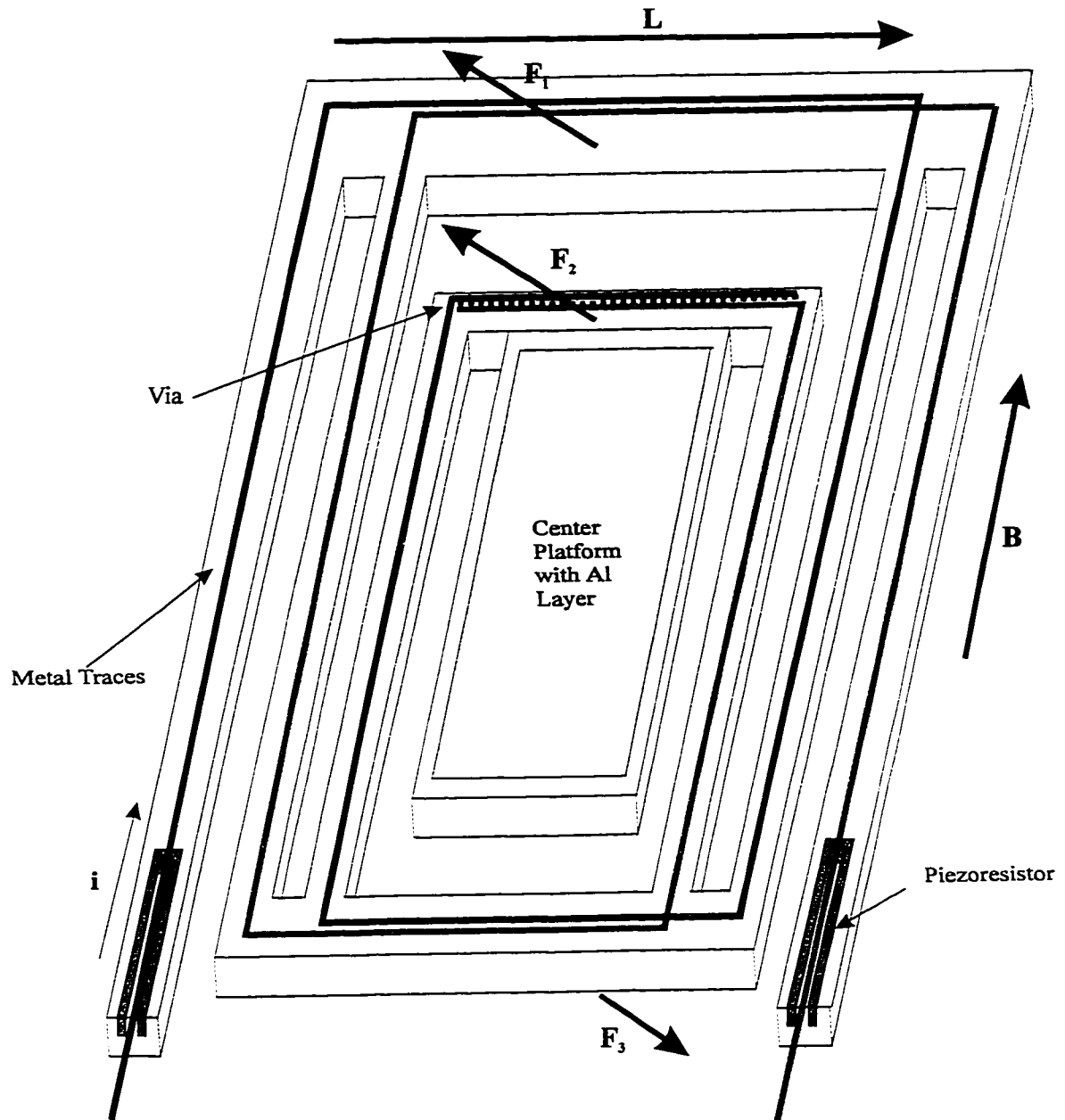


Figure 3.3 Actuation of triple cantilever-in-cantilever type 1.

after packaging and bonding the chips. That is, XeF_2 does not etch the aluminum bonding wires or ceramic package, but undercuts the edges of the chip. Handling of the chip after etching increases the likelihood of damaging the devices. A total of 15 one-minute pulses were required to completely undercut the devices to free them from the

substrate. The amount of etch depth and undercutting achieved after release was each approximately 100 μm , estimated by the amount of undercut and the number of etch pulses used.

3.3 EXPERIMENT LAYOUT AND PROCEDURE

The experimental layout for the investigation of pressure variations on the dynamic behaviour of CIC microstructures is shown in Figure 3.4a. A chip containing five variations of the cantilever-in-cantilever devices was packaged on a 40 pin Dual In-line Package (DIP). This DIP was placed into a Zero Insertion Force (ZIF) socket that was mounted inside an aluminum box. Aluminum was used as it is both non-magnetic and sufficiently strong for both vacuum and high pressure experiments. The top and bottom of the box are made from clear plexi-glass 4 mm thick. Holes were drilled in the bottom plate to allow the ZIF socket's pins to protrude outside of the pressure vessel. These were later sealed with Torr Seal[®], a high quality epoxy resin designed exclusively for use in vacuum environments. A rubber o-ring provided the seal to the top, which, in turn, was fastened down with several equally spaced screws.

External actuating magnets were mounted in countersunk holes on the sides of the box. These magnets would only actuate devices oriented appropriately within the chamber for generation of the required Lorentz force. Not all of the CIC's characterized were oriented properly with respect to this magnetic field and an alternative arrangement was devised by positioning a horseshoe magnet on top of the pressure vessel as portrayed in Figure 3.4b. The magnetic field interacting with the current in the CIC is approximately 220 G for the initial configuration, (a), and 750 G for the top-mounted

magnet, (b). These fields were measured with a model 511 Gaussmeter (LDJ Electronics Inc.) after probe calibration.

Care was taken throughout the experiment to maintain a constant magnetic field in the vicinity of the devices. This was achieved by first orienting the magnet so as to produce maximum response from each device under atmospheric conditions. Then, once this position was found, the magnet was not disturbed throughout the data taking.

Measurements were conducted with this setup for pressures ranging from 100 Torr to 1450 Torr as measured by a Bourdon pressure gauge with a resolution of 10 Torr. At the beginning of the experiment the pressure gauge was calibrated to the atmospheric pressure. The chamber was unable to maintain constant pressure for values outside this range. Pressures below 100 Torr were obtained with a vacuum system consisting of a bell jar and a mechanical pump. The aluminum chamber, without its original plumbing, was placed inside the bell jar. An illustration of this can be seen in Figure 3.5. The magnetic field source was kept in the same configuration as before. Data was taken from 15 Torr up to 700 Torr in the bell jar system to facilitate the merger of data taken from the two systems.

The signal conditioning circuitry used to measure the piezoresistor response is shown in Figure 3.6. A constant current of $500 \mu\text{A}_{\text{dc}}$ was generated by a Wilson current mirror and sent through both piezoresistors in series. The purpose of a current mirror is to provide constant current independent of the resistive load. The voltage across the piezoresistors was amplified by a two-stage AC-amplifier circuit. The amplifier circuit has a gain of 94, a cut-off frequency of 29.8 kHz, and a nominally flat gain that decreased by only 2.8% over the frequency range 1 kHz to 15 kHz. The two-stage design along

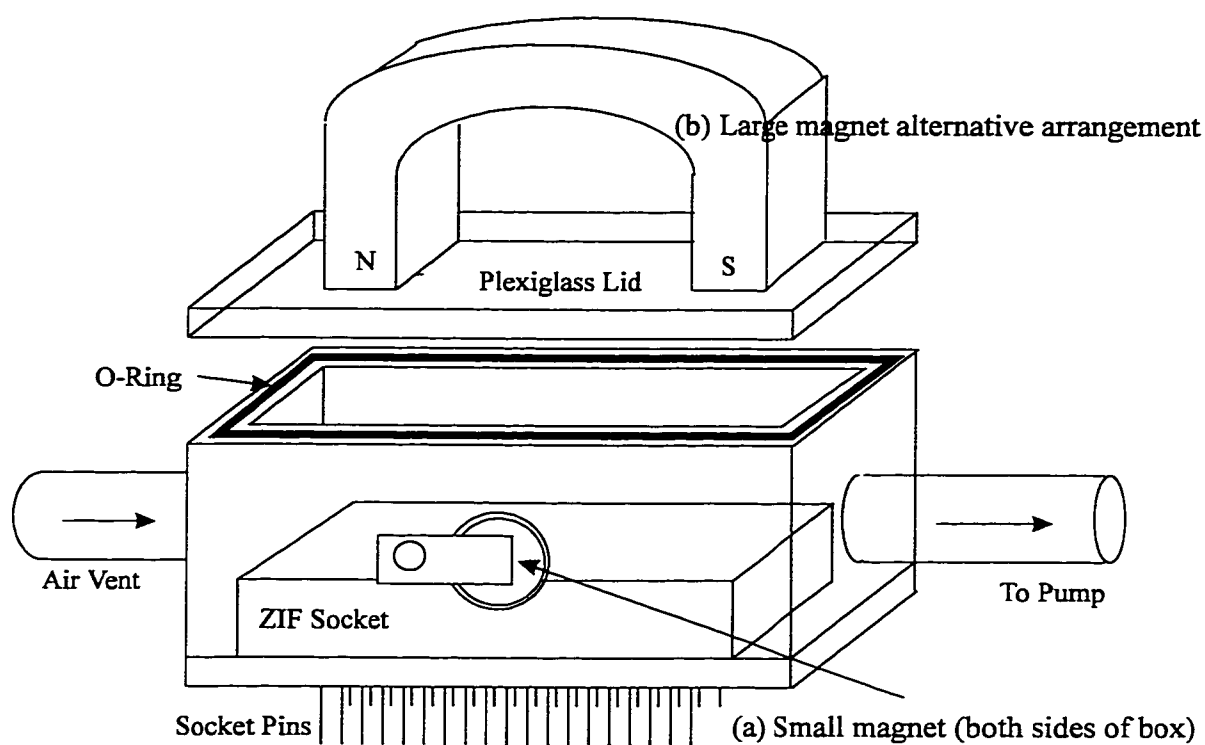


Figure 3.4 Experiment layout and magnet arrangement.

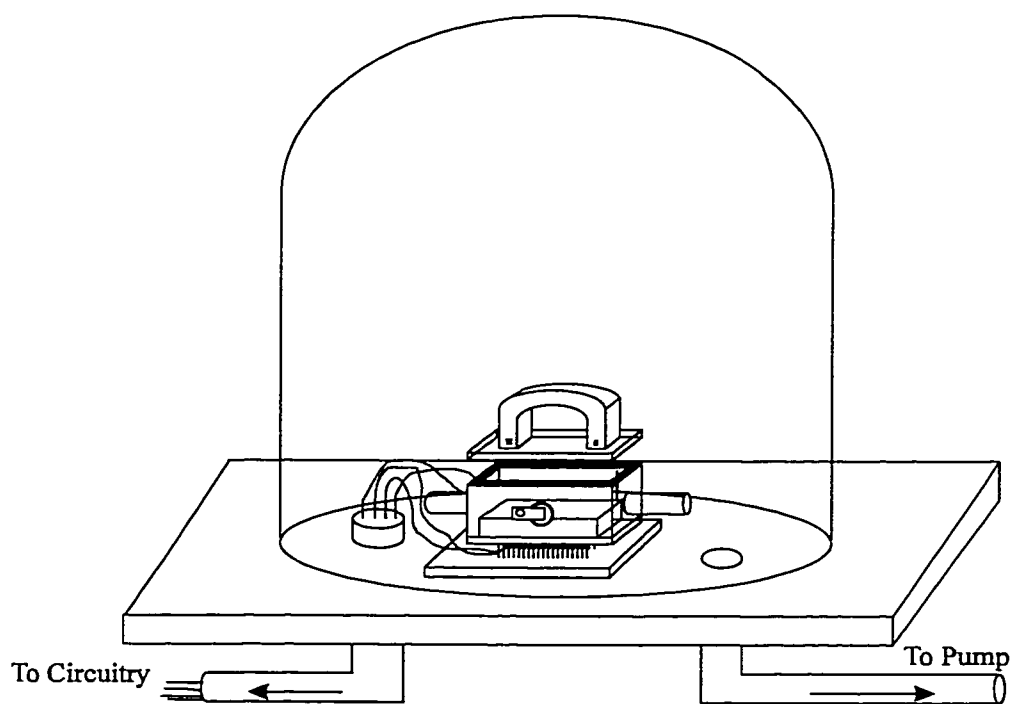


Figure 3.5 Bell jar experimental setup.

with the several capacitors shown in the figure enabled this flat-gain response and filtered out the DC components of the signal. A $270\ \Omega$ resistor was added in series with the actuating current loop on the CIC to add a temperature-independent resistive load to the signal generator. This extra resistance was necessary to stabilize the current applied to the CIC, as the AI on the CIC is typically $10\text{--}30\ \Omega$ and is strongly temperature dependent.

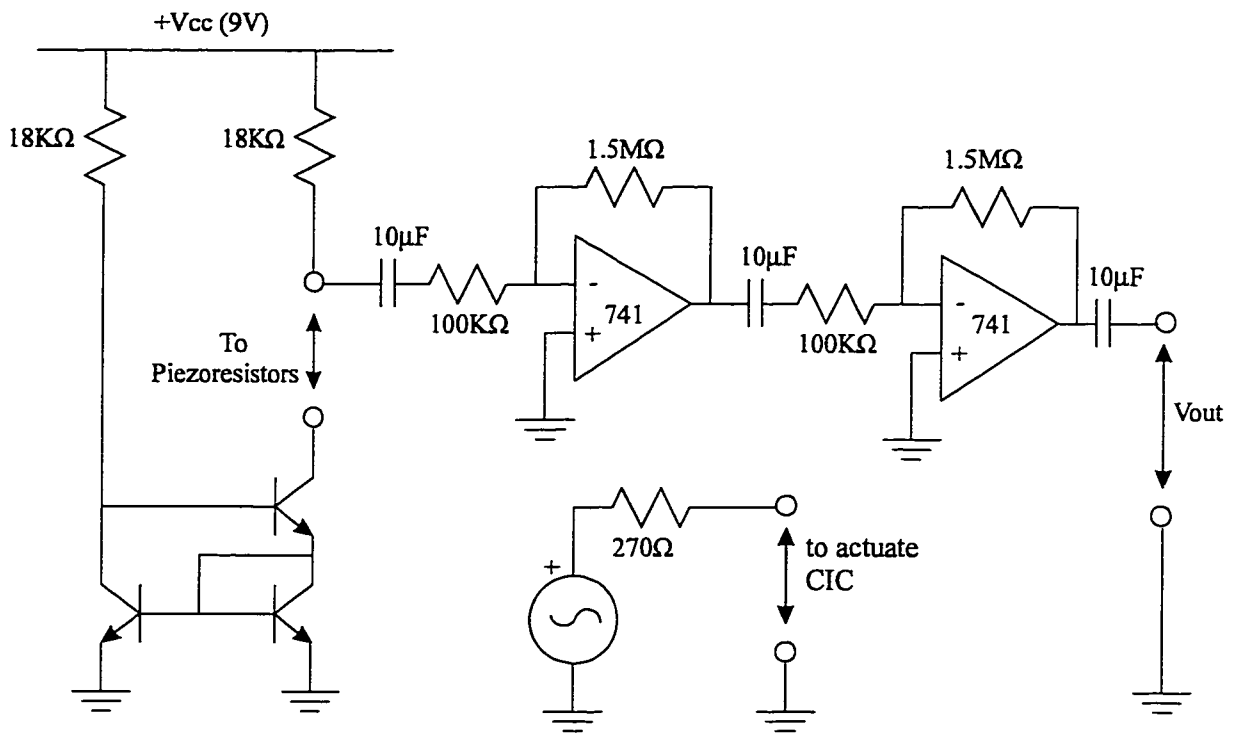


Figure 3.6 Signal conditioning circuitry.

An extensive number of data points were taken with the aid of an automated data acquisition system designed and produced in our laboratory. Figure 3.7 illustrates the data acquisition setup. The waveform generator and digital multimeter are controlled through the computer by the source code, and are connected to the signal conditioning circuit. The signal conditioning circuit (Figure 3.6) is connected to the device under test

via the ZIF socket pins protruding out of the pressure chamber. The source code was written in Microsoft® QuickBASIC 4.50®, an example of which is provided in Appendix A. This software provided computer control and programming of both the signal generator and digital multimeter via the computer's communication ports. In addition, smart algorithms were developed that provided feedback and preliminary analysis of the results prior to file writing. For example, the program, instead of simply sweeping the frequency domain and printing responses, could find resonant frequencies and decrease

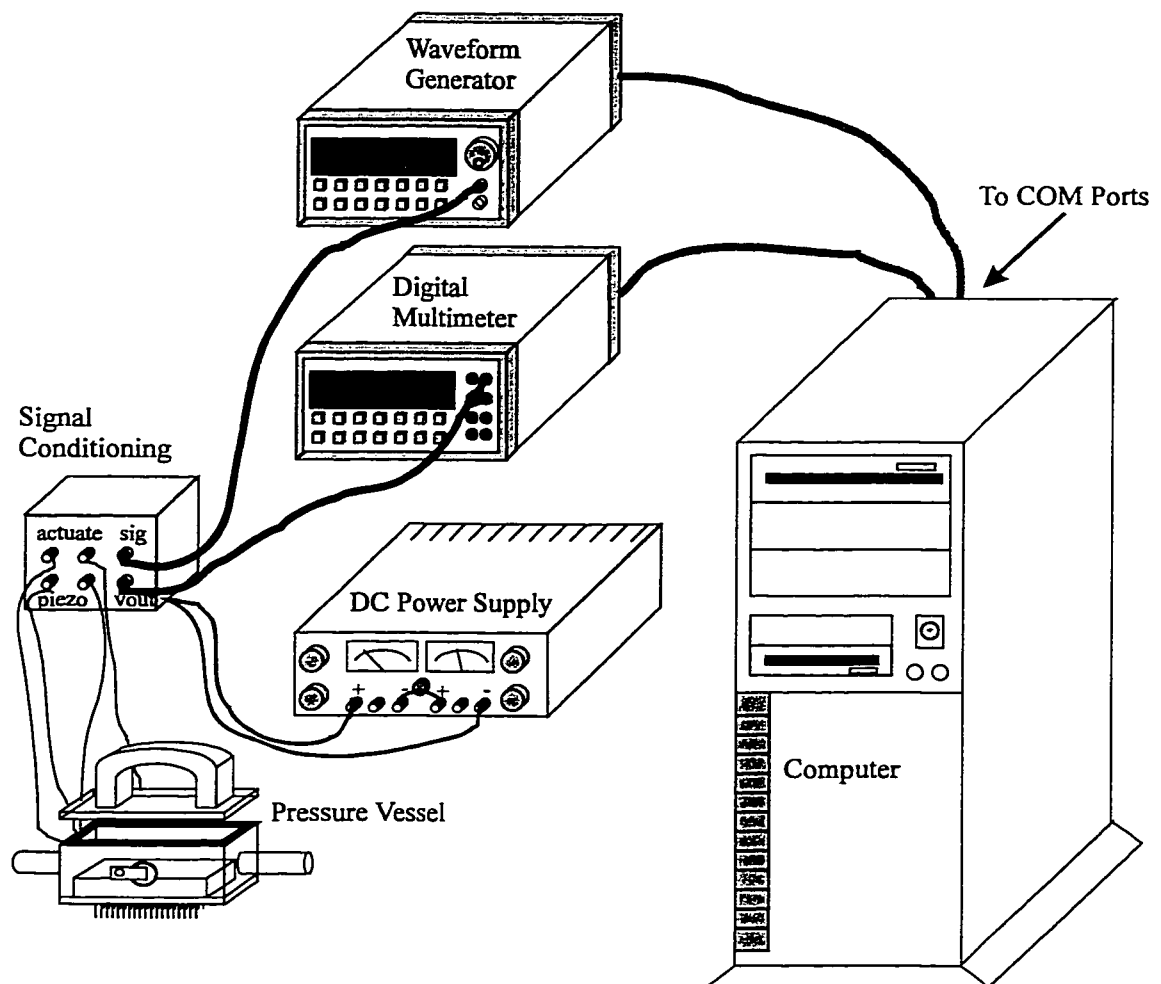


Figure 3.7 Data acquisition setup.

the frequency step size in those regions to yield more detailed data. A total of four program modules were created. The first module, shown in Appendix A, produced device response data as a function of frequency. The second module was designed to find resonant frequencies. Module three utilized user-entered values for pressure, found the corresponding resonant response, and displayed all relative information. The last module was used to find actuating current while maintaining constant piezoresistor response as the pressure varied.

Multiple samples at each frequency were taken to improve the signal quality and reduce noise effects. That is, at each data point the digital multimeter was triggered to sample the signal from 2 to 10 times. These values were input to the computer and the average signal calculated before writing to file. The number of samples taken was dependent upon the frequency step size. A frequency step size of 1 Hz was sampled twice, while any frequency step sizes greater than 50 Hz were sampled 10 times. Frequency step sizes between these values were assigned a sampling number between 2 and 10. A delay of approximately 1 second took place between a change in frequency and the computerized sampling of the device response.

3.4 RESULTS AND ANALYSIS

Using the experimental setup described, experimental results were obtained as pressures were varied from 0.1 to 1450 Torr. Stable results were seen for pressures of 15 Torr and higher. Below 15 Torr, hysteresis behaviour was observed, which is presented in Chapter 4.

All type 1 and type 2 devices were tested first to determine at which frequency each device produces a maximum piezoresistive response. These tests were carried out at 700 Torr, the atmospheric pressure in Edmonton, by applying a sine wave AC signal of 10 mA_{pp} to actuate the device. Frequencies from 1 kHz to 25 kHz were applied and the piezoresistor response was measured using the automated data acquisition system as described in Section 3.3. Figure 3.8 and Figure 3.9 show the results that were obtained for the single (types 1 and 2) and double (types 1 and 2) cantilever-in-cantilevers, respectively, and Figure 3.10 depicts the results for the triple CIC type 1. All plots are straight line fits between data points. The smoothness of the curves is due to the small frequency step of 20 Hz used during data taking.

There are two resonant peaks shown in Figure 3.8. The smaller peak is due to a second resonant mode. Figure 3.9 does not show any additional resonant peaks within

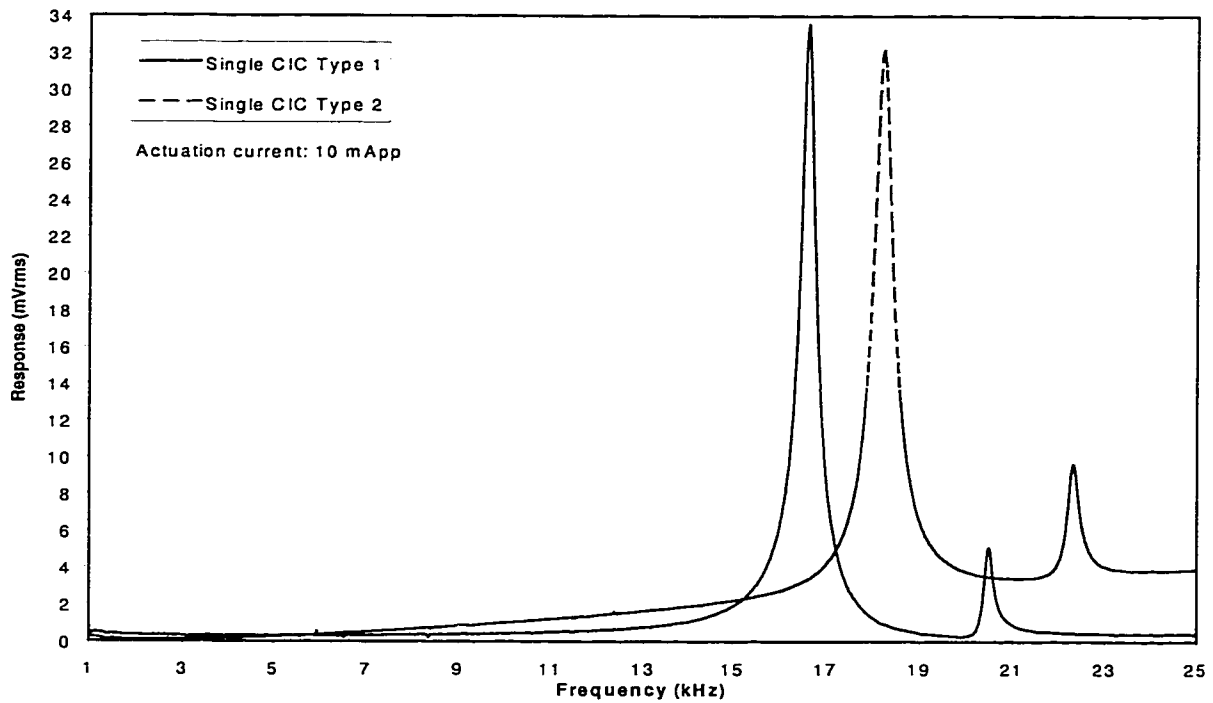


Figure 3.8 Frequency response for single CIC's at atmospheric pressure and constant actuating current.

the frequency range tested; however, a noticeable drop in piezoresistor response can be seen around 11 kHz. The cause of this response is not fully understood. Changing the polarity of the magnetic field eliminates this drop in response. In Figure 3.10, there are an additional three resonant peaks present for the triple CIC within the frequency range tested. For all type 2 devices the resonant peaks occur at higher frequencies than for the corresponding type 1 devices. This behaviour is predicted in Chapter 4.

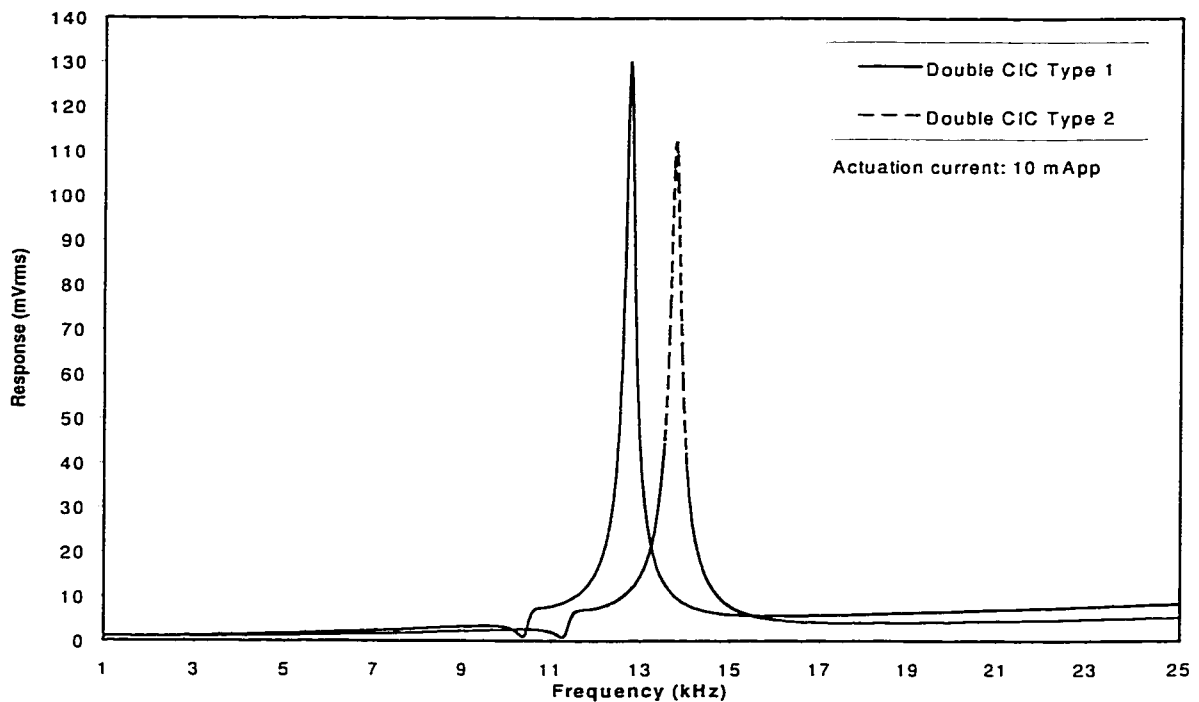


Figure 3.9 Frequency response for double CIC's at atmospheric pressure and constant actuating current.

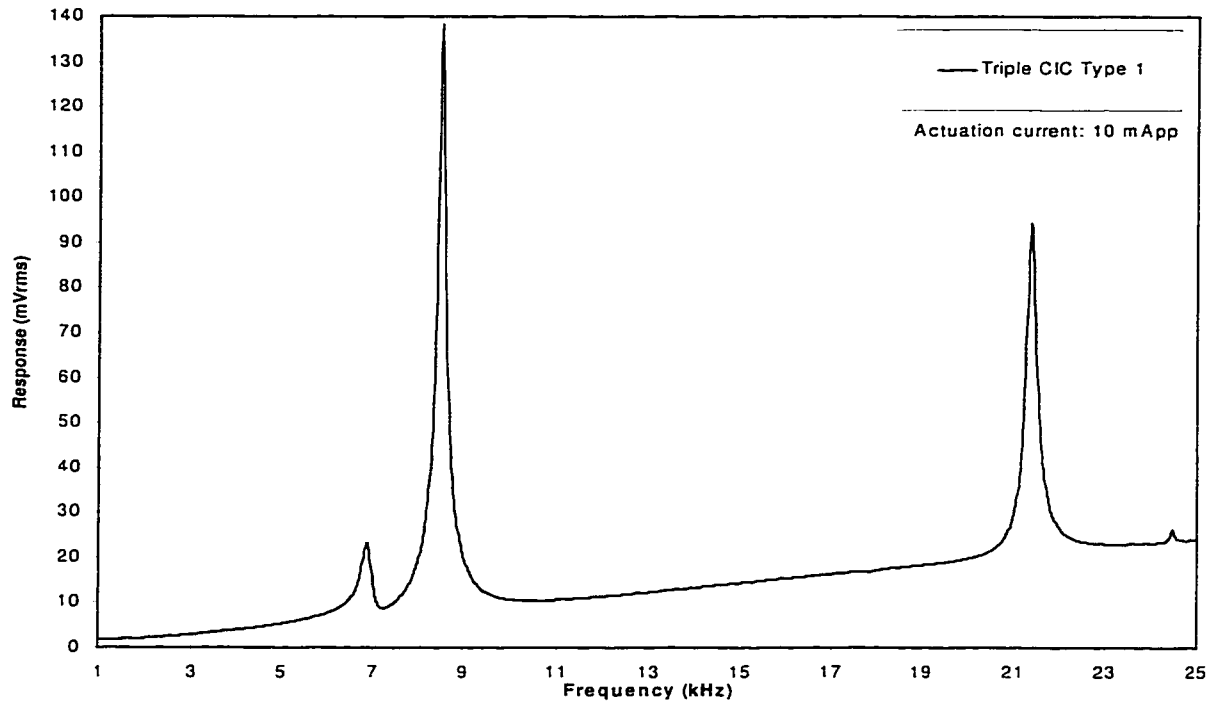


Figure 3.10 Frequency response for triple CIC at atmospheric pressure and constant actuating current.

3.4.1 Resonant Frequency

The resonant frequency, the frequency at which the largest response was observed, was monitored as the pressure was altered. Figures 3.11 to 3.13 each show the relationship between pressure and maximum response resonant frequency for single, double, and triple CIC's, respectively. It is seen that the behaviour of type 1 and type 2 devices is quite similar, except for an approximately constant shift in resonant frequency over the entire pressure range. Each plot was least-squares fitted using Microsoft® Excel97® spreadsheet software. The resulting curves showed at least a 99% correlation between experiment points and the curve. The best fit equations shown are all second degree polynomials, where f represents the frequency in kHz, and p the pressure in Torr.

The effects of temperature changes on the resonant frequency of these CIC devices was investigated [38]. Double and triple type 1 devices were subjected to a 60°C temperature increase resulting in shifts in resonant frequency of 20 and 35 Hz, respectively. A resonant frequency shift of 20 Hz for a double CIC type 1 and 35 Hz for a triple CIC type 1 is equivalent to a pressure change of 345 and 269 Torr, respectively. Therefore, temperature effects are significant and must be compensated for during experiments performed at changing temperatures. All experiments performed in this thesis were done at constant room temperature.

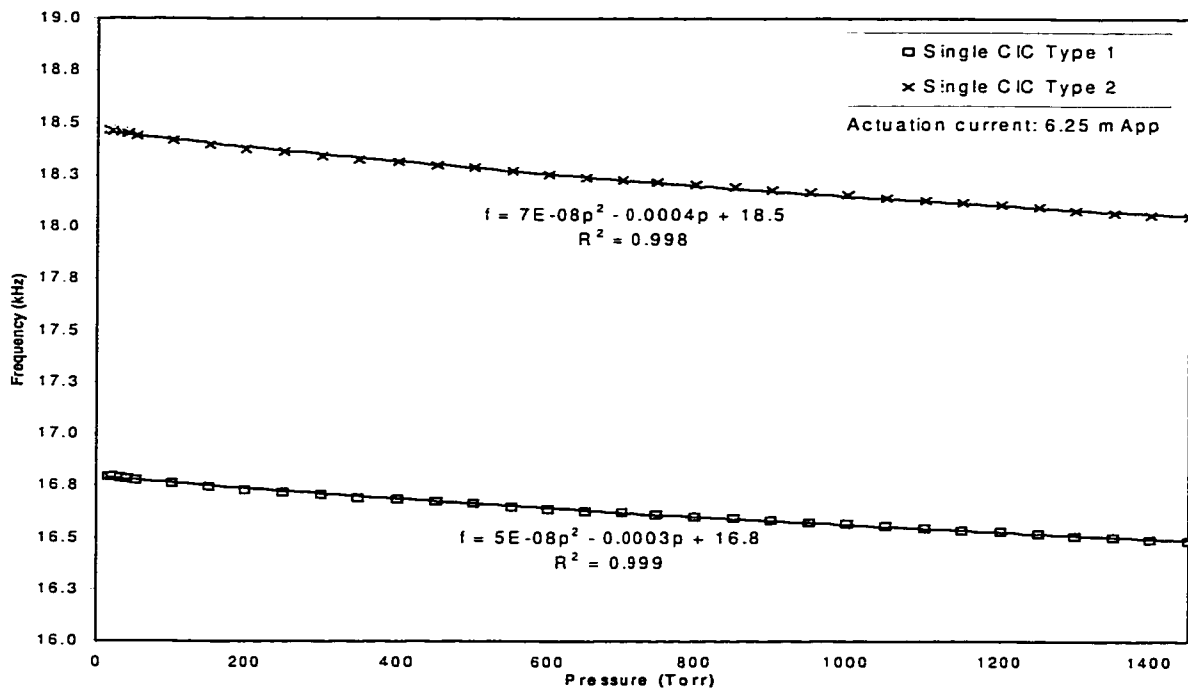


Figure 3.11 Frequency at which largest piezoresistive response is observed versus pressure for single CIC's at constant actuating current.

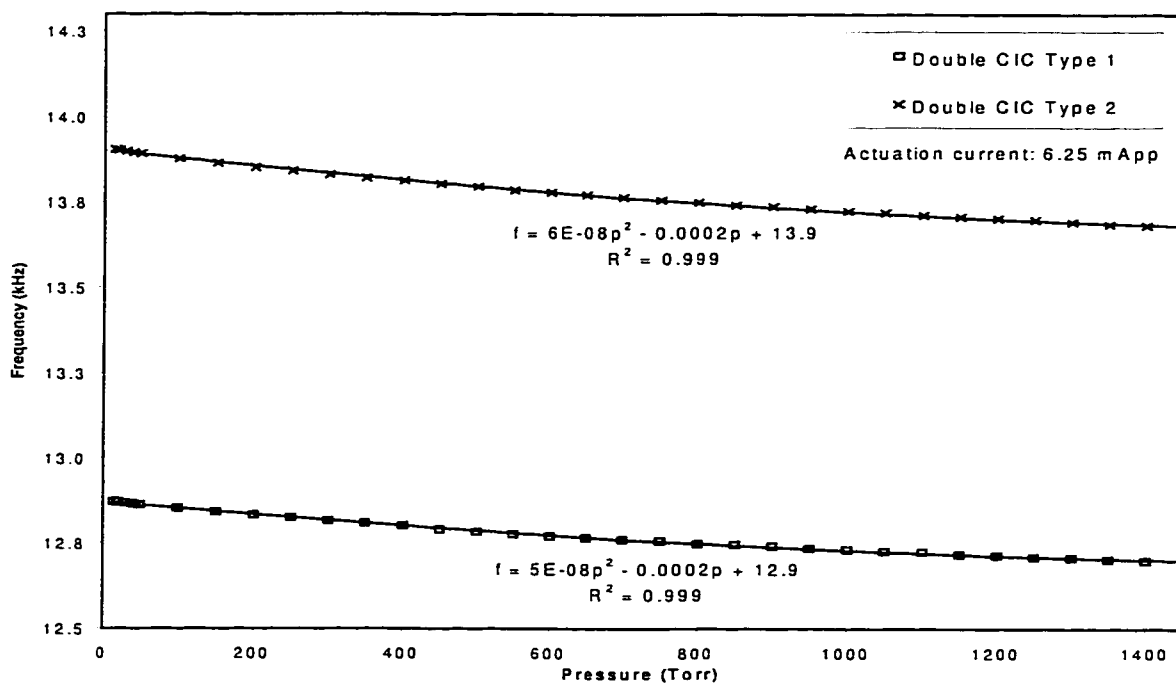


Figure 3.12 Frequency at which largest piezoresistive response is observed versus pressure for double CIC's at constant actuating current.

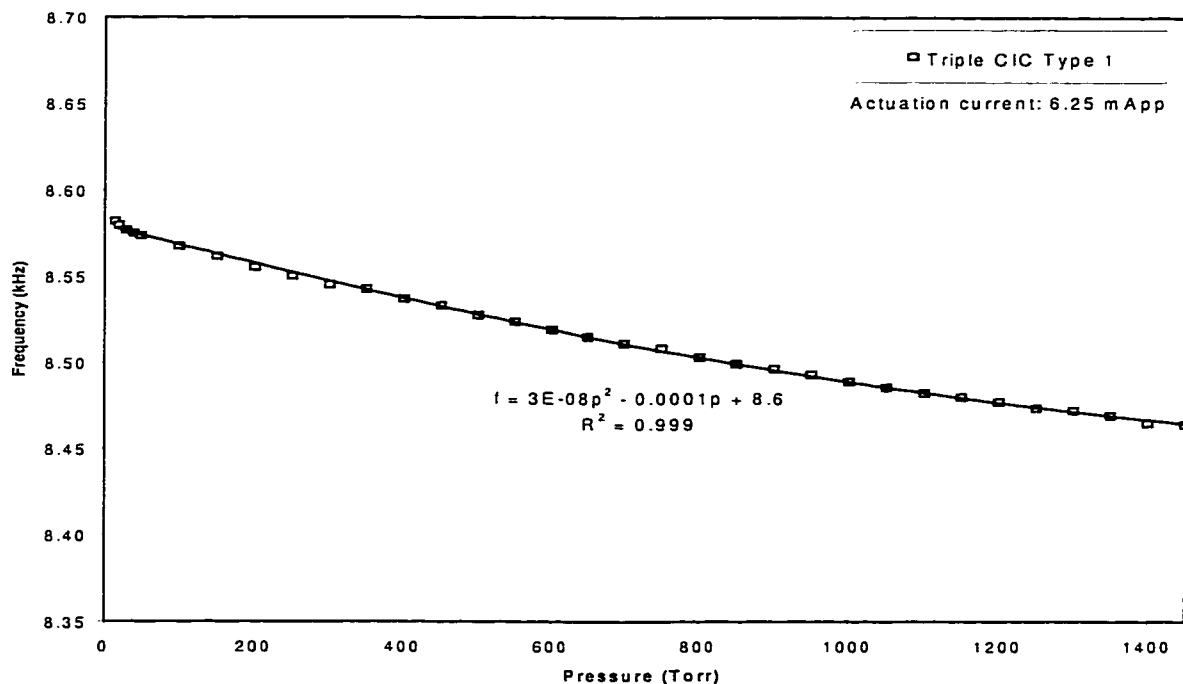


Figure 3.13 Frequency at which largest piezoresistive response is observed versus pressure for triple CIC at constant actuating current.

3.4.2 Quality Factor

The behaviour of a damped, driven resonating structure, such as the cantilever-in-cantilever, can be characterized by looking at the height and width of a resonance peak. This characterization is often specified by the Quality factor or Q -value which is defined as:

$$Q = \frac{\omega_o}{\Delta\omega} \quad (3.4.1)$$

where ω_o is the frequency of the resonance peak, and $\Delta\omega$ is the width of the peak where the square of the amplitude has half its maximum value [39]. As damping increases due to increased ambient pressure, the Q -value is expected to diminish and the resonance curve is flattened out. Figure 3.14 shows the relative response for a single CIC type 1 at various pressures. The resonant frequency decrease with increasing pressure, as shown in Figure 3.11, is clearly evident. The “flattening” of the resonance peak as pressure increases is also seen. Figures 3.15 to 3.18 are illustrations of the relative piezoresistive response versus frequency for various pressures.

The above measurements were carried out for all devices and the Q -values were calculated. A graph of Q versus pressure is presented in Figure 3.19. There is a general trend towards a decrease in Q as pressure increases. These results clearly demonstrate that air pressure has a significant effect on the resonance properties of cantilever-in-cantilever microstructures.

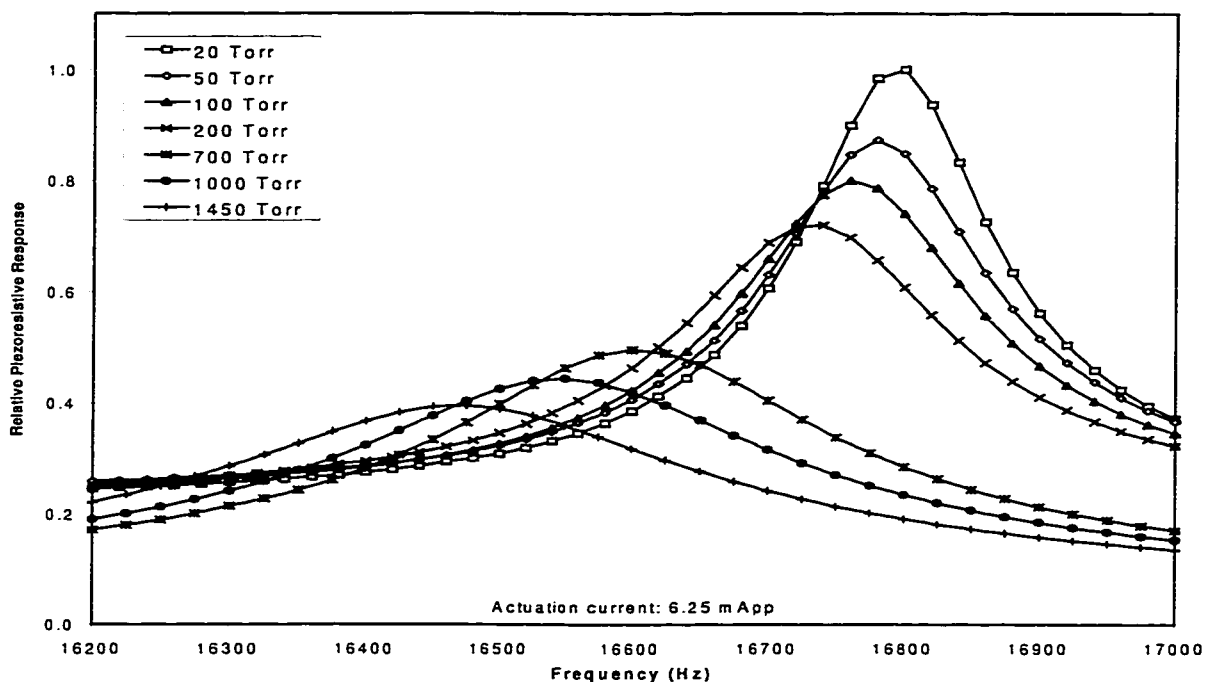


Figure 3.14 Relative piezoresistive response versus frequency for single CIC type 1 at constant actuating current.

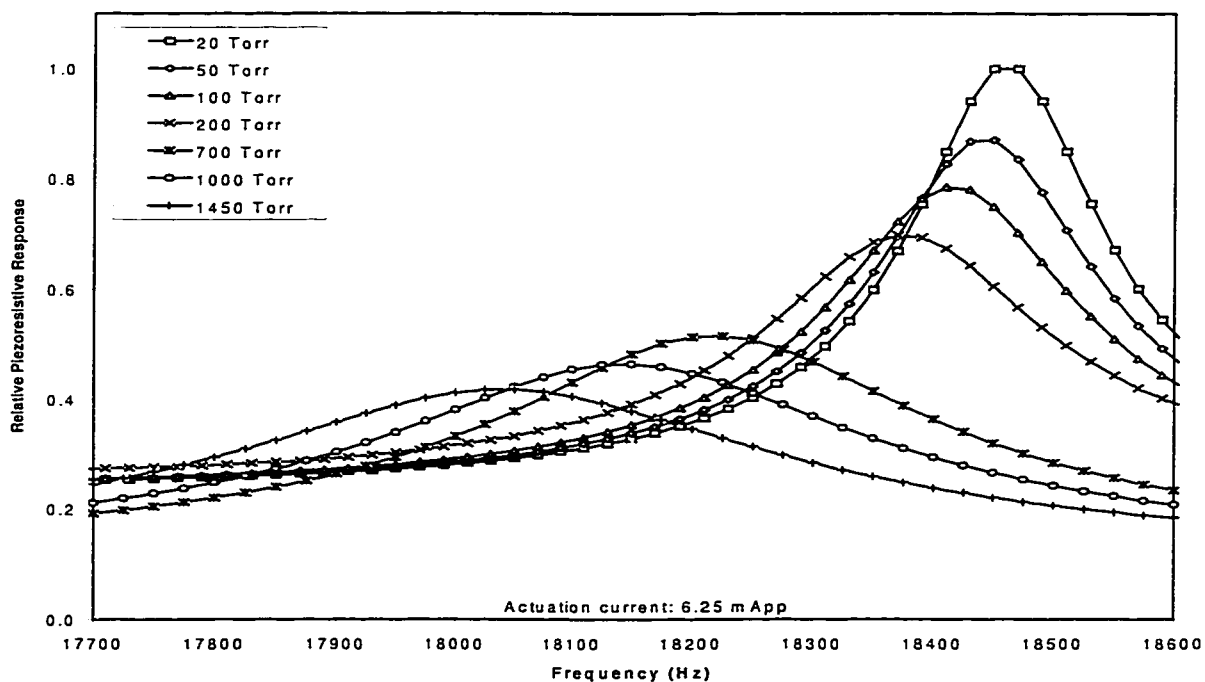


Figure 3.15 Relative piezoresistive response versus frequency for single CIC type 2 at constant actuating current.

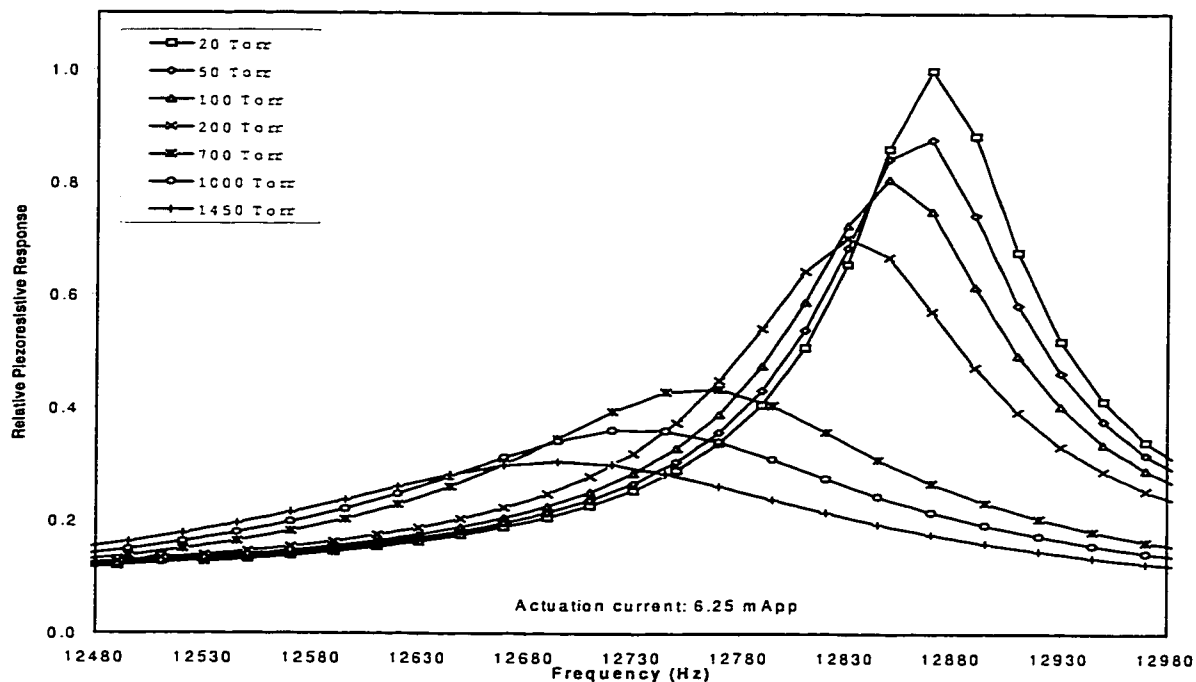


Figure 3.16 Relative piezoresistive response versus frequency for double CIC type 1 at constant actuating current.

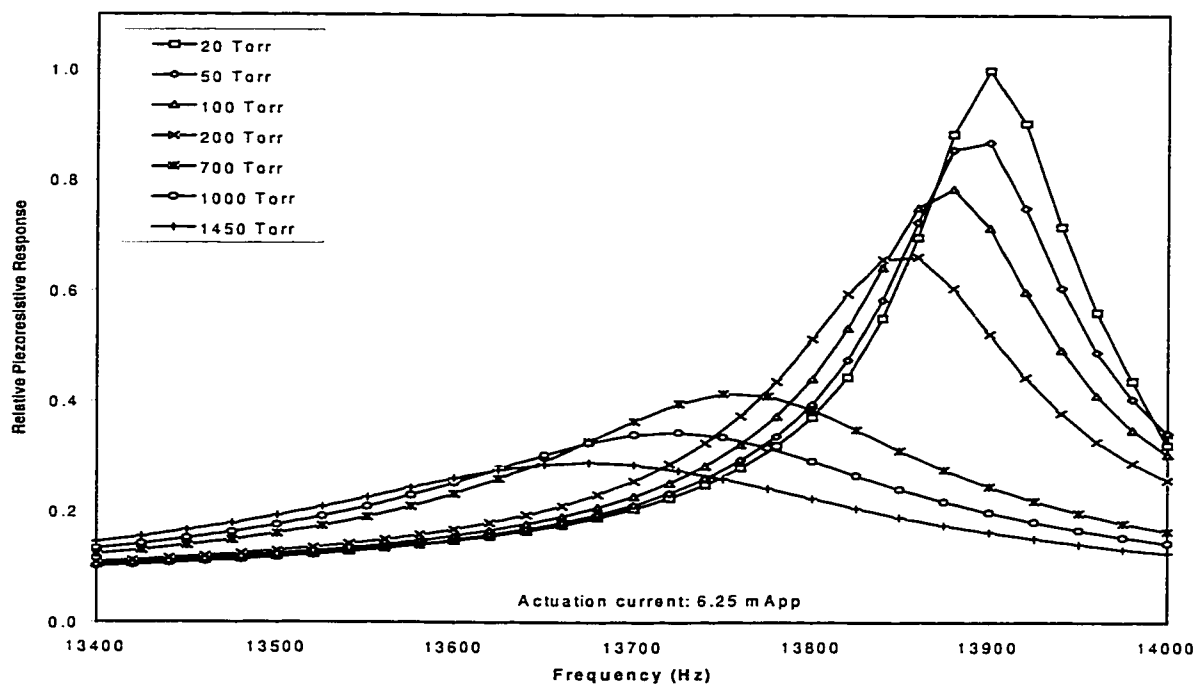


Figure 3.17 Relative piezoresistive response versus frequency for double CIC type 2 at constant actuating current.

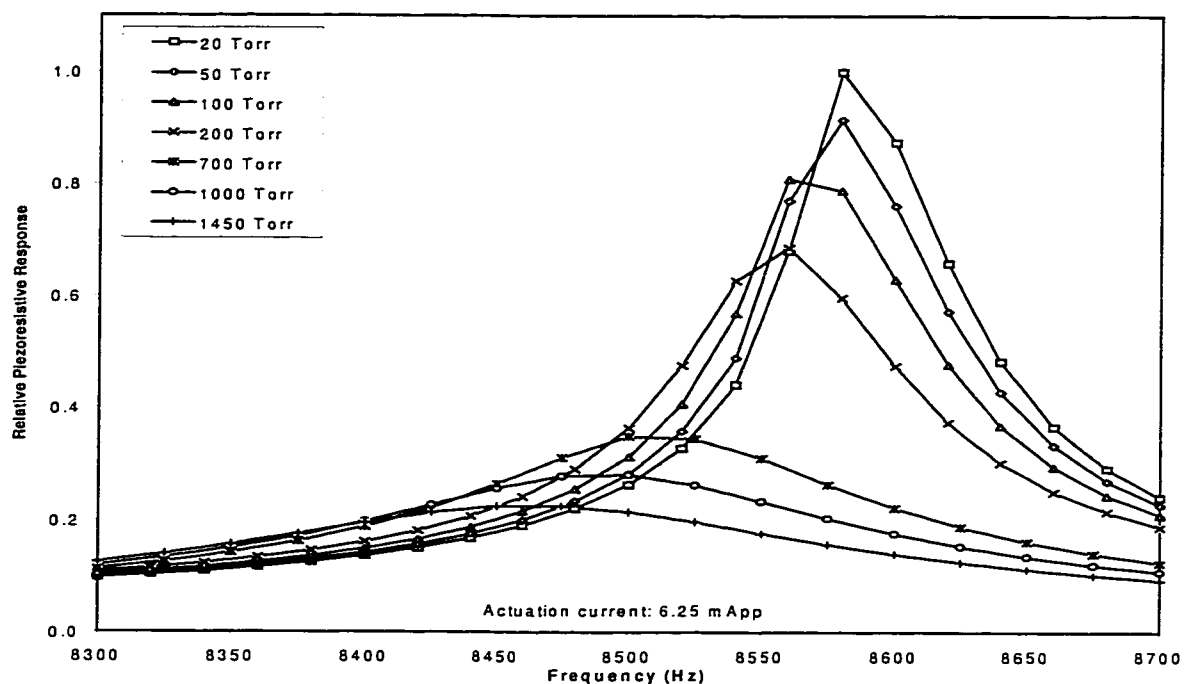


Figure 3.18 Relative piezoresistive response versus frequency for triple CIC type 1 at constant actuating current.

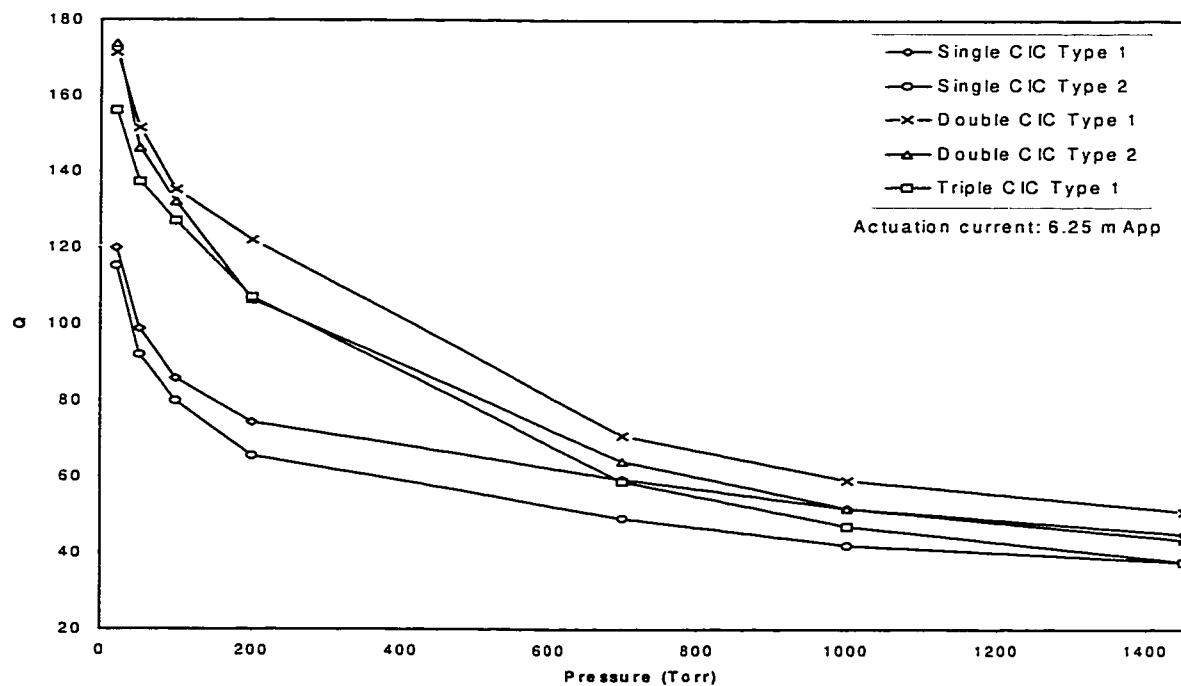


Figure 3.19 Q versus pressure at constant actuating current.

3.4.3 Actuating Current

Another method for pressure detection that may be used is to monitor the actuating current required to maintain constant piezoresistor response at resonance, that is, cantilever deflection, as the pressure is varied. In effect, what is measured is the force required to maintain constant CIC deflection as the damping changes. All of the devices were tested while maintaining a piezoresistive response of $60 \text{ mV}_{\text{rms}}$. The results obtained are shown in Figure 3.20. A fourth degree polynomial was least squares fitted to the data. Between 300 and 1450 Torr the required actuating current increases approximately linearly with pressure. Note that the type 2 devices require slightly more current than their respective type 1 structures. This is most likely the result of a conservation of energy. The kinetic energy of each device is the product of its mass multiplied by its velocity squared. Type 2 devices, while having less mass than their respective type 1 device, have higher resonant frequencies and thus higher velocities than their corresponding type 1 device. Since the actuating current is directly proportional to the force applied, and the devices are moving the same distance, the actuating current is directly proportional to the kinetic energy. Therefore, since type 2 devices require more actuating current than their respective type 1 device, they have more kinetic energy. Hence, the difference in velocity squared between type 1 and type 2 devices is greater than their difference in mass.

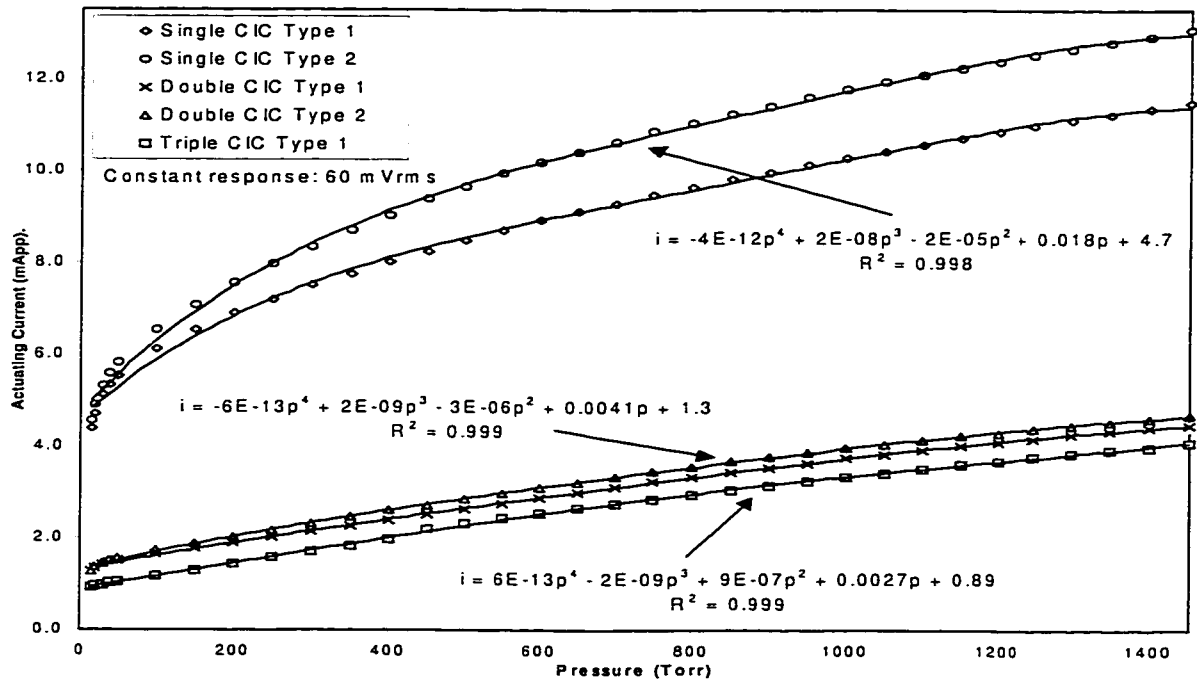


Figure 3.20 Actuation current versus pressure for constant piezoresistive response at resonance.

3.4.4 Piezoresistor Response

A further parameter that may be investigated for pressure measurements is the piezoresistor response at resonance for constant actuating current. A plot of this response versus pressure for all cantilever-in-cantilever devices is shown in Figure 3.21. Fourth order least squares curve fitting was implemented. An actuating current of 6.25 mA_{pp} was applied. As shown in Figure 3.21, the order of device response to pressure is: triple CIC type 1, double type 1, double type 2, single type 1, and single type 2, where the order ranges from highest piezoresistive response to lowest piezoresistive response.

As the pressure decreases below 15 Torr the nature of response for each device changes. The devices are entering a region of non-linearity where hysteresis effects occur. Chapter 4 addresses these issues and also deals with device modeling.

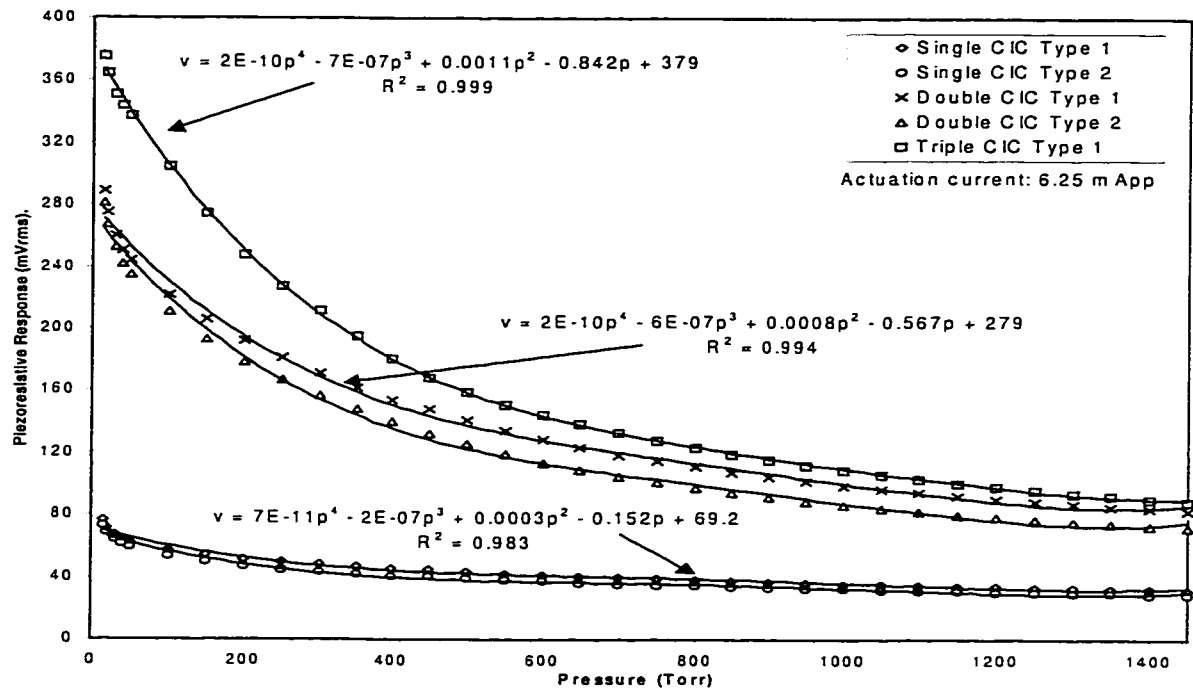


Figure 3.21 Piezoresistor response at resonance versus pressure at constant actuating current.

Chapter 4

SENSOR MODELING AND ANALYSIS**4.1 INTRODUCTION**

Developing device concepts on the micron scale is strong motivation to truly understand the fundamental principles involved. At these small scales, macroscopic intuition often fails, and a closer look at the fundamentals of device operation is required. At microscopic dimensions, the mechanical behaviour of devices is sensitive to both the surface properties of materials and the dynamics of the medium in which it actuates. In conventional mechanical systems, inertial forces dominate: once a rotor starts spinning, it has a tendency to keep spinning. But that is not the case for micromachines. As size decreases, inertial forces weaken while interfacial forces strengthen and finally dominate. Viscous medium dynamics also begin to play a significant role in micro-structure behaviour [40].

Analysis and modeling of the dynamic behaviour of cantilever-in-cantilever (CIC) devices has been done previously in our laboratory [18,19,42-45]. Further investigation of these dynamic properties has yielded a model to explain the effect of air pressure damping on oscillating microstructures. This chapter will discuss this model and compare theoretically predicted results with experimental measurements. Following this is a brief description of piezoresistivity. Lastly, non-linear measurement results involving hysteresis effects for pressures below 15 Torr and down to 0.1 Torr are discussed and analyzed.

4.2 RESONANT RESPONSE ANALYSIS

This section contains a comparison between the experimentally measured cantilever response versus frequency, at atmospheric pressure, as shown in Figures 3.8 to 3.10, and the expected theoretical resonant response curve. In other words, we wish to determine how well the measured resonant response of a cantilever device “fits” the classical resonating structure model.

The equation governing the deflection of our damped, driven harmonic oscillator system can be expressed as:

$$\rho \frac{\partial^2 z}{\partial t^2} + \rho_1 \frac{\partial z}{\partial t} + K_1(z)z = G(x, y, t) \quad (4.2.1)$$

where z is the amount of device deflection out of the plane of the chip and is a function of x, y , and t , and $K_1(z)$ is the device stiffness. Equation (4.2.1) and the exact form of $K_1(z)$ are classical equations for linear elasticity found in [46]. The area density (mass/area) is denoted by ρ , and the damping term by ρ_1 . $G(x, y, t)$ defines the force per unit area or “load” on the system. The frequency response of a CIC device consists of an infinite number of resonant modes, so to find a solution of Equation (4.2.1), we seek a deflection of the form:

$$z = \sum_{i=1}^{\infty} c_i(t) \varphi_i(x, y) \quad (4.2.2)$$

where φ_i are the eigenfunctions of $K_1(z)$ with eigenvalues λ_i . The term $c_i(t)$ is a function of t , attributable to each mode of oscillation. These eigenfunctions and eigenvalues can only be computed numerically, and solutions of the first two modes for a triple CIC type 1 without piezoresistors are shown in [42].

The current applied to actuate the device is of the form

$$i(t) = I_o \sin(\omega t) \quad (4.2.3)$$

and the Lorentz force acts on the conductor paths as described by Equation (3.1.1) and shown in Figure 3.3. This Lorentz force on each of the conductor paths of length L is equal to

$$G(x, y, t) = \frac{I_o \sin(\omega t) LB}{A} \quad (4.2.4)$$

where A is the conductor area, B the magnetic field, and L the conductor length along which the current flows. Solving Equation (4.2.1) for the deflection z is not a trivial matter. If a theoretical determination of deflection is to be made then a specialized solution technique is required.

For complex vibration systems the easiest method of confirming the shape of the resonance peak, known as modal resonance testing, is called the “single-degree-of-freedom curve fit” approach [47]. This approach sections off the frequency response into frequency ranges around each successive response peak. For our purposes only the largest response peak will be sectioned off and investigated. The peak is then analyzed under the assumption that its frequency response is the result of a single degree-of-freedom system. That is, in the vicinity of the response peak only a single mode of vibration dominates, thus removing the summation in Equation 4.2.2 and replacing the subscript i with 1. This approach also assumes that the resonance peaks are sufficiently separated to easily distinguish between them.

To begin this analysis we have to look at the damping ratio. The damping ratio, ξ , affects the shape of the response curve near resonance, at frequency ω_o , and here is assumed to be the modal damping ratio. The modal damping ratio is a quantity that

pertains only to the single mode assumed to be present at the resonant frequency of interest. The damping ratio is related to the damping term by

$$\xi = \frac{\rho_1}{2\omega_o \rho} \quad (4.2.5)$$

Given the experimental results and using a method similar to that for finding the Q-value, known as the bandwidth method, a value for the damping ratio can be easily determined from the following equation

$$\xi = \frac{f_2 - f_1}{2f_o} = \frac{f_2 - f_1}{f_2 + f_1} \quad (4.2.6)$$

where f_1 and f_2 are the frequencies around the maximum response frequency, f_o equal to 0.707 times the maximum response. These two points, f_1 and f_2 , are also called the 3-dB down points and correspond to the half-power points of the response peak.

The next step involves taking, as a function of frequency, a generalized equation representing cantilever deflection with damping and applying to it measured values of these quantities. A best fit curve can then be found to match the experimental results with this function. The generalized equation for resonance with damping that we will use is

$$z = \frac{\beta}{\sqrt{(f_o^2 - f^2)^2 + \gamma^2 f^2}} \quad (4.2.7)$$

where β is a constant, f is the frequency of actuation, f_o is the resonant frequency, and γ is a damping term linearly related to the damping ratio [48]. That is, $\gamma = \alpha\xi$ where α is a constant. The best fit is determined by the method of least squares fitting that assumes values for β and γ so as to minimize the error function

$$Error = \frac{\sqrt{\sum_{i=1}^N [z(f_i) - X(f_i)]^2}}{N} \quad (4.2.8)$$

with N , the number of experimental data points, and $X(f_i)$ the experimental response at frequency f_i . Table 4.1 contains the damping ratio values for all the CIC devices investigated in Chapter 3, as well as, the corresponding best fit values for β and γ . These values represent the lowest error determined for the displayed level of precision.

Table 4.1 Damping ratio, constant, and damping term for resonant response curve fit at 700 Torr.

Device	Damping Ratio, ξ (%)	Constant, β	Damping Term, γ
Single type 1	0.81 %	125.0	0.215
Single type 2	0.95 %	171.0	0.275
Double type 1	0.71 %	275.0	0.160
Double type 2	0.77 %	302.0	0.190
Triple type 1	0.88 %	167.4	0.142

Figure 4.1 shows the experimentally obtained data points and the best fit curve for a triple CIC type 1 structure. Similar plots for the other CIC devices are shown in Figure 4.2 (double type 1 and 2) and Figure 4.3 (single type 1 and 2).

As seen from the figures there is a close fit between the data points and the fitted response. Hence, the CIC structures fabricated and designed for this project are exhibiting good harmonic oscillator behaviour. However, as seen in Figure 4.2 and Figure 4.3, some of the data points do not match completely with the best fit curve. It

might seem that a better fit might be possible for these figures by increasing the number of significant digits for β and γ . However, increasing the number of significant digits for β and γ is not practical given that the precision in response is $\pm 1 \text{ mV}_{\text{rms}}$ and the best fit curves are already within this error region.

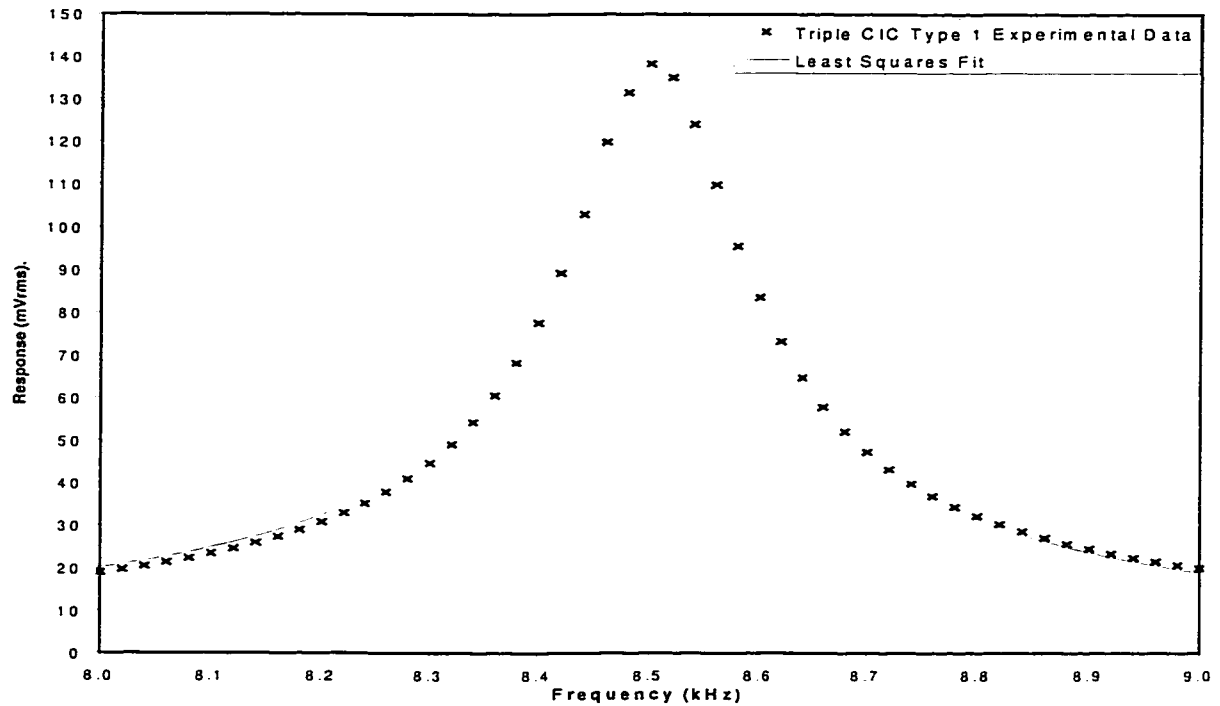


Figure 4.1 Least squares fitting of response of triple CIC type 1 at constant actuating current versus frequency.

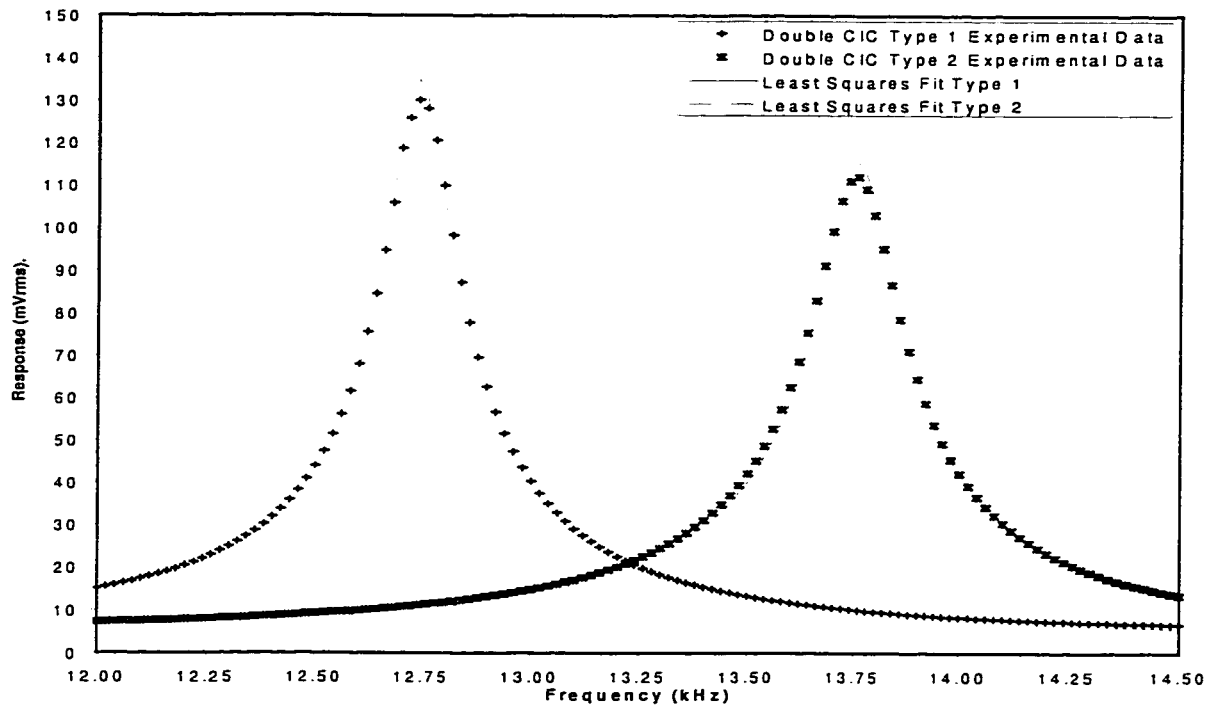


Figure 4.2 Least squares fitting of response of double CIC type 1 and 2 at constant actuating current versus frequency.

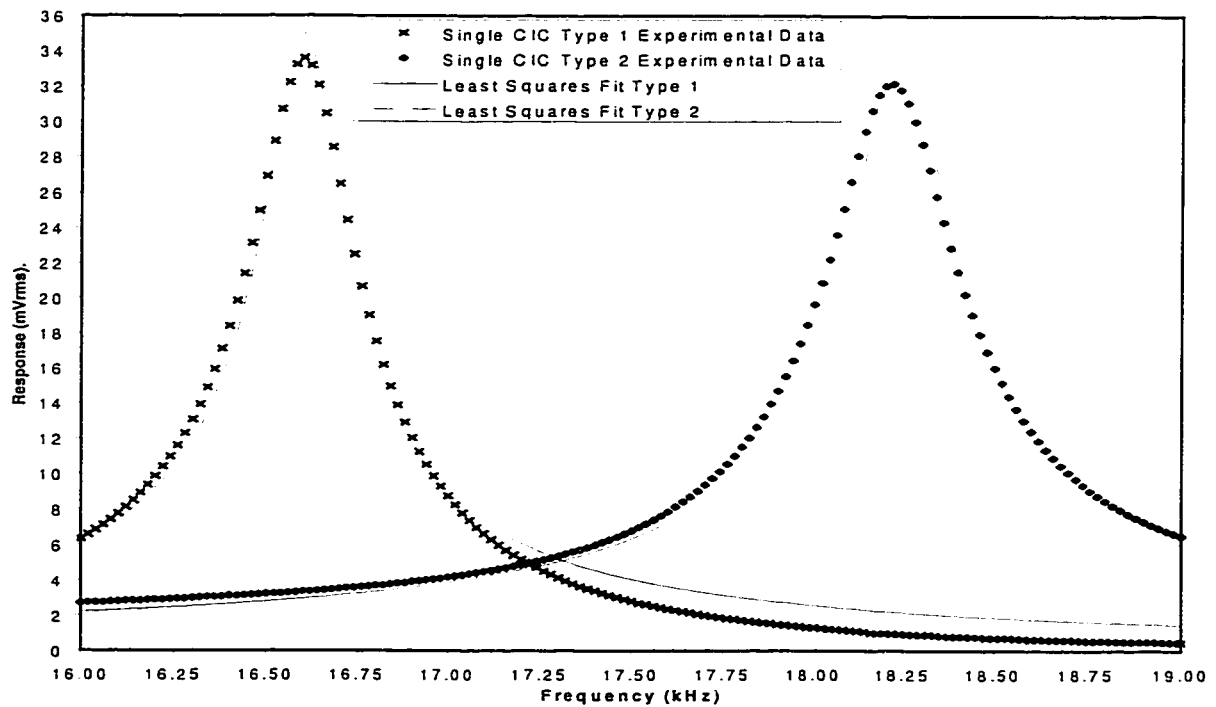


Figure 4.3 Least squares fitting of response of single CIC type 1 and 2 at constant actuating current versus frequency.

A statistical analysis of all devices tested was performed to find the mean resonant frequency (for the largest response peak), \bar{f}_o , the uncertainty in resonant frequency, $\delta\bar{f}_o$, and the mean difference in resonant frequency, Δf , between type 1 and type 2 devices. This analysis was done to determine the magnitude of the individual differences between devices for measuring the resonant frequency of the largest response. The results from this analysis are shown in Table 4.2, where n is the number of individual devices tested.

Table 4.2 Statistical analysis of largest response resonant frequency for CIC devices.

Device	\bar{f}_o (kHz)	$\delta\bar{f}_o$ (kHz)	n	Δf (kHz)
Single type 1	16.225	0.103	7	1.813
Single type 2	18.038	0.105	4	
Double type 1	12.668	0.040	8	0.727
Double type 2	13.395	0.214	4	
Triple type 1	8.510	0.006	3	

A detailed calculation of the mass for each device is presented in Table 4.3 below. Also shown is the mass difference (actual and percent) between the type 1 and type 2 devices. Each of the CMOS thin film materials used to fabricate the devices has a density of 2.7 ng/ μm^3 for polysilicon, 2.2 ng/ μm^3 for silicon dioxide, 2.7 ng/ μm^3 for aluminum, and 2.8 ng/ μm^3 for silicon nitride. The volumes of each layer are determined from the manufacturers specifications for layer thickness and the design area and do not account for any possible etching by XeF_2 . The material densities are those for bulk quantities at room temperature.

Table 4.3 Cantilever-in-cantilever thin film material mass and device mass.

Device	poly-silicon (ng)	silicon dioxide (ng)	aluminum (ng)	silicon nitride (ng)	Total mass (ng)	Δm (ng)	Δm (%)
Single type 1	0.854	385.0	125.8	77.1	569		
Single type 2	0.854	385.0	40.6	77.1	484	85.0	14.9%
Double type 1	0.854	485.4	125.8	97.2	709		
Double type 2	0.854	485.4	72.8	97.2	624	85.0	12.0%
Triple type 1	0.854	606.4	157.9	121.5	887		

Combining the values for Δf from Table 4.2 and the value for Δm from Table 4.3 yields a ratio of resonant frequency shift to change in mass. The ratio $\Delta f/\Delta m$ is 21.3 Hz/ng for a single CIC and 8.55 Hz/ng for a double CIC. Given a frequency resolution of 0.1 Hz for our apparatus, we can measure a mass change of 4 pg for a single CIC and 12 pg for a double CIC. These resolutions only apply to a mass uniformly distributed over the CIC surface and it is assumed device stiffness is not affected.

The natural frequency for a single degree-of-freedom system is denoted by

$$\omega_n = \sqrt{\frac{k}{m}} \quad (4.2.9)$$

where k is the stiffness, m is the system mass, and ω_n is the natural frequency assumed to be the same as the resonant frequency, ω_o , by the single degree-of-freedom curve fit approach as used in Section 4.2. Further analysis of the behaviour of the CIC devices can be achieved by the comparison of resonant frequencies and masses for type 1 and type 2 devices as shown in Table 4.2 and Table 4.3. This comparison takes the form of

$$\frac{\omega_{o,1}}{\omega_{o,2}} = \sqrt{\frac{m_2}{m_1}} \quad (4.2.10)$$

The L.H.S. of Equation (4.2.10) is 0.90 and 0.95 for single and double CIC's, respectively; while the R.H.S. of Equation (4.2.10) is 0.92 and 0.94 for single and double CIC's, respectively. There is good agreement between these values suggesting there is no difference in stiffness between type 1 and type 2 devices and that the device behaviour can be approximated by a single degree-of-freedom system at this resonant frequency.

4.3 PIEZORESISTANCE

In our CMOS micromachining process, polysilicon that is normally used for transistor gates and resistors is used as a piezoresistor. The placement of a segment of polysilicon within our cantilever-in-cantilever structure will permit the measurement of device deflections by measuring the resistance change of the polysilicon. Specifically, a small constant current is passed through the polysilicon and the voltage across it is measured. Any change in resistance due to mechanical stress will produce a change in voltage measured.

Piezoresistivity is a linear coupling between mechanical stress, X , and electrical resistivity, ρ [49]. The piezoresistance properties of semiconducting silicon and germanium were discovered by Smith in 1953 when he was verifying the form of their energy surfaces [50]. Piezoresistive effects in polysilicon were investigated later by Onuma and Kamimura in 1987 while conducting pressure measurements on a membrane [50]. The relationship between mechanical stress and electrical resistivity takes the form of

$$\frac{\delta\rho_{ij}}{\rho_o} = \Pi_{ijkl} X_{kl} \quad (4.3.1)$$

where ρ_o is the non-strained resistivity, $\delta\rho_{ij}$ is a symmetric second rank tensor denoting the change in resistivity, and X_{kl} is a symmetric second rank tensor denoting the mechanical stress. Combining two second rank tensors results in a fourth rank tensor which occurs in the form of Π_{ijkl} , the piezoresistivity tensor. The indices i and j take on values of 1,2, and 3, and correspond to the symmetric three-by-three matrix required to fully describe the piezoresistance effect in silicon. The same is true for the indices k and l . A detailed explanation of the origin of these indices can be found in [50]. Due to internal tensor symmetry and the structural properties of polycrystalline silicon the piezoresistivity tensor reduces from 81 independent components to 2; namely Π_{11} and Π_{12} . As such, Equation (4.3.1) can be expressed as

$$\frac{\delta R}{R} = \pi_L \Delta\sigma_L + \pi_T \Delta\sigma_T \quad (4.3.2)$$

where π_L is the longitudinal piezoresistive coefficient and π_T the transverse piezoresistive coefficient. The terms σ_L and σ_T are the stress components parallel and perpendicular to the current flow through the piezoresistor. Figure 4.4 is the conceptual diagram of a polysilicon piezoresistor embedded inside the arms of a cantilever.

Previous work has shown that the highest point of stress for a CIC device under static actuation occurs on the outer-most arms and at the clamped ends [18]. Hence, this is the best location for the placement of the piezoresistor for maximum sensitivity to structure deflection. Fabricating the polysilicon resistors parallel to the CIC arms, as shown previously in Figure 3.3, and actuating the structure at resonance, yields values for $\Delta\sigma_T$ of zero and $\Delta\sigma_L$ modulated by the deflection of the structure.

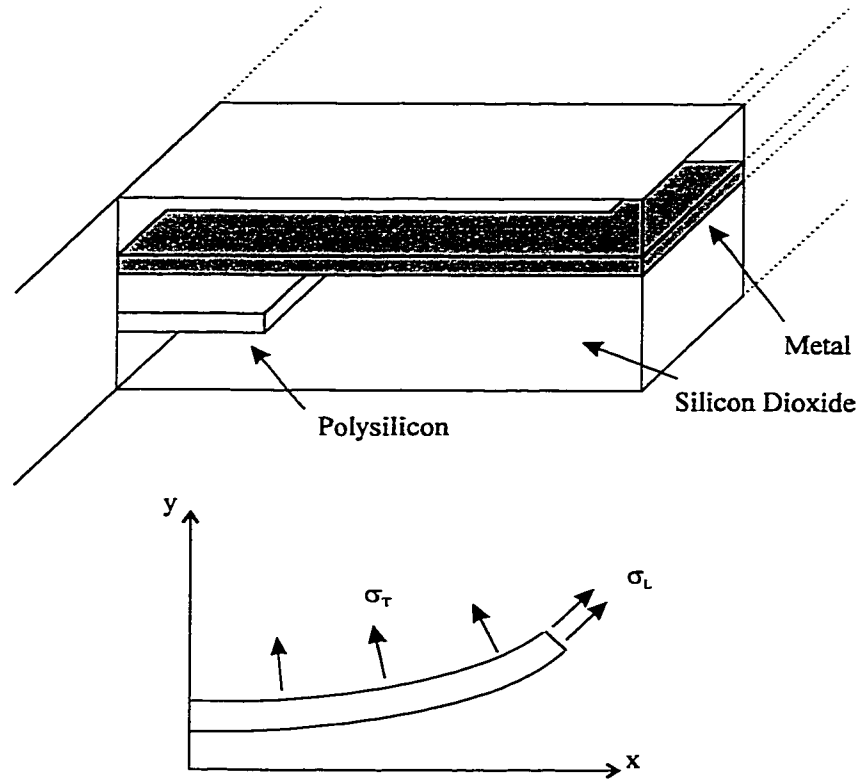


Figure 4.4 Polysilicon piezoresistor embedded inside CIC arm.

Assuming small deflections of the structure, to a first order approximation

$$\sigma_L = \sigma_{L0} + \Delta\sigma_L = \sigma_{L0} + cF \cos(\omega t) \quad (4.3.3)$$

where $F\cos(\omega t)$ is the vibration amplitude and c is a constant. Substituting Equation (4.3.3) into Equation (4.3.2) produces

$$\frac{\Delta R}{R} = \pi_L \Delta\sigma_L = \pi_L cF \cos(\omega t) \quad (4.3.4)$$

which means that a change in amplitude of oscillation is indicated directly by a change in resistance, R . Driving a constant current, I_o , through the polysilicon and measuring the change of voltage across it yields

$$\Delta U = I_o \Delta R = I_o R \frac{\Delta R}{R} = I_o R \pi_L cF \cos(\omega t) \quad (4.3.5)$$

Therefore, for small deformations of the polysilicon, the change in voltage measured may be used as an indication of the amount of cantilever deflection.

4.4 DAMPING RELATION

Knowing that our structures behave in a manner consistent with that of a damped, driven harmonic oscillator, we proceed with further modeling. The “damping relation” referred to here is a derivation of the dynamic response equation with regards to the viscous damping due to air pressure [52].

Substituting z from Equation (4.2.2) into Equation (4.2.1) results in an equation for the i -th mode of resonance:

$$\rho \ddot{c}_i + \rho_1 \dot{c}_i + \lambda_i c_i = \int_{device} G \phi_i dx dy \equiv f_i \sin \omega t \quad (4.4.1)$$

in which

$$f_i = \iint_{device} \frac{ILB \phi_i(x, y)}{A} dx dy \quad (4.4.2)$$

and is the actuating force on the current path of the device at the i -th mode of resonance in regions where the conductor is perpendicular to the magnetic field, B . Arranging Equation (4.4.1) to solve for $c_i(t)$ produces an equation of the form

$$\ddot{c}_i + \frac{\rho_1}{\rho} \dot{c}_i + \frac{\lambda_i}{\rho} c_i = \frac{f_i}{\rho} \sin \omega t \quad (4.4.3)$$

Expressing $c_i(t)$ as the sum of periodic functions

$$c_i = A_i \sin \omega_o t + B_i \cos \omega_o t \quad (4.4.4)$$

where ω_o is the angular resonant frequency of i -th mode, yields values for A_i and B_i in the form

$$A_i = \frac{\frac{f_i}{\rho} \left(\frac{\lambda_i}{\rho} - \omega_o^2 \right)}{\left[\left(\frac{\lambda_i}{\rho} - \omega_o^2 \right)^2 + \left(\frac{\rho_i}{\rho} \omega_o \right)^2 \right]} \quad (4.4.5)$$

$$B_i = \frac{-\frac{f_i}{\rho} \left(\frac{\rho_1}{\rho} \right) \omega_o}{\left(\frac{\lambda_i}{\rho} - \omega_o^2 \right)^2 + \left(\frac{\rho_1}{\rho} \omega_o \right)^2} \quad (4.4.6)$$

From the above derivations we can now solve for z in Equation (4.2.2) by substituting Equation (4.4.5) and Equation (4.4.6) into Equation (4.4.4) and applying the result to Equation (4.4.3). However, for a simpler solution, suppose we *choose* a value for ω_o so that we maximize the amplitude of a particular mode (referred to by the subscript '1'), where values for this resonant mode are

$$\omega_o = \sqrt{\left(\frac{\lambda_1}{\rho} \right) - \frac{1}{2} \left(\frac{\rho_1}{\rho} \right)^2} \quad (4.4.7)$$

and

$$z = \frac{|f_1|/\rho_1}{\sqrt{\left(\frac{\lambda_1}{\rho} \right) - \frac{1}{4} \left(\frac{\rho_1}{\rho} \right)^2}} \quad (4.4.8)$$

and where z is now the maximum device deflection at this one particular mode assuming all other modes make negligible contributions. This is a reasonable assumption given that in the first section of this chapter least squares curve fitting was obtained for each device using the “single-degree-of-freedom” curve fit approach. That is, we looked at the largest resonant peak and assumed that it was the result of one and only one mode.

We can now choose ω_o and z as for Equation (4.4.7) and Equation (4.4.8), and be confident that the other eigenvalues $\lambda_2, \lambda_3, \dots$ are *far* from λ_1 . Thus c_2, c_3, \dots will be approximately zero resulting in the simplified expression for Equation (4.2.2) of

$$z \approx c_1(t)\phi_1(x, y) \quad (4.4.9)$$

Thus, the deflection z at any point (x, y) at time t is now due to only one mode of oscillation, one eigenfunction of K_1 with one eigenvalue, λ_1 . This approach is different from the single-degree-of-freedom approach used in Section 4.2. The difference is that the single-degree-of-freedom method assumes the CIC structure is a point mass on a spring instead of the plate structure that it is.

Observe that multiplying Equation (4.4.7) and Equation (4.4.8) together and taking the inverse results in an equation of the form

$$\frac{1}{z \cdot \omega_o} = \frac{\rho_1}{|f_1|} \sqrt{\frac{\left(\frac{\lambda_1}{\rho}\right) - \frac{1}{4}\left(\frac{\rho_1}{\rho}\right)^2}{\left(\frac{\lambda_1}{\rho}\right) - \frac{1}{2}\left(\frac{\rho_1}{\rho}\right)^2}} \cong \frac{\rho_1}{|f_1|} \quad (4.4.10)$$

since the term under the square root $\cong 1$ because the square of ρ_1/ρ is small with respect to λ_1/ρ . The ratio of viscous damping to the area density is small since the viscous damping is the result of the air density compared to the area density of the CIC device. If the viscous damping were the result of a liquid or other equally dense medium then the ratio of viscous damping to the area density could not be neglected in Equation (4.4.10).

The damping of a CIC structure is due to two components: the internal damping and the external damping. This means that the damping term can be expressed in the form:

$$\rho_1 = \rho_i + \rho_e(p) \quad (4.4.11)$$

where ρ_i represents the device internal damping and $\rho_e(p)$ the external viscous damping, which is a function of gas pressure, p . Experimentally, we can plot the inverse of the maximum piezoresistive response, z_r , assuming it varies linearly with the deflection, z , divided by the resonant frequency versus pressure, p , and obtain what is called the “damping relation”:

$$\frac{1}{z_r \cdot \omega_o} = \frac{1}{|f_1|} [\rho_i + \rho_e(p)] \quad (4.4.12)$$

Figure 4.5 is an experimental plot of the “damping relation” as a function of pressure for each CIC device. The left-hand-side of Equation (4.4.12) is observed to be approximately linear at pressures above 200 Torr. We can thus say that $\rho_e(p) = \kappa p$ for some constant κ . Linear equations fitted by least squares to Figure 4.5 yield values for κ ranging from $280 \text{ (mV}_{pp}/\text{Hz})^{-1}$ for a single CIC to $430 \text{ (mV}_{pp}/\text{Hz})^{-1}$ for a triple CIC. These derivations are based on small deformations of the piezoresistive material where the linear theory of elasticity is valid.

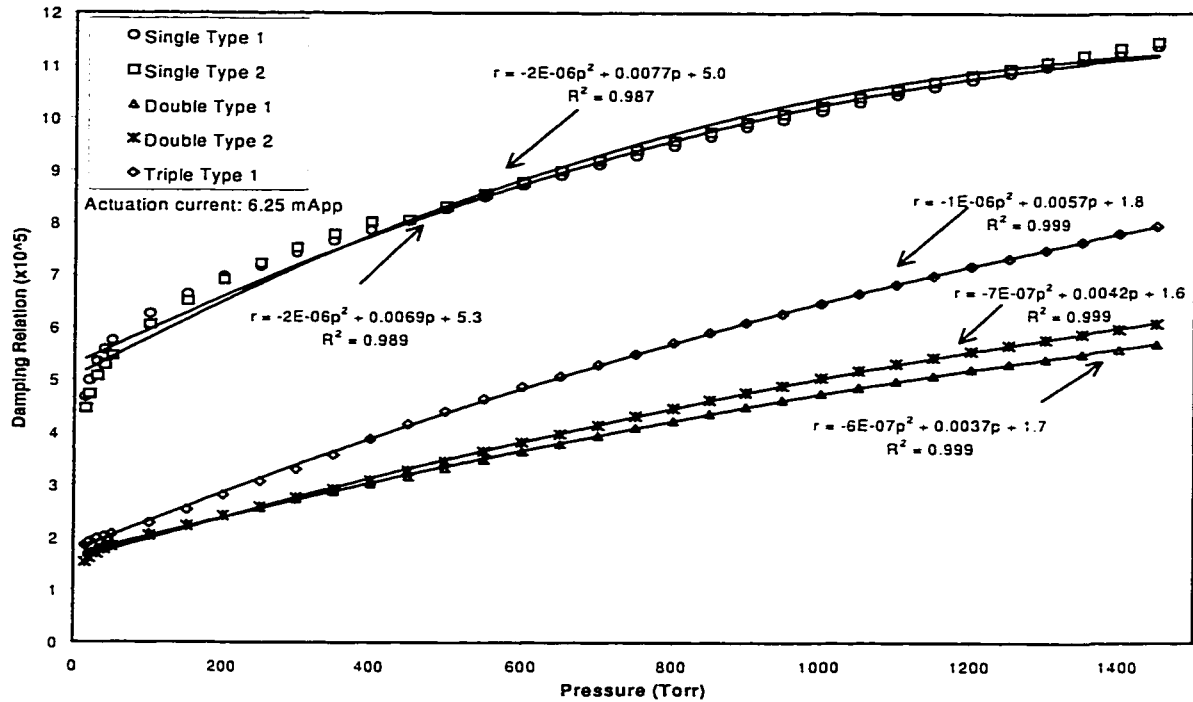


Figure 4.5 Damping relation versus pressure for CIC devices at constant actuating current.

4.5 NON-LINEARITY AND HYSTERESIS

From Figure 4.5 it can be seen that at pressures approaching 15 Torr the damping relation no longer varies linearly with pressure. Below 15 Torr, we have observed what we believe are non-linear effects producing a behaviour we call hysteresis. This behaviour occurs when there is a large deflection of the CIC. These large deflections occur at low pressure and also at high pressure with large actuating current.

Hysteresis leads to a plot where the path taken is dependent on the direction of travel. Figure 4.6 provides an example of a hysteresis loop in which travel from point 'a' to point 'b' takes place along the lower curve while the upper curve is followed for travel

from point 'b' to point 'a'. Hysteresis is commonly associated with ferromagnetic materials when the magnetic induction B is plotted versus the magnetic field intensity H .

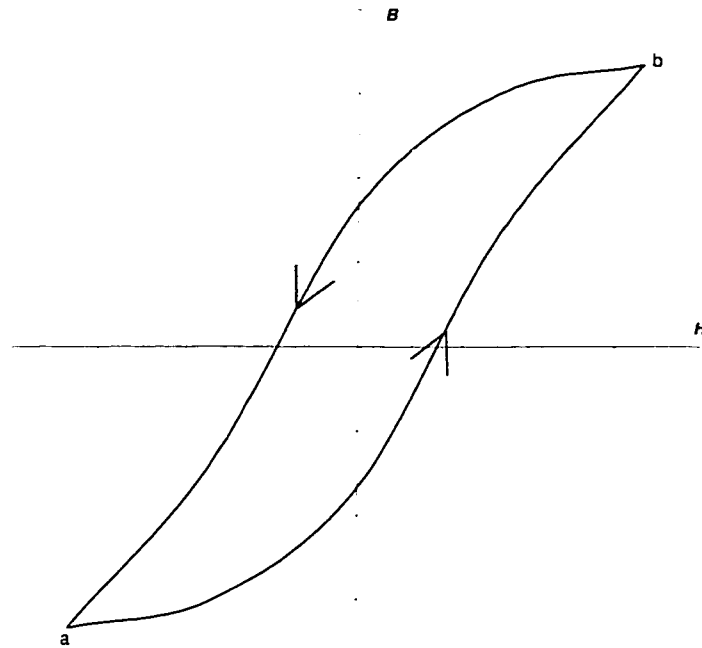


Figure 4.6 Example of hysteresis loop.

Specifically, for our CIC device, Figure 4.7 shows the cantilever deflection as a function of frequency for a triple CIC type 1 as the pressure is decreased from 300 Torr to 15 Torr. For each pressure a response was obtained over the frequency domain by sweeping first from 8400 Hz to 8700 Hz and then back down to 8400 Hz. The leftmost response curve for each pressure results from a decreasing frequency sweep. From the figure it is evident that as the pressure decreases the curves lose symmetry. The frequency at which maximum piezoresistive response occurs becomes dependent on whether the actuating frequency is increasing or decreasing. For pressures of 700 Torr and above, the frequency of maximum piezoresistive response is the same for both

increasing and decreasing frequencies. The small peaks present in Figure 4.7 on either side of the maximum piezoresistive response peak are believed to be the result of the digital multimeter changing the scale of measurement. This change of scale takes place at approximately $100 \text{ mV}_{\text{rms}}$, independent of frequency.

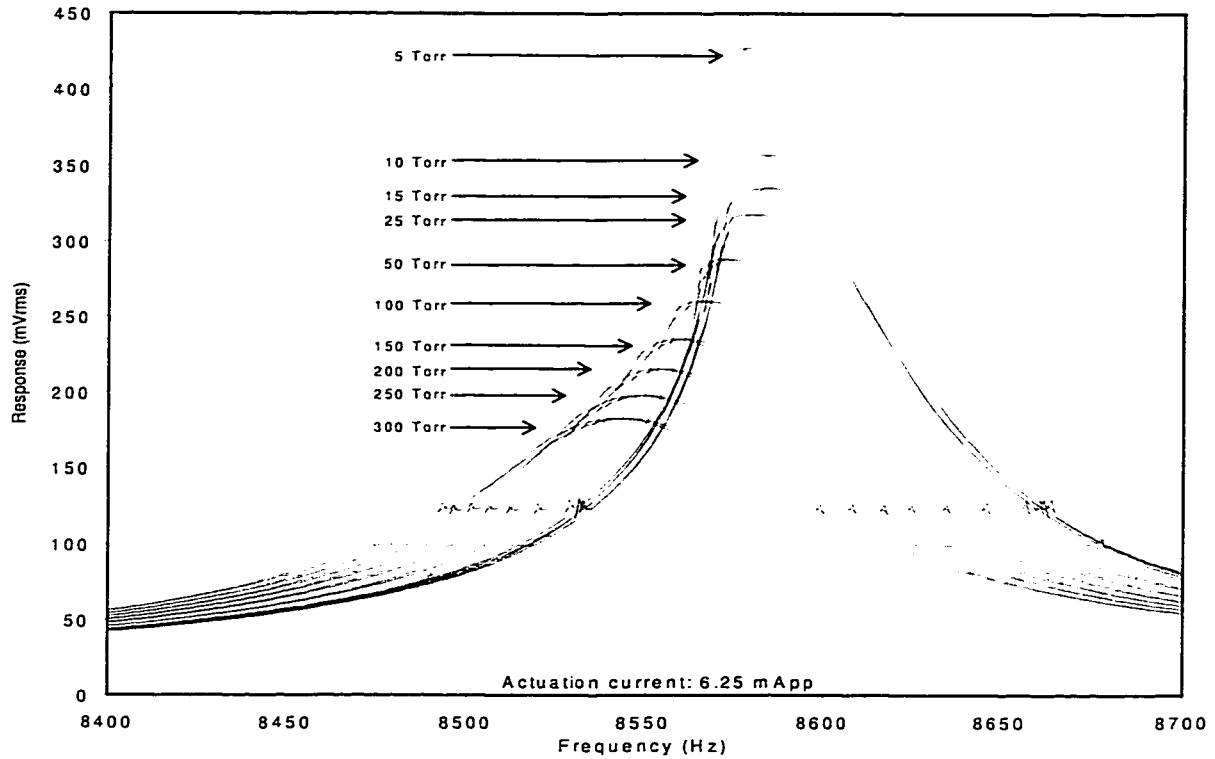


Figure 4.7 Frequency response for a triple CIC for various pressures at constant actuating current.

To help understand the nature of the response under these conditions a brief discussion of how these effects may be modeled is in order. What follows is by no means an exact account of the non-linear effects for these devices. Taking the linear equation of motion, Equation (4.2.1), for the CIC devices and adding a non-linear term results in an

equation similar in form to the Duffing equation for nonlinear spring motion, which is well understood:

$$\rho \frac{\partial^2 z}{\partial t^2} + \rho_1 \frac{\partial z}{\partial t} + K_1 z + K_3 z^3 = G(x, y, t) \quad (4.5.1)$$

where $K_1(z)$ is still the device stiffness pertaining to the linear equations of elasticity and $K_3(z)$ is the device stiffness arising from nonlinear cubic equations of elasticity [52,53]. A positive value for $K_3(z)$ is called the hard spring effect while a negative value is called the soft spring effect [55,56]. The sign of $K_3(z)$ also determines whether the response curve will bend to the right or left. From Figure 4.7 the curve appears to be bending towards the left implying a negative value for $K_3(z)$. The exact form of $K_3(z)$ for our devices has not yet been determined and is left for future work.

The hysteresis effect was investigated by varying the actuating current at 0.1, 1, and 10 Torr for a triple CIC type 1. The results are shown in Figures 4.8 to 4.11. As the frequency is increased there is an abrupt “jump” in piezoresistive response near the frequency where resonance is observed at higher pressures, followed by a continuous decrease in response as the frequency continues to increase. Reversing the direction of frequency sweep results in a continuous but larger increase in piezoresistive response until an abrupt “drop” in response is observed. The location of the decreasing “drop” frequency is less the increasing “jump” frequency.

As expected, decreasing the current or increasing the damping (pressure) reduced the device deflection and, hence, reduced the hysteresis effect. Measuring the difference between “jump” and “drop” frequencies may permit accurate pressure measurement well below 15 Torr. Table 4.4 shows the two frequencies at which maximum deflection

occurs for each frequency direction, f_0 , and their difference, Δf_0 , for each of the actuating currents at 0.1 Torr. The shape of the hysteresis curves in Figures 4.8 to 4.11 suggests that they are the result of soft spring effects. The “jump” frequency for this device is approximately independent of the actuating current and pressure, while the “drop” frequency is dependent on the device deflection (actuating current) and pressure.

Hysteresis effects have been observed in resonating micro-bridges [55] and resonating micro-diaphragms [56], when both types of devices were undergoing small deflections. This is the first time hysteresis has been reported for micro-cantilevers, and for large deflections.

Table 4.4 Hysteresis effect on maximum deflection frequency for triple

CIC type 1 at 0.1 Torr.

Actuation current (mA _{pp})	f_0 (increasing), (kHz)	f_0 (decreasing), (kHz)	Δf_0 (kHz)
3.0	8.586	8.378	208
1.76	8.594	8.430	164
1.0	8.593	8.532	61
0.5	8.597	8.577	20

To further investigate this behaviour a video was taken of the oscillating device using a CCD camera. The video was taken to determine if the device was truly oscillating with large deflections as suggested by the piezoresistive response voltage, or whether the piezoresistor was undergoing some other effect resulting in hysteresis. The CIC’s deflections were made observable by using a strobe light synchronized with the

actuating frequency. The video results showed that the device was producing large deflections at these pressures and actuating currents, thus confirming the piezoresistive response.

Data related to the double and single CIC devices regarding hysteresis was not obtained; however, all devices exhibited this behaviour given sufficient device deflection. As this is only an introduction to this phenomena much has been left for future investigation.

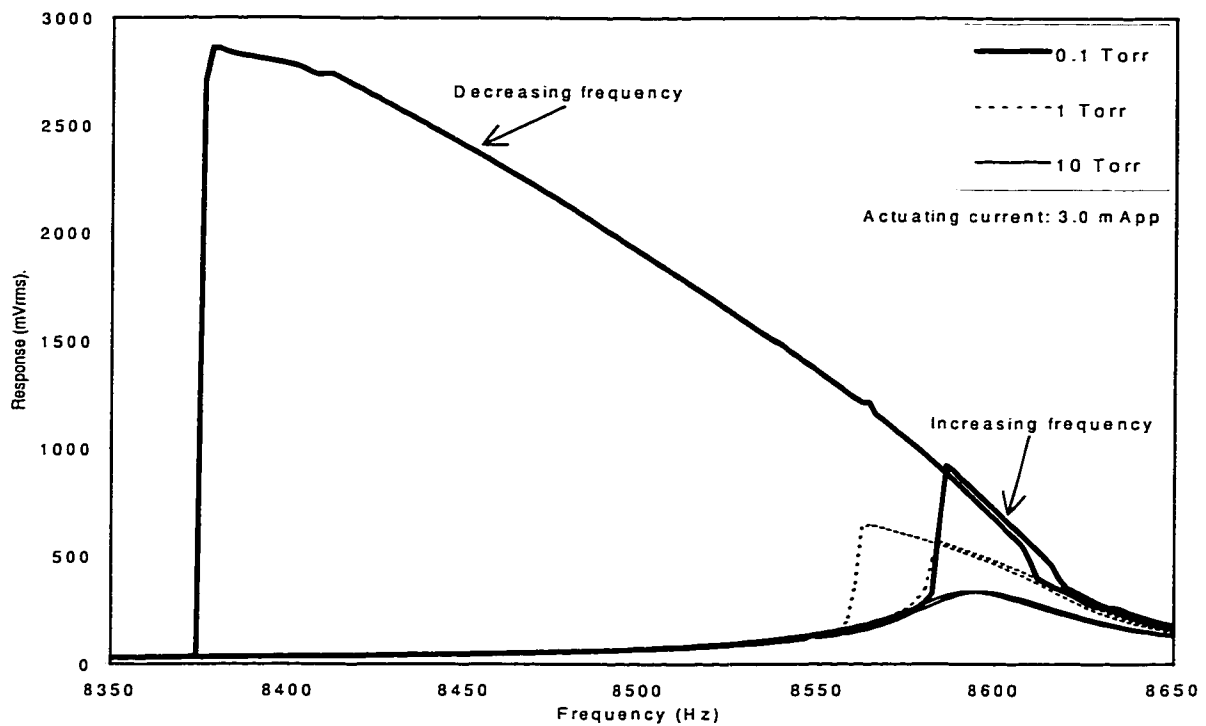


Figure 4.8 Frequency response for a triple CIC at 3.0 mA_{pp} constant actuating current.

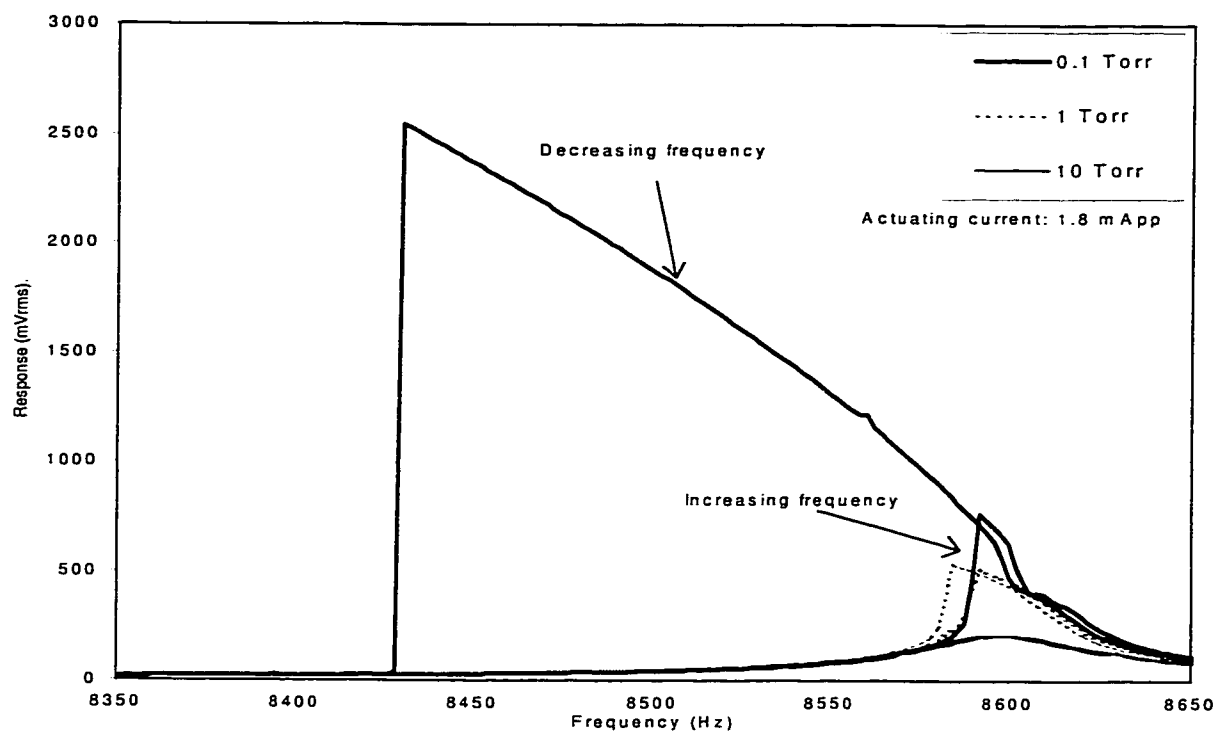


Figure 4.9 Frequency response for a triple CIC at 1.8 mA_{pp} constant actuating current.

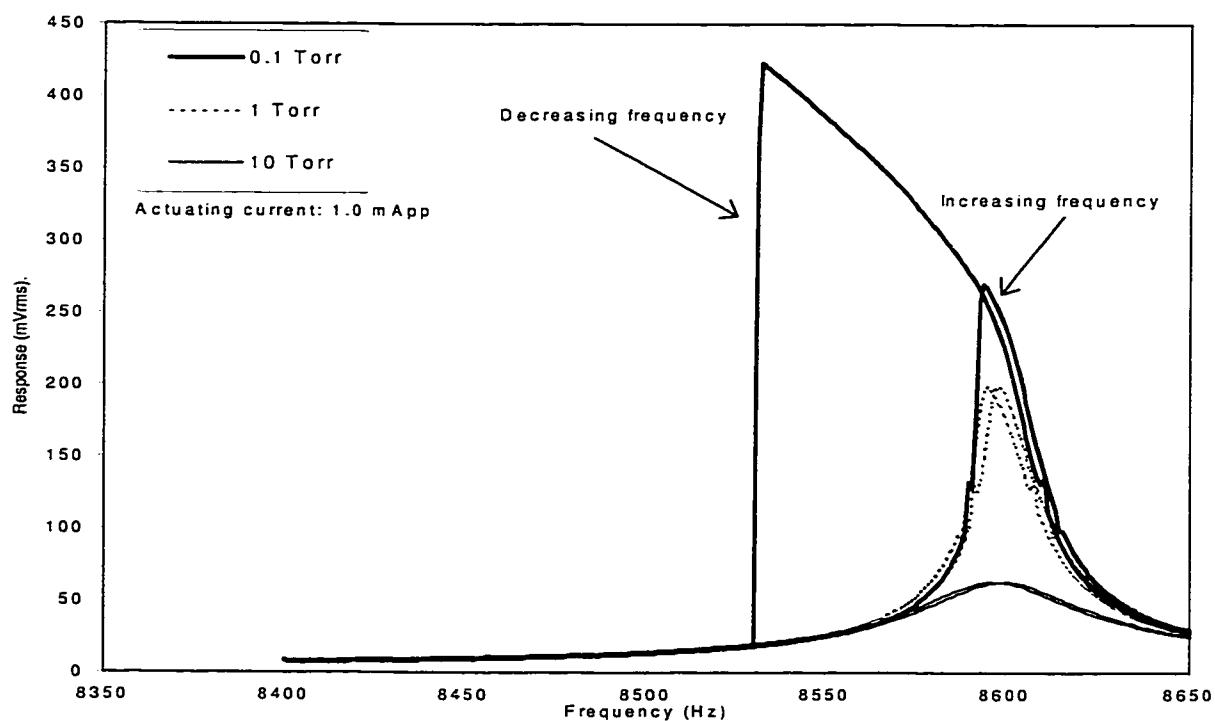


Figure 4.10 Frequency response for a triple CIC at 1.0 mA_{pp} constant actuating current.

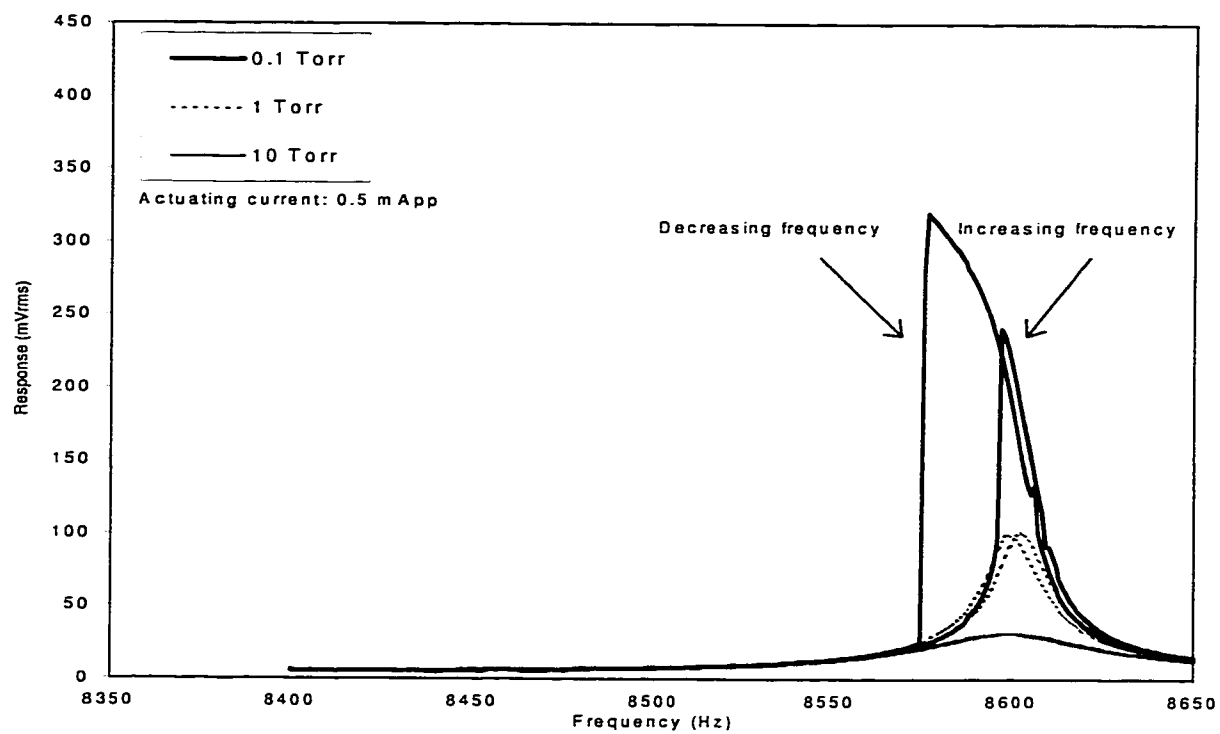


Figure 4.11 Frequency response for a triple CIC at 0.5 mA_{pp} constant actuating current.

Chapter 5

DISCUSSION

5.1 INTRODUCTION

As presented in Chapters 3 and 4, cantilever-in-cantilever microstructures may be used to measure gas pressure. The pressure may be deduced from the piezoresistive response, resonant frequency shift, quality factor change, or actuating current variation required to maintain constant response. In addition, Chapter 4 has introduced a further method of measuring gas pressure called the “damping relation”.

A discussion as to which method of gas pressure detection yields the highest sensitivity and greatest precision is relevant. Also important is a comparison between the responses of single, double, and triple CIC devices and their respective types 1 and 2. This is important to be able to determine which structure and parameter is best suited to performing the task of measuring gas pressure under given circumstances. For example, a triple CIC type 1 may have a higher piezoresistive response for a given actuating current for pressures ranging from 15 to 1450 Torr than a single CIC type 1. However, the single CIC type 1 may outperform the triple CIC type 1 over the same pressure regime if changes in resonant frequency are measured.

This chapter includes a discussion of the experimental data obtained and the results of the modeling analysis. The sensitivity of each device with respect to each of the parameters examined to detect gas pressure is discussed. Lastly, a brief discussion of possible device applications is presented.

5.2 PRESSURE SENSITIVITY

For this section the sensitivity of each device with respect to each of the five parameters that may be used to measure gas pressure is discussed. The parameters are presented in the same order in which they were first introduced in the preceding pages. It is my intent that there be minimal variations between devices of the same type. For this reason each of the devices tested resided on the same die and all were etched the same amount. All were investigated at the same temperature. All of the CIC devices tested were consistently reliable and yielded repeatable results. Analysis of the shape of the main resonance peak showed good correlation between experimentally measured results and analytically calculated ones, based on an idealized model. These results may be reviewed in Section 4.2, Table 4.1, and Figures 4.1 to 4.3 of Chapter 4.

Comparing similar devices that resided on separate die resulted in a variance of the mean of resonant frequency that ranged from 6 Hz for a triple type 1 to 214 Hz for a double type 2 device, as shown in Table 4.2. However, the number of devices measured is small, less than 30, and not too much statistical weight can be attached to these observations.

From Table 4.2 and Table 4.3 it can be seen that the different masses of type 1 and type 2 devices affect resonant frequency. There is a 14.9% mass difference between single CIC's type 1 and 2, which is responsible for a 1.813 kHz difference in resonant frequency. A resonant frequency shift of 0.727 kHz is due to a 12.0% mass difference between double CIC's type 1 and 2. This suggests that as the difference in mass divided by the overall device mass decreases the difference in resonant frequency also decreases.

5.2.1 Resonant Frequency

The first measurements were designed to measure the changes in resonant frequencies as the gas pressure was varied from 15 to 1450 Torr. Table 5.1 shows the incremental dependence of resonant frequency shifts upon small changes in pressure. These results were calculated from the data of Figures 3.11 – 3.13, where all curves were well fitted to a second order polynomial equation. The equation and derivative for each of the experimental plots is provided in Appendix B. Given the nature of the experimental setup and the computer algorithms used to find resonant frequency, a precision of ± 0.1 Hz in the measurement of frequency was achieved. One of the major limiting factors for this precision is the precision of the pressure gauges. The first column of Table 5.1 identifies each device and the second column shows the sensitivity of each device at 15 Torr. Sensitivity is calculated by taking the derivative of the best fit equation. The third column is identical to the second except it shows the sensitivity of each device at 1450 Torr. Taking the mean between sensitivities at 15 and 1450 Torr gives an indication of the average sensitivities of the various devices. Finally, the last column in Table 5.1 gives an indication of the mean resolution possible for each device over the pressure range 15 to 1450 Torr, assuming the equipment can reliably measure frequency to ± 0.1 Hz. The mean resolution is determined by inverting the mean sensitivity and multiplying by the precision (0.1 Hz). The results obtained show that the single type 2 device is the most sensitive device, when its performance is averaged over the entire pressure range considered.

Table 5.1 Comparison of device sensitivities for pressure measurement based on changes in resonant frequencies.

Device	df/dp at p=15 Torr (Hz/Torr)	df/dp at p=1450 Torr (Hz/Torr)	Mean Sensitivity (Hz/Torr)	Mean Resolution at ±0.1 Hz (Torr)
Single Type 1	-0.30	-0.16	-0.23	±4.3
Single Type 2	-0.40	-0.20	-0.30	±3.3
Double Type 1	-0.20	-0.06	-0.13	±7.7
Double Type 2	-0.20	-0.03	-0.12	±8.3
Triple Type 1	-0.10	-0.01	-0.06	±16.7

5.2.2 Quality Factor

The second method of gas pressure detection utilizes the change in quality factor, or Q , with pressure as shown in Figure 3.19. All curves were fitted to a power equation of the form

$$Q = kp^{-a} \quad (5.2.1)$$

with k and a being constants. These curve fits are, however, not shown in the figure but can be viewed in Appendix B. The determination of quality factor is described in Chapter 3, Section 3.4.2. Table 5.2, analogous to Table 5.1, presents results of sensitivity calculations for each device. The double type 2 and triple type 1 CIC devices exhibit the greatest decrease in quality factor with increases in pressure. The ability to measure pressure changes by noting changes in Q -value is an order of magnitude greater than is possible when measuring changes in resonant frequency. However, determining changes in Q is more complex than determining changes in resonant frequency. Note that the

order of performance of the various devices differs greatly from that depicted in the previous table, Table 5.1.

Table 5.2 Comparison of device sensitivities for pressure measurement based on changes in quality factor.

Device	dQ/dp at p=15 Torr (1/Torr)	dQ/dp at p=1450 Torr (1/Torr)	Mean Sensitivity (1/Torr)	Mean Resolution (Torr)
Single Type 1	-1.9	-0.007	-0.95	± 1.1
Single Type 2	-2.2	-0.007	-1.10	± 0.9
Double Type 1	-4.2	-0.011	-2.11	± 0.5
Double Type 2	-4.8	-0.011	-2.41	± 0.4
Triple Type 1	-4.7	-0.010	-2.36	± 0.4

5.2.3 Actuating Current

Maintaining the device at constant piezoresistive response ($60 \text{ mV}_{\text{rms}}$) and measuring the amount of actuation current required to maintain this response as a function of pressure is considered next. Table 5.3 presents the result of sensitivity calculations for each device. The single type 2 device requires the largest increase in actuating current to maintain constant deflection as pressure increases, making it the most sensitive device for this method of gas pressure detection. The least sensitivity is provided by the triple CIC type 1, which required the least increase in actuating current to maintain constant deflection as pressure increases. The experimental results for these devices are shown in Figure 3.20, where each experimentally obtained curve was fitted to a fourth order polynomial. Not all the fitting equations are shown to improve clarity and

to avoid congesting the graph. In determining the mean resolution for measuring pressure the ability to control actuating current to $\pm 10 \mu A_{pp}$ was considered reasonable.

Table 5.3 Comparison of device sensitivities for pressure measurement as actuating current is changed to keep device deflection constant.

Device	di/dp at p=15 Torr ($\mu A_{pp}/\text{Torr}$)	di/dp at p=1450 Torr ($\mu A_{pp}/\text{Torr}$)	Mean Sensitivity ($\mu A_{pp}/\text{Torr}$)	Mean Resolution at $\pm 10 \mu A_{pp}$ (Torr)
Single Type 1	39.1	95.5	67.3	± 0.2
Single Type 2	48.1	104.6	76.4	± 0.1
Double Type 1	8.7	4.6	6.7	± 1.5
Double Type 2	11.3	2.0	6.7	± 1.5
Triple Type 1	7.7	0.03	3.9	± 2.6

The order of device performance is similar to that depicted in Table 5.2. These results suggest that given a choice between measuring resonant frequency at constant current or actuating current at constant response, better mean resolution can be obtained using the latter method. However, for this latter method power consumption to actuate the device would not be constant.

5.2.4 Piezoresistive Response

For measuring pressure by noting piezoresistive response at resonance at constant actuating current, the most sensitive device is the double CIC type 2 followed closely by the triple CIC type 1, as shown in Table 5.4. The least sensitive devices are the double

CIC type 1 and the single CIC type 1. The lower sensitivity for double and single CIC devices is due to the reduced stiffness due to extra arms in the double and triple CIC's. The data from which the results of Table 5.4 are derived are shown in Figure 3.21 where all the curves are fitted to fourth degree polynomial equations. Again, to prevent clutter, not all polynomial equations are shown. All of the polynomial equations fitted to the experimental results in Figure 3.21 are presented in Appendix B. A resolution of $\pm 1 \text{ mV}_{pp}$ was used for calculating the mean resolution for piezoresistor response measurements. These measurements are perhaps the easiest to undertake – but the method does not yield very great sensitivities.

Table 5.4 Comparison of device sensitivities by measuring piezoresistive response at resonance as a function of pressure at constant actuating current.

Device	dV/dp at p=15 Torr (mV _{pp} /Torr)	dV/dp at p=1450 Torr (mV _{pp} /Torr)	Mean Sensitivity (mV _{pp} /Torr)	Mean Resolution at $\pm 1 \text{ mV}_{pp}$ (Torr)
Single Type 1	-0.41	0.88	0.24	± 4.2
Single Type 2	-0.37	-0.25	-0.31	± 3.2
Double Type 1	-1.54	1.15	-0.20	± 5.0
Double Type 2	-1.67	0.05	-0.81	± 1.2
Triple Type 1	-2.29	1.05	-0.62	± 1.6

5.2.5 Damping Relation

Finally, the sensitivity for each CIC device when employing the concept of “damping relation” is shown in Table 5.5. The experimental plot of the “damping

relation” for each CIC device is obtained by inverting the resonant frequency and dividing by the piezoresistive response. Shown in Figure 4.5 the “damping relation” is somewhat linear, with small negative curvature. Hence, the question arises as to the variation of ρ_1 with pressure. That is, does the viscous damping vary linearly with pressure? From our results it is concluded that the viscous damping is not completely linearly dependent on pressure. Using a measurement precision of ± 0.1 Hz and ± 1 mV_{pp} yields very similar mean resolutions for each of the CIC devices in Table 5.5. The most sensitive device is the single type 2 followed closely by the triple type 1 and single type 1 devices. The least sensitive CIC device is the double type 1.

Table 5.5 Comparison of device sensitivities by measuring the “damping relation” at resonance as a function of pressure at constant actuating current.

Device	dr/dp at p=15 Torr (1/Torr/ Hz/mV _{pp})	dr/dp at p=1450 Torr (1/Torr/ Hz/mV _{pp})	Mean Sensitivity (1/Torr/ Hz/mV _{pp})	Mean Resolution at ±1 mV _{pp} , ±0.1 Hz (Torr)
Single Type 1	241.8	38.9	140.4	±0.07
Single Type 2	270.1	67.2	168.7	±0.06
Double Type 1	130.2	69.3	99.8	±0.10
Double Type 2	147.7	76.7	112.2	±0.09
Triple Type 1	200.5	99.0	149.8	±0.07

5.3 CIC DEVICE APPLICATIONS

Possible applications for these devices as gas pressure measurement devices are in industrial atmospheres and meteorological environments. This section briefly describes

some of the design specifications that would be required for each of these particular working environments [8,57].

5.3.1 Industrial Atmospheres

Application of these devices in industrial atmospheres is at pressures of several atmospheres, and at high vacuums. For a high pressure system a resolution of a few tens of Torr is most likely sufficient and thus any CIC device and detection method is suitable which gives this resolution. However, for proper function at high pressures a sufficiently stiff device is required, suggesting the single CIC's over the double and triple CIC devices. In a vacuum system the requirements are quite the opposite. High sensitivity and a supple structure are mandatory. For this application the double and triple CIC's using the method of quality factor measurement, or the single CIC's using actuating current at constant deflection are best suited. Hysteresis effects must always be carefully monitored and compensated for by lowering the actuation force to reduce the deflections. Another possibility for measuring high vacuum pressures might be the measurement of the change in magnitude of hysteresis effects as a function of pressure.

Both the high pressure and vacuum applications would require temperature compensation and device calibration. High pressures would also require humidity compensation. Finally, resistance to corrosive atmospheres and external vibration would have to be considered.

5.3.2 Meteorological Environments

In a meteorological environment pressure measurements must be taken between 600 and 800 Torr, with a resolution better than 0.4 Torr. This corresponds to pressures of 80-107 kPa with a sensitivity of ± 0.05 kPa. Most commercial barometric pressure sensors measure to ± 0.1 kPa, with some measuring to ± 0.01 kPa. This limits the selection of devices and detection method to measurement of quality factor using double CIC type 2 or triple CIC type 1 devices, and the measurement of actuating current variations at constant device deflection using either of the single CIC device types. The method of measuring “damping relation” could also be used for any of the devices described here.

As in the industrial setting, this application would need device calibration and temperature compensation. An enclosed package would be needed to shield from wind effects and radiative heating from the sun. Humidity compensation, shock protection, and weathering prevention would need to be considered.

Chapter 6

CONCLUSION AND FUTURE WORK**6.1 GAS PRESSURE MICROSENSORS**

It has been shown in this thesis that resonating CMOS micromachined magnetically actuated cantilever-in-cantilever structures can be used to measure gas pressure over the range 15 Torr to 1450 Torr. Although these devices are not new, their use for gas pressure measurement is novel.

Gas pressure may be determined by measuring any one of five parameters: the change in maximum piezoresistive response at constant actuating current, the change in resonant frequency at which the maximum piezoresistive response occurs with constant actuating current, the change in actuation current required to maintain constant device deflection at the resonant frequency (at which the maximum piezoresistive response occurs), the change in quality factor, or Q , of the frequency response for maximum piezoresistive response with constant actuating current, and the change in “damping relation” as a function of pressure.

Five types of devices were designed, fabricated, and tested. These device types varied in stiffness, mass, and surface area, and a comparison of their abilities to measure pressure was carried out. All devices were stable and produced reproducible results.

There is good agreement between experiment and results obtained from analysis and modeling of the devices. The parameters that vary most linearly with gas pressure are the change in resonant frequency at which the maximum piezoresistive response occurs with constant actuating current, the change in actuation current required to

maintain constant device deflection at the resonant frequency (at which the maximum piezoresistive response occurs), and the change in “damping relation”. The parameter that varies most non-linearly with gas pressure is the change in quality factor, or Q , of the frequency response for maximum piezoresistive response with constant actuating current.

Finally, the observed hysteresis effect resulting from large device deflections is significant and requires further investigation. Perhaps the difference between resonant frequency peaks that is noted as frequency is increased, and then decreased, could be used to measure pressures well below 15 Torr.

6.2 FUTURE WORK

There are a number of areas that should be considered for further work. These include, but are not limited to:

- on-wafer signal conditioning
- on-wafer actuating magnetic field
- electrostatic actuation
- hysteresis

The on-wafer signal conditioning circuit would initially consist of a current mirror and amplifier circuits using MOSFET technology. Further circuitry could include a voltage-controlled oscillator to produce the actuating current, an analog-to-digital converter for measuring the piezoresistor voltage, and feedback circuitry. The latter would perform a similar function to that of the computer algorithms used to find the resonant frequency of maximum piezoresistive response and the actuating current required to maintain constant piezoresistive response.

Removing the bulky external magnet and replacing it with an on-wafer magnetic field generator is perhaps the greatest improvement that could be made [58]. It may also be useful to consider electrostatic actuation rather than magnetic actuation. For electrostatic actuation a voltage could be applied to the backside of the wafer to create the electric field required to deflect the cantilever.

Lastly, hysteresis effects are an obvious area for future work.

REFERENCES

- [1] D. Teegarden, G. Lorenz, and R. Neul, "How to Model and Simulate Microgyroscope Systems", *IEEE Spectrum*, vol. 35, no. 7, pp. 67, July 1998.
- [2] H. Fujita, "Microactuators and Micromachines", *Proc. IEEE*, vol. 86, no. 8, pp. 1721-1732, August 1998.
- [3] H. Baltes, "Future of IC Microtransducers", *Sensors and Actuators A*, vol. 56, pp. 179-192, 1996.
- [4] A.B. Frazier, "Guest Editorial Special Section on Micromachining", *IEEE Trans. Ind. Elect.*, vol. 45, no. 6, pp. 853, December 1998.
- [5] K.J. Gabriel, "Scanning the Technology", *Proc. IEEE*, vol. 86, no. 8, pp. 1534-1535, August 1998.
- [6] D.A. Koester, K.W. Markus, and M.D. Walters, "MEMS: Small Machines for the Microelectronics Age", *Computer*, vol. 29, pp. 93-94, January 1996.
- [7] A.V. Chavan and K.D. Wise, "A Batch-Processed Vacuum-Sealed Capacitive Pressure Sensor", *Ninth Int. Conf. Solid-State Sensors and Actuators* (Transducers '97), Chicago, pp. 1449-1452, June 1997.
- [8] R.H. Grace, "Automotive Applications of Microelectromechanical Systems", *Proc. Sensors Expo.*, Boston, pp. 67-74, May 16-18, 1995.
- [9] M. Esashi, S. Sugiyama, K. Ikeda, Y. Wang, and H. Miyashita, "Vacuum-Sealed Silicon Micromachined Pressure Sensors", *Proc. IEEE*, vol. 86, no. 8, pp. 1627-1639, August 1998.

- [10] H. Baltes, O. Paul, and O. Brand, "Micromachined Thermally Based CMOS Microsensors", *Proc. IEEE*, vol. 86, no. 8, pp. 1660-1678, August 1998.
- [11] D.S. Eddy and D.R. Sparks, "Application of MEMS Technology in Automotive Sensors and Actuators", *Proc. IEEE*, vol. 86, no. 8, pp. 1747-1755, August 1998.
- [12] H. Baltes, D. Lange, and A. Koll, "The Electronic Nose of Lilliput", *IEEE Spectrum*, vol. 35, no. 9, pp. 35-38, September 1998.
- [13] Y. Suzuki, T. Kudo, and K. Ikeda, "Accurate, Cost Effective Absolute Pressure Sensor", *Ninth Int. Conf. Solid-State Sensors and Actuators* (Transducers '97), Chicago, pp. 1493-1496, June 1997.
- [14] W.P. Eaton and J.H. Smith, "A CMOS-compatible, surface-micromachined pressure sensor for aqueous ultrasonic application", *SPIE Proc.*, vol. 2448, pp. 258-265, 1995.
- [15] H. Kim and K. Chun, "Integrated MEMS for Pressure Transponder", *Ninth Int. Conf. Solid-State Sensors and Actuators* (Transducers '97), Chicago, pp. 1011-1014, June 1997.
- [16] M.F. Miller, M.G. Allen, E. Arkilic, K.S. Breuer, and M.A. Schmidt, "Fabry-Perot Pressure Sensor Arrays for Imaging Surface Pressure Distributions", *Ninth Int. Conf. Solid-State Sensors and Actuators* (Transducers '97), Chicago, pp. 1469-1472, June 1997.

- [17] Y. Yoshii, A. Nakajo, H. Abe, K. Ninomiya, H. Miyashita, N. Sakurai, M. Kosuga, and S. Hao, "1 Chip Integrated Software Calibrated CMOS Pressure Sensor with MCU, A/D Convertor, D/A Convertor, Digital Communication Port, Signal Conditioning Circuit, and Temperature Sensor", *Ninth Int. Conf. Solid-State Sensors and Actuators* (Transducers '97), Chicago, pp. 1485-1488, June 1997.
- [18] B. Shen, "CMOS Actuators", *PhD Thesis*, University of Alberta, Canada, 1996.
- [19] Y. Ma, "Magnetically Actuated CMOS Micromachined CIC Devices", *MSc Thesis*, University of Alberta, Canada, 1997.
- [20] G.T. Kovacs, N.I. Maluf, and K.E. Petersen, "Bulk Micromachining of Silicon", *Proc. IEEE*, vol. 86, no. 8, pp. 1536-1551, August 1998.
- [21] J.M. Bustillo, R.T. Howe, and R.S. Muller, "Surface Micromachining for Microelectromechanical Systems", *Proc. IEEE*, vol. 86, no. 8, pp. 1552-1574, August 1998.
- [22] J.M. Rabaey, *Digital Integrated Circuits: A Design Perspective*, Prentice-Hall, New Jersey, pp. 2-4, 1996.
- [23] D.A. Johns and K. Martin, *Analog Integrated Circuit Design*, John Wiley & Sons, Toronto, 1997.
- [24] D.A. Johns and K. Martin, *Analog Integrated Circuit Design*, John Wiley & Sons, Toronto, pp. 82-94, 1997.
- [25] D.A. Johns and K. Martin, *Analog Integrated Circuit Design*, John Wiley & Sons, Toronto, pp. 125-127, 1997.

- [26] K. Petersen, "Silicon as a Mechanical Material", *Proc. IEEE*, vol. 70, no. 5, pp. 420-457, 1982.
- [27] A. Reismann, M. Berkenblit, S.A. Chan, F.B. Kaufman, and D.C. Green, "The controlled etching of silicon in catalyzed ethylenediamine-pyrocatechol-water solutions", *J. Electrochem. Soc.*, vol. 126, pp. 1406-1415, 1979.
- [28] M. Paranjape, "Vertical Hall Magnetic Field Microsensor Development and Implementation in CMOS Technology", *PhD Thesis*, University of Alberta, Canada, 1993.
- [29] J.R. Hook and H.E. Hall, *Solid State Physics*, 2nd ed., John Wiley and Sons, Inc., Canada, pp. 10, 1994.
- [30] Canadian Microelectronics Corporation, *An Introduction to Micromachining: Results of Projects Using Mitel's 1.5-micron CMOS Technology to Develop a Canadian MEMS Process*, Report IC95-08, Queen's University, Canada, 1995.
- [31] P.B. Chu, J.T. Chen, R. Yeh, G. Lin, J.C. Huang, B.A. Warneke, and K.S.J. Pister, "Controlled Pulse-Etching with Xenon Difluoride", *Ninth Int. Conf. Solid-State Sensors and Actuators* (Transducers '97), Chicago, pp. 665-668, June 1997.
- [32] R. Toda, K. Minami, and M. Esashi, "Thin Beam Bulk Micromachining Based on RIE and Xenon Difluoride Silicon Etching", *Ninth Int. Conf. Solid-State Sensors and Actuators* (Transducers '97), Chicago, pp. 671-674, June 1997.
- [33] I.W.T. Chan, K.B. Brown, R.P.W. Lawson, A.M. Robinson, Y. Ma, and D. Strembicke, "Gas Phase Pulse Etching of Silicon for MEMS with Xenon Difluoride", *IEEE Can. Conf. Electrical and Computer Engineering*, Edmonton, to be published May 1999.

- [34] E.J.J. Kruglick, S. Damle, and J. Pister, "Three-dimensional Structures for Micro-optical Mechanical Systems in Standard CMOS", *UCLA MEMS Trans.* vol. 19, October 1995.
- [35] F.I. Chang, R. Yeh, G. Lin, P.B. Chu, E. Hoffman, E.J.J. Kruglick, and K.S.J. Pister, "Gas-phase Silicon Micromachining with Xenon Difluoride", *Sym. on Microelectronic structures and MEM devices for optical proc. and multimedia appl.* (Proc. SPIE 2641), pp. 117-128, October 1995.
- [36] K.B. Brown, W. Allegretto, F. Vermeulen, and A.M. Robinson, "Cantilever-in-Cantilever Micro-Structures for Pressure and Magnetic Field Measurement", *Sym. Microelectronics R&D Can.* (TEXPO '98), Ottawa, Canada, June 25-26, 1998.
- [37] M. Spacek, K.B. Brown, Y. Ma, A.M. Robinson, R.P.W. Lawson, and W. Allegretto, "CMOS Cantilever Microstructures As Thin Film Deposition Monitors", *IEEE Can. Conf. Electrical and Computer Engineering*, Edmonton, to be published May 1999.
- [38] Y. Ma, A.M. Robinson, W. Allegretto, T. Zhou, and R.P.W. Lawson, "Static and dynamic characterization of magnetically actuated CMOS-micromachined cantilever-in-cantilever devices", *Can. J. Phys.*, vol. 76, pp. 747-758, 1998.
- [39] R. Rakoz, "Thermal Characterization of a Cantilever-in-Cantilever Microstructure", *Internal Paper: Micromachining Applications and Development Lab*, University of Alberta, Canada, 1998.
- [40] D.C. Giancoli, *Physics for Scientists and Engineers*, 2nd ed., Prentice-Hall, New Jersey, pp. 341-342, 1988.
- [41] S.T. Picraux and P.J. McWhorter, "The Broad Sweep of Integrated Microsystems", *IEEE Spectrum*, vol. 35, no. 12, pp. 24-33, December 1998.

- [42] B. Shen, W. Allegretto, Y. Ma, B. Yu, M. Hu, and A.M. Robinson, "Cantilever Micromachined Structures in CMOS Technology with Magnetic Actuation", *Sensors and Materials*, vol. 9, no. 6, pp. 347-362, 1997.
- [43] B. Shen, W. Allegretto, M. Hu, and A.M. Robinson, "CMOS Micromachined Cantilever-in-Cantilever Devices with Magnetic Actuation", *IEEE Electron Dev. Lett.*, vol. 17, no. 7, pp. 372-374, July 1996.
- [44] B. Shen, A.M. Robinson, W. Allegretto, Y. Ma, B. Yu, and M. Hu, "Magnetically Actuated CMOS Micromachined Cantilever-in-Cantilever Devices", *IEEE Can. Conf. Elec. and Comp. Eng.*, pp. 84-87, Calgary, May 1996.
- [45] B. Shen, A.M. Robinson, W. Allegretto, Y. Ma, B. Yu, and M. Hu, "A Magnetically Actuated Cantilever-in-Cantilever Micromachined Device", *Sym. Microelectronics R&D Can. (TEXPO '96)*, Ottawa, Canada, June 17-19, 1996.
- [46] S. Timoshenko and S. Woinowsky-Krieger, *Theory of Plates and Shells*, McGraw-Hill, New York, 1959.
- [47] D.J. Inman, *Engineering Vibration*, Prentice-Hall, New Jersey, pp. 378-381, 1996.
- [48] M. Garbuny, *Optical Physics*, Academic Press, Inc., New York, pp. 270, 1965.
- [49] R.C. Dorf, ed., *The Electrical Engineering Handbook*, CRC Press, Florida, pp. 1099-1105, 1993.
- [50] C.S. Smith, "Piezoresistance Effect in Germanium and Silicon", *Phys. Rev.*, vol. 94, no. 1, pp. 42-49, April 1954.
- [51] Y. Onuma and K. Kamimura, "Piezoresistive Elements of Polycrystalline Semiconductor Thin Films", *Sensors and Actuators*, vol. 13, pp. 71-77, 1988.

- [52] K.B. Brown, W. Allegretto, F.E. Vermeulen, R.P.W. Lawson, and A.M. Robinson, "Cantilever-in-Cantilever Micromachined Pressure Sensors Fabricated in CMOS Technology", *IEEE Can. Conf. Electrical and Computer Engineering*, Edmonton, to be published May 1999.
- [53] S.G. Adams, F.M. Bertsch, K.A. Shaw, and N.C. MacDonald, "Independent Tuning of Linear and Nonlinear Stiffness Coefficients", *J. Microelectromechanical Systems*, vol. 7, no. 2, pp. 172-180, June 1998.
- [54] A. Dimarogonas, *Vibration for Engineers*, 2nd ed., Prentice-Hall, New Jersey, pp. 131-139, 152-159, 1996.
- [55] C. Gui, R. Legtenberg, H.A.C. Tilmans, J.H.J. Fluitman, and M. Elmenspoek, "Nonlinearity and Hysteresis of Resonant Strain Gauges", *J. Microelectromechanical Systems*, vol. 7, no. 1, pp. 122-127, March 1998.
- [56] H.A.C. Tilmans and R. Legtenberg, "Electrostatically driven vacuum-encapsulated polysilicon resonators. Part II. Theory and performance", *Sensors and Actuators A*, vol. 45, pp. 67-84, 1994.
- [57] J. Fraden, *Handbook of Modern Sensors: Physics, Designs, and Applications*, 2nd ed., Springer-Verlag, New York, pp. 335-354, 1996.
- [58] C.H. Ahn and M.G. Allen, "Micromachined Planar Inductors on Silicon Wafers for MEMS Applications", *IEEE Trans. Ind. Elect.*, vol. 45, no. 6, pp. 866-876, December 1998.

Appendix A

EXAMPLE OF DATA ACQUISITION PROGRAM CODE

This appendix is an example of one of four programs developed for and used by the automated data acquisition system. The acquisition system was used to collect all experimental data. The software runs in a DOS environment and controls the digital multimeter and arbitrary waveform generator via the communication ports. The data is written to hard disk in a comma-delimited form allowing for easy import into any spreadsheet application for plotting.

This particular program lets the user specify a frequency range and step size to sweep while measuring the piezoresistive response. In addition, multiple sweeps in different directions and at different frequency step sizes within each sweep can be specified.

```

Declare SUB setup()
Declare SUB coarse (s,r)
Declare SUB openFile (s)
Declare SUB getData ()
Declare SUB closeFile ()
Declare SUB finish ()

Common Shared filename$, fullFileName$, f, freqstep, voltageResponse
Common Shared numResonances, numDesiredSets, numActualSets, deffilename$
Common Shared defstartfreq, defstopfreq, deffreqstep, defSweepBothWays$
Common Shared defNumDesiredSets, defNumRanges, maxSets, maxRanges
Common Shared maxResonances, description$, bignessFactor, numSamples
Common Shared trigDelay, maxVoltageFreq, maxVoltageResponse, defkeypress$
Common Shared keypress$ maxSets=20, maxRanges=20, maxResonances=5000

Dim Shared mvpp(maxSets), numRanges(maxSets), startfreq(maxSets, maxRanges)
Dim Shared stopfreq(maxSets, maxRanges), freqstep(maxSets, maxRanges)
Dim Shared resonance(maxResonances, 2), sweepBothWays$(maxSets)

```

```

deffilename$="sweep": defstartfreq=1000: defstopfreq=25000: deffreqstep=5
defSweepBothWays$="n": defNumDesiredSets=1: defma=10: deflr=285
defNumRanges=1: defkeypress$="n"

bignessFactor=1.004
cls:locate 1,28: color 12: "?"="--";: color 10: "?" Frequency Sweeper ": color 12: "?"="--"
color 15: ?
CALL setup
numResonances=0
for s=1 to numDesiredSets
    f=startfreq(s,1): ?#1,"FREQ";f: ?#1,"VOLT?": input#1, vpp mvpp(s)=vpp*1000
    sleep1
    CALL openFile(s)
    ?:"Set";rtrim$(str$(s));, saving to file ";fullFileName$
    for r=1 to numRanges(s)
        if startfreq(s,r)>stopfreq(s,r) then freqstep(s,r)=-freqstep(s,r)
        end if
    next r
    if sweepBothWays$(s)="y" then numOneWaySweeps=2
    elseif sweepBothWays$(s)="n" then numOneWaySweeps=1
    end if
    for r=1 to numRanges(s) ?:"Range";r: ?:"Frequency (Hz)","Response
        (mVrms)": ?:" numActualOneWaySweeps=0
        do while numActualOneWaySweeps<numOneWaySweeps
            CALL coarse(s,r) numActualOneWaySweeps =
            numActualOneWaySweeps+1
            if sweepBothWays$(s)="y" then temp=startfreq(s,r)
                startfreq(s,r)=stopfreq(s,r): stopfreq(s,r)=temp
                freqstep(s,r)=-freqstep(s,r)
            endif
        loop
    next r
    CALL closeFile
    if keypress$="y" and s<>numDesiredSets then ?#1, "SYSTEM:BEEP": ?
        ?" Press any key to continue with next set...": sleep
    end if
next s
?: ?"Driving frequency yielding maximum response (Hz):", maxVoltageFreq
?"Maximum response (mVpp):",,, maxVoltageResponse*1000
CALL finish

SUB setup

Dim defstartfreqArray(maxRanges)
Dim defstopfreqArray(maxRanges)
Dim deffreqstepArray(maxRanges)
for r=1 to maxRanges: defstartfreqArray(r)=defstartfreq: defstopfreqArray(r)=defstopfreq

```

```

    deffreqstepArray(r)=deffreqstep
next r
?"Base name of data file (default is '"+deffilename$+"')";: input filename$
if filename$="" then filename$=deffilename$
?"Description to add to file (press Enter to skip)";: input": " , description$
?"Number of sets (default is";defNumDesiredSets; ")";: input numDesiredSets
if numDesiredSets=0 then numDesiredSets=defNumDesiredSets
if numDesiredSets<>1 then ?"Wait for keypress between sets (default is
    '"+defkeypress$+"')";: input keypress$
end if
if keypress$<>"y" then keypress$=defkeypress$
for s=1 to numDesiredSets: ?:"Set"; rtrim$(str$(s)); " , "
    ? , "Sweep both ways (y/n) (default is " ; defSweepBothWays$ ; ")";
    input sweepBothWays$(s)
    if sweepBothWays$(s)="" then sweepBothWays$(s)=defSweepBothWays$
    else defSweepBothWays$=sweepBothWays$(s)
    end if

150    ? , "Number of ranges (default is"; defNumRanges; ")";: input numRanges(s)
    if numRanges(s)=0 then numRanges(s)=defNumRanges
    else defNumRanges=numRanges(s): end if
    for r=1 to numRanges(s): ?:"Range";r;": "

100    ? , "Starting frequency (Hz) (default is";defstartfreqArray(r);")";: input
    startfreq(s,r)
    if startfreq(s,r)=0 then startfreq(s,r)=defstartfreqArray(r)
    elseif startfreq(s,r)<.0001 or startfreq(s,r)>1.5E+07 then ? , "Range must be from
        0.0001 to 15,000,000 Hz": goto 100
    else defstartfreqArray(r)=startfreq(s,r)
    end if

120    ? , "Stopping frequency (Hz) (default is";defstopfreqArray(r);")";: input
    stopfreq(s,r)
    if stopfreq(s,r)=0 then stopfreq(s,r)=defstopfreqArray(r)
    elseif stopfreq(s,r)<.0001 or stopfreq(s,r)>1.5E+07 then ? , "Range must be from
        0.0001 to 15,000,000 Hz": goto 120
    else defstopfreqArray(r)=stopfreq(s,r)
    end if

140    ? , "Frequency step size (Hz) (default is";deffreqstepArray(r);")";: input
    freqstep(s,r): freqstep(s,r)=abs(freqstep(s,r))
    if freqstep(s,r)=0 then freqstep(s,r)=deffreqstepArray(r)
    elseif freqstep(s,r)<.0001 or freqstep(s,r)>abs(stopfreq(s,r)-startfreq(s,r)) then
        ? , "Step size must be larger than 0.0001 and smaller
        than";abs(stopfreq(s,r)-startfreq(s,r)): goto 140
    else deffreqstepArray(r)=freqstep(s,r)

```

```

        end if
    next r
next s

```

```

?:?"Set the Function Generator to a desired amplitude, and press any key to begin..."
sleep: com(1) on: com(2) on
open "com1:9600,n,8,2,rs,lf" for random as #1
open "com2:9600,n,8,2,rs,lf" for random as #2
?:?"Please wait...":?:?#1, "SYSTEM:REMOTE":?#2, "SYSTEM:REMOTE"
?#2, "*RST":?#2, "CONF:VOLT:AC":?#2, "TRIGGER:SOURCE BUS": sleep 1

```

```
END sub
```

```
SUB coarse(s,r)
```

```

if freqstep(s,r)<=1 then trigDelay=.1: numSamples=1
elseif freqstep(s,r)>1 and freqstep(s,r)<=2 then trigDelay=.2: numSamples=2
elseif freqstep(s,r)>2 and freqstep(s,r)<=10 then trigDelay=.3: numSamples=2
elseif freqstep(s,r)>10 and freqstep(s,r)<=50 then trigDelay=.4: numSamples=4
elseif freqstep(s,r)>50 then trigDelay=.5: numSamples=5
end if
for f=startfreq(s,r) to stopfreq(s,r) step freqstep(s,r)
    keystore$=inkey$
    if keystore$="x" then EXIT sub
    CALL getData
next f

```

```
END sub
```

```
SUB openFile(s)
```

```

If s<10 then fullFileName$=filename$+".s0"+ltrim$(str$(s))
Else fullFileName$=filename$+".s"+ltrim$(str$(s))
end if
Open fullFileName$ for output as #3: ?#3, "-----"
?#3, "File name: ";fullFileName$: ?#3, "Description: ";description$
?#3, ?#3, "Date: "; date$: ?#3, "Start time: "; time$
?#3, "Function Gen. amplitude: ";mvpp(s):"mVpp": ?#3: ?#3, "Ranges:"
for r=1 to numRanges(s): ?#3,,"Starting frequency: "; startfreq(s,r) ?#3,,"Stopping
    frequency: "; stopfreq(s,r): ?#3,,"Frequency step size: ";freqstep(s,r)
    ?#3,
next r
?#3,,"-----": ?#3, ?#3, "Frequency (Hz)";",",";"Response (mVrms)"

```

```
END sub
```

SUB getData

```
?#1, "FREQ";f: ?#2, "TRIG:DELAY"; trigDelay: ?#2, "INIT": ?#2, "*TRG"
?#2, "FETCH?": input#2, response: sum=sum+response
if numSamples>=2 then ?#2, "TRIG:DELAY 0"
    for i=2 to NumSamples: ?#2, "INIT": ?#2, "*TRG": ?#2, "FETCH?"
        input#2, response: sum=sum+response
    next i
    voltageResponse=sum/numSamples: ?#2, "TRIG:DELAY"; trigDelay
else voltageResponse=response
end if
if voltageResponse>maxVoltageResponse then maxVoltageFreq=f
    maxVoltageResponse=voltageResponse
end if
?, ltrim$(str$(f)),ltrim$(str$(voltageResponse*1000))
?#3, ltrim$(str$(f));",";ltrim$(str$(voltageResponse*1000))
```

END sub

SUB closeFile

```
?#3,: ?#3, "End time: "; TIME$: ?#3,"-----": close#3
```

END sub

SUB finish

```
?#1, "SYSTEM:BEEP": ?#2, "SYSTEM:BEEP": sleep .7: ?#1, "SYSTEM:BEEP"
?#2, "SYSTEM:BEEP": ?#1, "SYSTEM:LOCAL": ?#2, "SYSTEM:LOCAL"
close: com(1) off: com(2) off
```

END sub

Appendix B

EQUATIONS DERIVED FROM LEAST SQUARES CURVE FITTING OF EXPERIMENTAL DATA

RESONANT FREQUENCY: (Figures 3.11 – 3.13, f in kHz, p in Torr)

Single CIC type 1: $f = 5 \times 10^{-8} p^2 - 0.0003p + 16.8$

Single CIC type 2: $f = 7 \times 10^{-8} p^2 - 0.0004p + 18.5$

Double CIC type 1: $f = 5 \times 10^{-8} p^2 - 0.0002p + 12.9$

Double CIC type 2: $f = 6 \times 10^{-8} p^2 - 0.0002p + 13.9$

Triple CIC type 1: $f = 3 \times 10^{-8} p^2 - 0.0001p + 8.6$

QUALITY FACTOR: (Figure 3.19, Q is unitless, p in Torr)

Single CIC type 1: $Q = 233.7p^{-0.218}$

Single CIC type 2: $Q = 255.7p^{-0.258}$

Double CIC type 1: $Q = 478.8p^{-0.294}$

Double CIC type 2: $Q = 537.8p^{-0.331}$

Triple CIC type 1: $Q = 523.5p^{-0.340}$

ACTUATING CURRENT: (Figure 3.20, i in mA_{pp}, p in Torr)

Single CIC type 1: $i = -4 \times 10^{-12} p^4 + 2 \times 10^{-8} p^3 - 2 \times 10^{-5} p^2 + 1.4 \times 10^{-2} p + 4.6$

Single CIC type 2: $i = -4 \times 10^{-12} p^4 + 2 \times 10^{-8} p^3 - 2 \times 10^{-5} p^2 + 1.8 \times 10^{-2} p + 4.7$

Double CIC type 1: $i = -4 \times 10^{-13} p^4 + 1 \times 10^{-9} p^3 - 1 \times 10^{-6} p^2 + 3.1 \times 10^{-3} p + 1.3$

Double CIC type 2: $i = -6 \times 10^{-13} p^4 + 2 \times 10^{-9} p^3 - 3 \times 10^{-6} p^2 + 4.1 \times 10^{-3} p + 1.3$

Triple CIC type 1: $i = 6 \times 10^{-13} p^4 - 2 \times 10^{-9} p^3 + 9 \times 10^{-7} p^2 + 2.7 \times 10^{-3} p + 0.89$

PIEZORESISTIVE RESPONSE: (Figure 3.21, V in mV_{rms} , p in Torr)

$$\text{Single CIC type 1: } V = 7 \times 10^{-11} p^4 - 2 \times 10^{-7} p^3 + 3 \times 10^{-4} p^2 - 0.152p + 69.2$$

$$\text{Single CIC type 2: } V = 6 \times 10^{-11} p^4 - 2 \times 10^{-7} p^3 + 2 \times 10^{-4} p^2 - 0.138p + 71.7$$

$$\text{Double CIC type 1: } V = 2 \times 10^{-10} p^4 - 6 \times 10^{-7} p^3 + 8 \times 10^{-4} p^2 - 0.567p + 279$$

$$\text{Double CIC type 2: } V = 2 \times 10^{-10} p^4 - 7 \times 10^{-7} p^3 + 9 \times 10^{-4} p^2 - 0.615p + 272$$

$$\text{Triple CIC type 1: } V = 2 \times 10^{-10} p^4 - 7 \times 10^{-7} p^3 + 1.1 \times 10^{-3} p^2 - 0.842p + 379$$

DAMPING RELATION: (Figure 4.5, r in $1/mV_{pp}/Hz \times 10^5$, p in Torr)

$$\text{Single CIC type 1: } r = -2 \times 10^{-6} p^2 + 6.9 \times 10^{-3} p + 5.3$$

$$\text{Single CIC type 2: } r = -2 \times 10^{-6} p^2 + 7.7 \times 10^{-3} p + 5.0$$

$$\text{Double CIC type 1: } r = -6 \times 10^{-7} p^2 + 3.7 \times 10^{-3} p + 1.7$$

$$\text{Double CIC type 2: } r = -7 \times 10^{-7} p^2 + 4.2 \times 10^{-3} p + 1.6$$

$$\text{Triple CIC type 1: } r = -1 \times 10^{-6} p^2 + 5.7 \times 10^{-3} p + 1.8$$